Alpine rock glacier activity over Holocene to modern timescales (western French Alps)

Benjamin Lehmann[1,2*], Robert S. Anderson[2], Xavier Bodin[1], Diego Cusicanqui[1,3], Pierre G. Valla[4], and Julien Carcaillet[4]

[1]Université Savoie Mont Blanc, CNRS, EDYTEM, 73000, Chambéry, France
[2]INSTAAR and Department of Geological Sciences, University of Colorado Boulder, Boulder, CO 80309, USA
[3]Université Grenoble Alpes, CNRS, IRD, IGE, Grenoble, France
[4]Université Grenoble Alpes, Univ. Savoie Mont Blanc, CNRS, IRD, IFSTTAR, ISTerre, 38000, Grenoble, France

Correspondence to: Benjamin Lehmann (lehmann.benj@gmail.com)

Abstract. ~~Rock~~Active rock glaciers are some of the most frequent cryospheric landforms in mid-latitude high-elevation mountain ranges. Their activity strongly influences the hydrology and geomorphology of alpine environments over short (years to decades) and long (centuries to millennia) timescales. Being conspicuous expressions of mountain permafrost and important water reserves in the form of ground ice, rock glaciers are seen as increasingly important actors in the geomorphological and hydrological evolution of mountain systems, especially in the context of current climate change. Over geological timescales, rock glaciers both reflect paleoclimate conditions and transport rock boulders produced by headwall erosion and therefore participate in shaping high mountain slopes. However, the dynamics of rock glaciers and their evolution over different timescales remain under-constrained.

In this study, we adopt a multi-method approach including field observations, remote sensing, and geochronology, to investigate the rock glacier system of the Vallon de la Route (Combeynot massif, western French Alps). ~~Remote sensing employing image~~Remotely sensed images and correlation ~~documents~~techniques are used to document the displacement field of the rock glacier over ~~modern~~ timescales ~~(1-10^1 years). Over longer~~ranging from year to decades. Additionally, over periods ~~(10^3-10^4 years),~~from centuries to millennia, we employ terrestrial cosmogenic nuclide (~~^{10}Be in~~ quartz~~)~~ ^{10}Be) surface~~-~~exposure dating on rock~~-~~ boulder surfaces located along the central flow line of the rock glacier, targeting different longitudinal positions from the headwall to the rock~~-~~ glacier terminus.

The remote sensing analysis demonstrates that between 1960 and 2018, the two lower units of the rock glacier have been motionless, the transitional unit presents an integrated surface velocity of 0.03 ±0.02 m/a, and the two upper active units above 2600 m a.s.l. show velocity between 0.14 ±0.08 and 0.15 ±0.05 m/a. Our results show ^{10}Be surface-exposure ages ranging from ~~1.88 ±0.14 to~~ 13.10 ±0.51 to 1.88 ±0.14 ka. The spatial distribution of dated rock~~-~~ glacier boulders reveals a first-order inverse correlation between ^{10}Be surface-exposure age and elevation~~;~~, and a positive correlation with horizontal distance to the headwall. These observations support the hypothesis of rock boulders falling from the headwall and remaining on the glacier surface as they are transported down valley, ~~which thus can~~and may therefore be used to estimate rock~~-~~ glacier surface velocity

over geological timescales. Our results also suggest that the rock glacier is characterized by two major ~~episodes~~phases of activity. The first phase, starting around 12 ka, displays a ^{10}Be-age gradient ~~that suggests~~with a rock~~-~~ glacier surface velocity of about 0.45 m/a. Following a quiescent period between ca. 6.2 ~~ka~~ and 3.4 ka, before the emplacement of the present-day active upper two units~~ have been emplaced during climatic~~. Climatic conditions ~~favoring~~have favored an integrated rock-glacier motion ~~at~~of around 0.18 m/a~~. Those~~ between 3.4 ka and present day. These results allow us to quantify back~~ erosion~~-wearing rates of the headwall of between 1.0 and 2.5 mm/a, higher than catchment-integrated denudation rates estimated over millennial timescales~~, suggesting~~. This suggests that the rock~~-~~ glacier system promotes the maintenance of high rock~~-~~ wall erosion by acting as debris conveyor and allowing freshly exposed bedrock surfaces to be affected by erosion processes.

~~1 Introduction and motivations~~

~~Rock glaciers are important geomorphic structures influencing the evolution of high-elevation mountain environments. Being lobated or tongue-shaped assemblages of poorly-sorted, angular rock debris and ice, rock glaciers move as a consequence of the deformation of internal ice, conveying large calibre sediments from high-elevation steep slopes, cirque headwalls to their terminus at lower elevations (Barsch, 1977; Giardino and Vitek 1988). In the context of current climate change, rock glaciers are one of the most resilient cryospheric bodies in alpine environments (Jones et al., 2019). Indeed, they represent an important storage of water supply when pure-ice glaciers have disappeared (e.g., Williams et al., 2006; Jones et al. 2019). Over geological timescales, rock glaciers participate actively in the development of asymmetrical mountain crests by eroding and conveying rock from leeside headwalls (where rockfall is the primary source of debris) to lower elevations in the valley (Gilbert, 1904; Johnson et al., 1980). Although rock glaciers have received considerable attention in the last couple decades, being catalogued in several geographic areas (see Jones et al. 2019 for latest review), how rock glaciers form and evolve is still a subject of debate, with two main holistic views (see Haeberli et al. 2006; Berthling, 2011). On one hand, rock glaciers are seen as periglacial features in which ice grows into debris interstices, forming an ice-rock mixture that creeps by the influence of gravity and sufficient slope (e.g., Wahrhaftig and Cox, 1959; Ikeda et al., 2008). On the other hand, rock glaciers are thought to result from glacial remnants with a deforming ice core that are being protected by a continuous debris cover (e.g., Whalley, 1974; Anderson et al., 2018).~~

~~The development of rock glaciers is a long process taking few hundred to thousands of years (e.g., Berthling, 2011). Their morphology, activity and dynamics reflect present and past climates (i.e. temperature and precipitation fluctuations) and geomorphological forcing (rock and snow avalanching, bedrock structural patterns; Kellerer-Pirklbauer and Rieckh, 2016; Jones et al. 2019). Rock-glacier activity is categorized between active, transitional and relict modes, and has been recently updated based on geomorphological indicators (RGIK, 2021). An active rock glacier presents movement in most of its surface, although a transitional rock glacier will present low movement only detectable by *in-situ*/remote-sensing measurement and/or restricted to areas of non-dominant extent. Finally, a relict rock glacier has no detectable movement and no morphological evidence of recent movement and/or ice content (RGIK, 2021). Rock glaciers have been documented to accelerate with~~

~~increasing temperature (Delaloye et al., 2010; Cremonese et al., 2011; Kellerer-Pirklbauer, 2017; Wirz et al., 2016; Eriksen et al., 2018; Kenner et al. 2018; Marcer et al. 2021) but when the ice content falls below a critical saturation threshold, rock glaciers stop creeping, turning from active into transitional and eventually relict mode (Sandeman and Ballantyne, 1996). Their activity is also controlled by the geomorphology of the surrounding topography. For instance, it has been suggested that when the rock-boulder delivery rate and debris/ice incorporation from the headwall becomes insufficient to sustain the insulation of the ice-rich part, the activity of the rock glacier will decrease and stop regardless of the rock-glacier thermal state (Amschwand et al., 2021).~~

~~To better understand the relationships between external forcings and the activity of rock glaciers, and to assess how ongoing climate change has and will affect them, their past activity and in particular past vs. modern surface velocity estimates have to be quantified from annual to millennial timescales. Analytical advancements over the past decades have allowed significant progress of the remote-sensing tools monitoring landscape changes in high-mountain regions (e.g., Necsoiu et al., 2016; Vivero and Lambiel, 2019; Blöthe et al., 2021; Robson et al., 2020). Indeed, methods such as LiDAR (Micheletti et al., 2017), InSAR (i.e., Liu et al., 2013; Barboux et al., 2014; Strozzi et al. 2020), aerial photogrammetry (i.e., Cusicanqui et al., 2021) and unmanned aerial vehicle systems (i.e., Dall'Asta et al. 2017; Vivero and Lambiel 2019) have remarkably improved the temporal and spatial resolution of surface velocity surveys for rock glaciers. A recent study (Cusicanqui et al., 2021) in the western French Alps has shown the feasibility of using high-resolution digital elevation models (DEMs) and ortho-rectified images produced from combinations of historical aerial and satellite images to reconstruct the surface velocity of rock glaciers over the last seven decades. Extrapolations from short-term surface velocities have been used to estimate the rock-glacier formation time and to reconstruct their activity over longer timescales (e.g., Kaab et al., 1997; Bodin, 2013). However, it remains difficult to assess such extrapolations and to accurately constrain the long-term dynamics and morphological changes of rock glaciers without reliable estimates over centennial to millennial timescales.~~

~~To improve our understanding of rock-glacier long-term dynamics and potential forcing mechanisms, relative and absolute dating methods have been applied on both active and relict rock glaciers (e.g. Haeberli, 2013; Amschwand et al. 2021). In rare cases, radiocarbon dating has been used on lacustrine sediments or trees buried by rock glaciers (Paasche et al., 2007) or on vegetal macrofossils found in the permafrost of rock glacier (Krainer et al., 2015). Schmidt-hammer dating has been employed to date surface exposure for boulders from numerous rock glaciers (European Alps, Norway, Island and New Zealand) but such approach requires local calibration surfaces and often only provide relative dating (e.g., Böhlert et al., 2011; Scapozza et al., 2014; Matthews and Wilson, 2015; Winkler and Lambiel, 2018). Similarly, lichenometry has been applied successfully on rock glaciers with stable rock boulders at the surface, although absolute dating requires calibration of this technique (Konrad and Clark, 1998; Galanin et al., 2014). Optically stimulated luminescence has been used to quantify the travel time of buried fine sediments in rock glaciers (Swiss Alps), but large uncertainties potentially coming from pre-burial bleaching of fine sediments make this approach challenging to apply at larger scale (Fuchs et al., 2013).~~

~~Terrestrial cosmogenic nuclide (TCN) dating has been successfully applied to constrain the exposure time of rock boulders at the surface of relict rock glaciers and their stabilization in the European Alps (Hippolyte et al., 2009; Steinemann et al., 2020),~~

~~the Iberian Peninsula (Rodríguez-Rodríguez et al., 2017; Andrés et al., 2018; Palacios et al., 2020), Scotland (Sandeman & Ballantyne, 1996) and Iceland (Fernández-Fernández et al. 2020), demonstrating their potential as independent paleoclimate archives to reconstruct past permafrost development and disappearance (Andrés et al., 2018). Cossart et al. (2010) combined~~ ~~^{10}Be surface-exposure dating and weathering rind thickness to document three main generations of rock glaciers in the Southern French Alps. Recently, two studies (in Iceland and Switzerland) have applied TCN dating on rock glacier systems composed of both active and relict units (Fernández-Fernández et al. 2020; Amschwand et al., 2021), showing deactivation and stabilization of the rock glacier at lower elevations and further distance from the headwall.~~

~~The onset of rock-glacier development in the high-elevation parts of the European Alps is thought to have started after the onset of glacier retreat following the Last Glacial Maximum (around 19-18 ka in the European Alps, e.g., Wirsig et al., 2016 ; Monegato et al. 2017; Lehmann et al., 2020). Chronologies of rock-glacier development in the Alps of Austria, Central Switzerland and France have shown different rock-glacier generations: during the Lateglacial period (ca. 16 ka), during or shortly after the Younger Dryas (ca. 12 ka) and during the Late Holocene, probably at the end of Subboreal period (5.2/5.0 - 4.3/4.2 ka) when the high-elevation cirques became ice-free (Cossart et al., 2010; Amschwand et al., 2021; Steinemann et al., 2020; Charton et al. 2021).~~

~~In this study, we present the reconstruction of activity and surface velocities at different timescales for the rock-~~

1 Introduction and motivations

Rock glaciers are important geomorphic structures influencing the evolution of high-elevation mountain environments. They are lobated or tongue-shaped assemblages of angular rock debris and ice. Rock glaciers move by the deformation of internal ice, conveying large caliber sediments from high-elevation steep slopes, cirque headwalls to their terminus at lower elevations (Barsch, 1977; Giardino & Vitek, 1988). In the context of current climate change, rock glaciers are considered as one of the most resilient cryospheric bodies in alpine environments thanks to the insulated effect of their rocky carapace (Jones et al. 2019). Indeed, they represent an important storage of water supply when mountain glaciers have disappeared (e.g., Jones et al., 2019). However, in-situ measurements since the last decades have shown rock glacier acceleration and destabilization associated with increasing air temperature in the European alps (e.g., Marcer et al. 2021). Over geological timescales, rock glaciers participate actively in the development of asymmetrical mountain crests by conveying rock from leeside headwalls (where rockfall is the primary source of debris) to lower elevations in the valley (Gilbert 1904; Johnson, 1980). Although rock glaciers have received considerable attention in the last couple decades, being catalogued in several geographic areas (see Jones et al., 2019 for latest review), the formation and evolution of rock glacier are still a subject of debate, with two main holistic views (see Haeberli et al., 2006; Berthling, 2011). On the one hand, rock glaciers are seen as periglacial features in which ice forms, ice content increases within debris interstices, forming an ice-rock mixture that creeps by the influence of gravity and sufficient slope (e.g., Wahrhaftig & Cox, 1959; Ikeda et al., 2008). On the other hand, rock glaciers are thought to result from the remnants of glaciers with a deforming ice core that are being protected by a continuous debris cover (e.g., Whalley, 1974; Monnier and Kinnard 2015; Anderson et al., 2018).

The development of rock glaciers is a long process taking few decades to thousands of years (e.g., Berthling, 2011). Their morphology, activity and dynamics reflect present and past climates (i.e., temperature and precipitation fluctuations) and geomorphological forcing (rock and snow avalanching, bedrock structural patterns; Ikeda and Matsuoka, 2006; Kellerer-Pirklbauer & Rieckh, 2016; Jones et al., 2019). Rock glacier activity is categorized between active, transitional, and relict modes, and has been recently updated based on geomorphological indicators (Delaloye & Echelard, 2020). An active rock glacier presents movement in most of its surface whereas a transitional rock glacier will present low movement only detectable by *in-situ*/remote sensing measurement and/or restricted to non-dominant areas. Finally, a relict rock glacier has no detectable movement and no morphological evidence of recent movement and/or ice content (Delaloye & Echelard, 2020). Rock glaciers have been documented in the European Alps to accelerate with increasing temperature (Delaloye et al., 2010; Kellerer-Pirklbauer, 2017; Wirz et al., 2016; Eriksen et al., 2018; Kenner et al., 2018; Marcer et al., 2021) but when the ice content falls below a critical saturation threshold, rock glaciers stop creeping, turning from active into transitional and eventually relict mode (Sandeman & Ballantyne, 1996). Their activity is also controlled by the geomorphology of the surrounding topography. For instance, it has been suggested that when the rock boulder delivery rate and debris/ice incorporation become insufficient to sustain the insulation of the ice-rich part, the activity of the rock glacier will decrease and stop regardless of the rock glacier thermal state (Amschwand et al., 2021).

The relationships between external forcings and the activity of rock glaciers need to be better understand. Consequently, their past activity and in particular past vs. modern rock glacier surface velocity estimates must be quantified from annual to millennial timescales. This will allow us to assess how ongoing climate change has and will affect rock glaciers. Analytical advancements over the past decades have allowed significant progress based on remote sensing tools for monitoring changes on high-mountain landforms (e.g., Necsoiu et al., 2016; Vivero & Lambiel, 2019; Blöthe et al., 2021; Robson et al. 2022). Indeed, methods such as LiDAR (Micheletti et al., 2017), InSAR (i.e., Liu et al., 2013; Barboux et al., 2014; Strozzi et al., 2020), aerial photogrammetry (i.e., Kaab et al., 1997) and unmanned aerial vehicle systems (i.e., Dall'Asta et al., 2017; Vivero & Lambiel, 2019) have remarkably improved the temporal and spatial resolution of surface velocity surveys for rock glaciers. Recent studies have shown the feasibility of using high-resolution digital elevation models (DEMs) and ortho-rectified images produced from historical aerial and satellite images to reconstruct the surface velocity of rock glaciers over the last seven decades (Fleischer et al. 2021; Vivero et al. 2021; Kääb et al. 2021; Cusicanqui et al., 2021). Extrapolations from short-term surface velocities have been used to estimate the rock glacier formation time and to reconstruct their activity over longer timescales (Kaab et al., 1997; Frauenfelder and Kääb, 2000; Bodin, 2013). However, it remains difficult to assess such extrapolations and to accurately constrain the long-term dynamics and morphological changes of rock glaciers without reliable estimates over centennial to millennial timescales.

To improve our understanding of rock glacier long-term dynamics and potential forcing mechanisms, relative and absolute dating methods have been applied on both active and relict rock glaciers (e.g., Haeberli, 2013; Amschwand et al., 2021). In rare cases, radiocarbon dating has been used on lacustrine sediments or trees buried by rock glaciers (Paasche et al. 2007) or on vegetal macrofossils found in old permafrost cores from a rock glacier (Krainer et al. 2015). Schmidt-hammer methods have been employed to estimate the surface exposure age of boulders from numerous rock glaciers (European Alps, Pyrenees, Norway, Island and New Zealand) but such an approach requires local calibration surfaces and often only provides relative dating (e.g., Böhlert et al., 2011; Scapozza et al., 2014; Matthews & Wilson, 2015; Winkler & Lambiel, 2018). Similarly, lichenometry has been applied successfully on rock glaciers with stable rock boulders at the surface, although absolute dating requires calibration of this technique (Konrad and Clark, 1998; Galanin et al., 2014). Optically stimulated luminescence has been used to quantify the travel time of buried fine sediments in rock glaciers (Swiss Alps), but large uncertainties potentially coming from pre-burial bleaching of fine sediments make this approach challenging to apply at larger scale (Fuchs et al. 2013). Terrestrial cosmogenic nuclide (TCN) dating has been successfully applied to constrain the exposure time of rock boulders at the surface of relict rock glaciers and their stabilization in the European Alps (Hippolyte et al., 2009; Steinemann et al., 2020), the Iberian Peninsula (Rodríguez-Rodríguez et al., 2017; Andrés et al., 2018; Palacios et al., 2020; García-Ruiz et al. 2000), Scotland (Sandeman and Ballantyne, 1996) and Iceland (Fernández-Fernández et al., 2020), demonstrating their potential as independent paleoclimate archives to reconstruct past permafrost development and to identify activity phases of rock glacier (Andrés et al. 2018). Cossart et al. (2010) combined ^{10}Be surface-exposure dating and weathering rind thickness to document three main generations of rock glacier in the Southern French Alps. Recently, two studies (in Iceland and Switzerland) have applied TCN dating on rock glacier systems composed of both active and relict units (Fernández-Fernández et al., 2020; Amschwand et al., 2021), showing deactivation and stabilization of the rock glacier at lower elevations and further distance from the headwall.

The onset of rock glacier development in the high-elevation parts of the European Alps is thought to have started after the onset of glacier retreat following the Last Glacial Maximum (around 19-18 ka in the European Alps, e.g., Ivy-Ochs, 2015; Monegato et al., 2017; Lehmann et al., 2020). Chronologies of rock glacier development in the Alps of Austria, Central Switzerland and France have shown different rock glacier generations: during the Lateglacial period (ca. 16 ka; Steinemann et al. 2020), during or shortly after the Younger Dryas (ca. 12 ka; Cossart et al. 2010; Steinemann et al. 2020; Charton et al., 2021) and during the Late Holocene (Amschwand et al. 2021), probably at the end of Subboreal period (5.2/5.0 - 4.3/4.2 ka; Cossart et al., 2010) when the high-elevation cirques became ice-free.

The goal of this study is to reconstruct the activity and the surface velocities at different timescales of the rock glacier system of the Vallon de la Route (Combeynot massif, western French Alps). ~~Remote~~A remote-sensing ~~methods such as~~approach utilizing image correlation over photogrammetric products ~~allow~~allows us to reconstruct the surface ~~displacements~~displacement field of the rock glacier over the last six decades. Over longer periods (10^3 to 10^4 years), we apply TCN dating (quartz ^{10}Be) to rock~~-~~ boulder surfaces at different positions along the central flow line of the rock glacier, from ~~the headwall~~its terminus to its ~~terminus~~highest part, allowing the conversion of the ^{10}Be surface-exposure ages into long-term surface displacement estimates. By discussing our estimates of rock~~-~~ glacier surface kinematics at different timescales, we

Formatted: English (United States)

show that it is possible to reconstruct the history of past activity of the rock glacier, and to use rock glaciers as independent paleoclimate and paleo-geomorphological ~~archives~~proxies revealing the evolution of alpine environments.

2 Study site

~~The Combeynot massif (45°0N - 6°2E) represents the north-eastern part of the Ecrins Pelvoux massif, located in the western French Alps (Fig. 1a). The Ecrins Pelvoux massif presents high alpine topography, with summits above 4000 m a.s.l. and valley bottoms around 1000-1500 m a.s.l. Widespread U-shaped valley profiles, hanging valleys and glacial trimlines illustrate the imprint of Quaternary glaciations on the massif (Delunel et al., 2010; Valla et al., 2010; Le Roy et al., 2017). Paleo-glacier reconstructions since the Last Glacial Maximum have been previously constrained using mapping, interpolation of glacial features and TCN dating applied on moraine deposits and glacially-polished bedrock surfaces (Delunel, 2010). Evidence for Younger Dryas stadial readvances have been mapped and dated in several catchments of the massif (e.g., Coûteaux and Edouard, 1987; Chenet et al., 2016; Charton et al., 2021). Based on surface-exposure dating of moraine deposits, few glacial advances during the Holocene and more precisely during the Neoglacial (from ca. 4.3 ka) have been reconstructed (Le Roy et al., 2017 ; Shimmelpfennig et al., 2019, unpublished data ; Schoeneich et al., 2019, unpublished data). Modern glacierization is characterized by small cirque and slope ice bodies covering 68.6 km^2 in 2009 (Gardent et al., 2014). The two largest valley glaciers remaining today are the Girose Glacier (5.1 km^2) and the Glacier Blanc (4.8 km^2); most of the other glaciers are cirques or debris covered (Gardent et al., 2014; Fig. 1b in Le Roy et al., 2017).~~

~~Ranging from 1670 to 3155 m a.s.l., the Combeynot massif hosts 33 active and transitional rock-glacier systems and 38 relict rock glaciers (Bodin, 2013). These landforms range between 2000 and 2850 m a.s.l.; the root-zones mean elevation of the active rock glaciers is about 2700 m a.s.l., whereas the mean elevation of their frontal positions is 2620 m a.s.l. (Bodin, 2013). The Laurichard rock glacier, on the northern side of the Combeynot massif (Fig. 1a), is the site of one of the longest geodetic surveys for surface velocity in the European Alps (from the late 1970s; Francou and Reynaud, 1992; Thibert et al., 2018).~~

~~The Combeynot massif represents a slice of granitic intrusion confined in volcanic-sedimentary gneiss; a flysch layer of the ultra-Dauphinoise zone locally covers its eastern side (Barbier et al., 1973). The characteristic macro-crystalline scale fragility of the crystalline bedrock can be related to Pre-Hercynian hydrothermal activity. A network of NNW/SSE faults and a high density of diaclases cut the Combeynot massif, producing meter and sub-meter scale jointing of the bedrock (Francou and Reynaud, 1992). Thick superficial deposits (mostly coarse material) are the consequence of gravitational and nivo-periglacial processes (cryoclastic and avalanche activity; Francou, 1982).~~

~~From a present-day climatic point of view, the Combeynot massif is located in the transition zone between areas with a Mediterranean climate and areas with a more oceanic climate. Consequently, the local climatic setting is characterized by western frontal incursions and rainfall coming from the Italian side of the Alps and summer periods with low rainfall (Bodin, 2013). Regionally-available datasets (1971-2000) from weather stations located between 1324 and 2550 m a.s.l. suggest that monthly air temperatures are negative over 4 months of the year at 2000 m a.s.l., and over 8 months of the year at 3000 m a.s.l.~~

~~Also, for the 1961-1990 period, mean annual 0°C and −2°C isotherms were located at 2560 m a.s.l. and 2910 m a.s.l., respectively (Bodin, 2013).~~

The Combeynot massif (45°0N - 6°2E) represents the north-eastern part of the Ecrins Pelvoux massif, located in the western French Alps (Figure 1a). The Ecrins Pelvoux massif presents high alpine topography, with its highest summit being the only one above 4000 m a.s.l. (Barre des Ecrins, 4101 m a.s.l.) and valley bottoms around 1000-1500 m a.s.l. Widespread U-shaped valley profiles, hanging valleys and glacial trimlines illustrate the imprint of Quaternary glaciations on the massif (Delunel et al., 2010; Valla et al., 2010; Le Roy et al., 2017). Paleo-glacier reconstructions since the Last Glacial Maximum have been previously constrained using mapping, interpolation of glacial features and TCN dating applied on moraine deposits and glacially-polished bedrock surfaces (Delunel, 2010). Evidence for Egesen stadial readvances (the alpine counterpart of the Younger Dryas) have been mapped and dated in several catchments of the massif (e.g., Coûteaux & Edouard, 1987; Charton et al., 2021; Chenet et al., 2016; Hofmann et al. 2019). Based on surface-exposure dating of moraine deposits, glacial advances in the Ecrins Pelvoux massif have been identified from the Lateglacial to the Early Holocene (around 11 ka, Hofmann et al. 2019). Glacial advances during the Neoglacial (from ca. 4.3 ka) have also been reconstructed (Le Roy et al., 2017). Modern glacierized terrain is characterized by small cirque and slope ice bodies covering 68.6 km^2 in 2009 (Gardent et al., 2014). The two largest valley glaciers remaining today are the Girose Glacier (5.1 km^2) and the Glacier Blanc (4.8 km^2); most of the other glaciers are cirques or debris covered (Gardent et al., 2014; Figure 1b in Le Roy et al., 2017).

Ranging from 1670 to 3155 m a.s.l., the Combeynot massif hosts 33 active and transitional rock glacier systems and 38 relict rock glaciers (Bodin, 2013). These landforms range from 2000 to 2850 m a.s.l.; the mean elevation of the rooting zones of active rock glaciers is about 2700 m a.s.l., whereas the mean elevation of their frontal positions is 2620 m a.s.l. (Bodin, 2013). The Laurichard rock glacier, on the northern side of the Combeynot massif (Figure 1a), is the site of one of the longest geodetic surveys for surface velocity in the European Alps (since the late 1970s; Francou & Reynaud, 1992; Thibert et al., 2018).

The Combeynot massif comprises a slice of granitic intrusion confined in volcanic-sedimentary gneiss; a flysch layer of the ultra-Dauphinoise zone locally covers its eastern side (Barbier et al., 1973). The characteristic macro-crystalline scale fragility of the crystalline bedrock can be related to Pre-Hercynian hydrothermal activity. A network of NNW/SSE faults and a high density of diaclases cut the Combeynot massif, producing meter and sub-meter scale jointing of the bedrock (Francou & Reynaud, 1992). Thick superficial deposits (mostly coarse material) are the consequence of gravitational and nivo-periglacial processes (cryoclastic and avalanche activity; Francou, 1982).

From a present-day climatic point of view, the Combeynot massif is located in the transition zone between areas influenced by the Mediterranean climate and areas with a more Atlantic climate. Consequently, the local climatic setting is characterized by western frontal incursions and rainfall coming from the Italian side of the Alps and summer periods with low rainfall (Bodin, 2013). Cusicanqui et al. (2021) have performed weather reanalysis of data provided by the S2M (SAFRAN data from Durand, Giraud, et al., 2009; Durand, Laternser, et al., 2009; Vernay et al., 2020). Their results show annual average temperature of 1.3 ±0.76°C and snowfall of 791 ±169 mm/yr for the period 1958-2018 at the Laurichard site (elevation 2400 m a.s.l., northern exposure, 20° slope; Cusicanqui et al., 2021). The average air temperature for the 1958–1990 period is 1.0 against 1.7°C for the period 1991–2018, revealing a change trend of +0.23°C per decade (Cusicanqui et al., 2021). Inversely, the mean number of days of snow cover during winter went from 221 for the 1958-1990 period to 200 for the 1990-2018 period (Cusicanqui et al., 2021).

The Vallon de la Route catchment is occupied by neither debris-free nor debris-covered ~~glacier~~glaciers, but is sheltering a rock~~-~~ glacier system of about ~~6.74×10^5 m^2~~0.674 km^2. The total catchment area is about 4.41~~$\times10^6$ m^2~~ km^2, is southwest facing and ranges from 1960 to 3155 m a.s.l. It is bounded upstream by the highest peaks of the massif, the Tete de Pradieu (2879 m a.s.l.), the Roc Noir de Combeynot (3112 m a.s.l~~.),~~.) and the West Pic of Combeynot (3155 m a.s.l~~.) and the Tete de Pradieu (2879 m a.s.l.),~~ .), and downstream by the torrent of the Rif de la Planche (~~Figs.~~Figures 1a~~ and 1b~~-b). The rock~~-~~ glacier system is overhung by a debris source with area of about 5.351 $\times10^5$ m^2 ~~(estimated horizontal projection of the surface)~~ composed of leucogranitic bedrock (~~Fig.~~Figure 1b). Geoelectrical measurements (performed in 2006) on the rock glacier have shown that the active layer reaches a maximum thickness of 9 m at 2630 m a.s.l~~.~~., and that the ice-rich layer does not exceed 15 m and may consist of ice-cemented debris, with occasional layers of higher ice contents ~~(Bodin, 2013). The rock-glacier system of the Vallon de la Route (Fig.~~(Bodin, 2013). The rock glacier system of the Vallon de la Route (Figure 1) was chosen because it presents the ideal attributes of a rock glacier for this study, namely (i) it has an active snout and sharp edges, (ii) its total length of order of 1 km long, (iii) its situation in the middle of a valley, and (iv) it has one single bedrock type in the headwall source (i.e., leucogranite).

3 Methods

A multi-method approach combining geomorphological mapping and identification, remote sensing, and geochronology was used to reconstruct the history of activity of the rock glacier system of the Vallon de la Route (Combeynot massif, western French Alps).

3.1 ~~Field observations~~Geomorphological mapping/identification and image correlation

3.1.1 ~~Field observations~~Geomorphological mapping/identification

Geomorphological recognition was performed using the protocol described in the "Towards standard guidelines for inventorying rock glaciers, Baseline concepts" of the International Permafrost Association Action group for rock glacier inventories and kinematic ~~(RGIK, 2020).~~(RGIK 2020). *In-situ* visual inspection such as observation of the steepness of the front, description of ridge and furrow topography, size and shape distribution of the debris cover, together with ~~DEM~~using a high-resolution LiDAR Digital Surface Model (DSM, 0.5-m resolution) survey realized by SINTEGRA and landscape image analysis, were performed to geomorphologically classify the different landforms and their connection with each other. Five ~~different~~ units (I, II, III, IV and V) were identified from ~~top to~~ bottom to top according to *in-situ* geomorphological observations such as their elevation, their slope, their vegetation cover, the continuity, and apparent activity of their landforms (elevation, average slope and covered area were determined using the 0.5-m LiDAR high resolution ~~DEM; Figs.~~DSM; Figures 1, 2, 3 and 4). Units are separated by either ridge and furrow topography or front, which are the expression of the gravity-driven buckle folding of rock glacier morphology ~~(Frehner et al., 2015). In the present study, we focus our sampling strategy on 13 landforms (ridges) annotated from A to M (Table 1 and Fig. 5~~(Frehner et al., 2015). In the present study, we focus our sampling strategy on 13 ridges annotated from A to M (Table 1 and Figures 2 and 6).

3.1.2 Orthomosaic production

The reconstruction of the rock~~-~~ glacier surface displacement over decade timescales ~~was~~is done using ~~the~~ image correlation protocol ~~developed by Cusicanqui et al. (2021). We~~between different orthomosaics. Here, we compared timeseries of ~~4~~2 different ~~orthorectified images (1952,~~ orthomosaics (1960~~, 1989~~ and 2018). The ~~3~~ oldest ~~ones were~~one, acquired on August 22, 1960, was generated using historical aerial photographs (~~1952, 1960, 1989~~ with ~~2~~3 black and ~~3~~white film images~~, respectively~~ of 0.59 m of resolution) collected from the French National Institute of Geographic Information and Forestry (IGN, www.remonterletemps.ign.fr). ~~Orthomosaics were computed with Agisoft Metashape (version 1.6) software using ground control points (GCPS, between 12 and 18 depending of the year) with coorinates collected from the IGN map service (www.geoportail.fr) and elevations using a high-resolution LiDAR DSM (0.5 m resolution) survey realized by SINTEGRA (2012).~~

~~For the latest period, the orthorectified image of 2018 was computed using stereo Pleaides high-resolution acquisition using Ames Stereo Pipeline (ASP) (Shean et al., 2016).~~The orthomosaic of 2018 was computed using 3 stereo Pléaides 0.7-m resolution acquisition (acquired on August 12, 2018) using Ames Stereo Pipeline (ASP) (Shean et al. 2016). ASP uses rational polynomial coefficients (RPCs) provided with the Pléaides images, eliminating the requirement of a large number of high ~~accuracies GCPs. The DEMs and orthoimage were then co-registered using previous LiDAR high-resolution DEM and following Nuth and Kääb, (2011) methodology, the orthoimage was then shifted (translation-only) with co-registration values (x, y and z displacements). All original orthomosaics were resampled at a 0.5~~ accuracy GCPs (ground control points). Orthomosaics were computed with Agisoft Metashape (version 1.6) software using ground control points (the same 14 GCP for both orthomosaics) with coordinates collected from the IGN map service (www.geoportail.fr) and elevations using a high-resolution LiDAR DSM (0.5-m resolution) survey realized by SINTEGRA (August 17, 2012). Details on coordinates of the GCPs are given in Figure A1 and Table A1. The orthomosaics were then co-registered using previous LiDAR high-resolution DSM and following Nuth & Kääb (2011) methodology, they were then shifted (translation-only) with co-registration values (x and y displacements). All original orthomosaics were resampled at a 0.5-m resolution and set in a common 3465 × 3541-pixel grid system.

3.1.~~2~~3 Image correlation for surface displacement measurement

~~2D displacements of the rock glacier between orthomosaic pairs (1952, 1960, 1989 2018) were computed using the IMCORR module within the SAGA toolbox in QGIS (Scambos et al., 1992). The feature-tracking algorithm retrieves pixel patterns between two georeferenced images and attempts to match small subscenes (called ‘chips’) and produces shapefiles (points and lines) containing the 2D surface displacements. The program uses a fast Fourier transform-based version of a normalized cross-covariance method (Scambos et al., 1992). In the present study, several parameters of the algorithm were tested before settling on the following: search chip size = 64 pixels; reference chip size = 32 pixels; grid space = 4 m for the pair 1952-1960; 1960-1989 and 1989-2018. The 2D displacement of the 1960-2018 pair, giving the most accurate results regarding the largest time difference, was calculated using the following parameters: search chip size = 128 pixels; reference chip size = 64 pixels; grid space = 10 m.~~

The 2D displacements of the rock glacier between orthomosaic pairs (1960 and 2018) were computed using the IMCORR module within the SAGA toolbox in QGIS (Scambos et al., 1992). The feature-tracking algorithm retrieves pixel patterns between two georeferenced images and attempts to match small subscenes (called ‘chips’) and produces shapefiles (points and lines) containing the 2D surface displacements. The program uses a fast Fourier transform-based version of a normalized cross-covariance method (Scambos et al., 1992). In the present study, several parameters of the algorithm were tested before settling on the following: search chip size = 128 pixels; reference chip size = 64 pixels; grid space = 10 m.

The obtained surface displacements were first filtered with a threshold of 100 pixels for error on x and y direction estimates (IMCORR xerr and yerr values) removing about 1% of the initial values. We then manually filtered according to (a) different local spatial coverage and artifacts (e.g., related to random local similarity of the coarse blocky surface; ~~Bodin et al. 2018),~~Bodin et al., 2018), (b) lack of consistency of the displacement between neighboring vectors (difference >30°), and (c) outlier displacement values ~~(Cusicanqui et al., 2021).~~(Cusicanqui et al., 2021). Finally, 5.4% of the points were removed~~ for the pair 1960-2018.~~. The ±1σ variability is calculated using all the pixels for each unit together with the median displacement. ~~The~~ The quality of the results mentioned above is assessed through two analyses. First, the displacements obtained on the rock~~-~~glacier system are compared to the measured displacements of ~~a~~6 control ~~area selected to be within stable terrain of about 1.25×10^4 m^2 below the lower part of the rock glacier,~~areas where no displacement should be observed~~ (dashed outlined area in Fig. 2). This~~. Details of those control ~~area has been~~ areas are given in Figures 3, A1, A2 and Table A3. These control areas were chosen to be outside of and around the rock~~-~~ glacier system~~,~~ and out of the scree field~~ and with local slopes <30°.~~. The absence of movement (solifluction, creeping, landsliding) ~~has been~~was determined by visually inspecting historical aerial photographs collected from the IGN-France and the two orthomosaics. In a second time, the potential mismatchs between 11 control points between the two orthomosaics have been manually measured. Those manual control points were chosen on topographic features of the surface of our studied area (blocks, cliff structures) and their stability was estimated using the historical aerial photographs collected from the IGN-France.

3.2 ^{10}Be surface-exposure dating

TCN surface-exposure dating is based on the observation that when cosmic rays reach the Earth's surface, they produce cosmogenic isotopes in specific targets, such as the production of Beryllium-10 (^{10}Be) in quartz minerals (e.g., Gosse & Phillips, 2001; Lifton et al., 2014). The in-situ production of ^{10}Be in quartz occurs predominantly within a few meters of Earth's surface and decreases exponentially with depth such that by knowing a measured concentration of ^{10}Be in the first centimetre of a rock surface and the local production rate of ^{10}Be in such a rock, it is possible to calculate an apparent surface exposure age (Portenga and Bierman, 2011). In this section, we detail how samples were collected, prepared, and analyzed, and we explain how external processes affecting the dataset can be estimated.

3.2.1 Sampling

~~We~~ The samples were collected ~~19 rock-boulder samples~~ with approximately 0.5 kg of rock material from the 13 ~~landforms~~ridges of interest (Tables 1 and 2; ~~Fig. 3~~Figure 6). For 6 of these ~~landforms (B, C, E~~ridges (A, D, G, ~~J~~I, K and ~~M~~L, Table 1 and Figure 6) two different boulders were sampled ~~in order~~ to evaluate the reproducibility of our dating approach (~~Fig.~~Figure 2c). The boulders were chosen following the central flow line which was defined to be both at the ~~centre~~center of the rock glacier width and perpendicular to the main ridge and furrow ~~topography landforms (black line~~topographic ridges (red lines in ~~Fig.~~Figures 3 and ~~Fig. 5~~6), from the terminus to the high-elevation active lobes ~~to the terminus~~ of the rock glacier system. Sampled boulders were chosen on the top of the ridges to minimize topographic shielding, snow-cover effect, and complex exposure ~~histoires (covering of~~histories (i.e., sediment ~~and clasts~~or clast cover, late exhumation; ~~Fig.~~Figures 2c-d). Suitable boulders are large (>1.5 m) and in a stable position (~~Figs.~~Figures 2c~~ and 2d~~-d). Appropriate rock surfaces do not show ~~sign~~signs of intense weathering or recent chipping. Sampling was done using a hammer, a chisel, and a small electric circular saw ~~during~~over 4 days (28/09/20-01/10/20). The sampling details of each rock boulder including coordinates, elevation, distance to the headwall, height of the sample from the ground, size of the boulder and topographical shielding are summarized in Tables 1 and 2.

~~3.2.2 TCN preparation and ^{10}Be measurement~~

~~Samples were crushed and sieved to retain the 200-500-µm grainsize fraction. Beryllium extraction was performed at the GTC platform (ISTerre, France) using a chemical protocol adapted from Brown et al. (1991) and Merchel and Herpers (1999). Magnetic separation was used to isolate the quartz fraction, followed by successive leaching in an H_2SiF_6/HCl mixture. In order to speed up the purification of quartz and save leaching cycles, magnetic separation with fine magnetite powder was performed between leaching cycles, to remove partially altered minerals. Meteoric Be purification was achieved with three sequential dissolutions using diluted HF (Kohl and Nishiizumi, 1992). The purified quartz samples (13-26 g for each individual sample) were completely dissolved in concentrated HF after being spiked with ~510 mg of a 998 mg/L Be carrier solution (Scharlab ICP Standard, batch 16107901) in order to fix the ^{10}Be/^{9}Be ratio (Table 2). After HF evaporation, perchloric and~~

~~nitric acids were added and evaporated to remove organic compounds and fluorides. Beryllium was extracted by successive alkaline precipitations of Be(OH)$_2$ alternated with separation on anion and cation columns. Samples were then oxidized at 700°C for 1h and the final BeO mixed with Nb powder and loaded into nickel cathodes. ^{10}Be concentration were measured at ASTER national facility (Cerege, France) against standard BeO_STD-11 (1.191 ±0.013×10^{11}; Braucher et al., 2013) and were corrected for the full process blank with a ^{10}Be/^{9}Be ratio of 6.278 ±0.534×10^{-15}.~~

~~3.2.3.~~3.2.2 TCN preparation and ^{10}Be measurement

Samples were crushed and sieved to retain the 200-500-µm grainsize fraction. Beryllium extraction was performed at the GTC platform (ISTerre, France) using a chemical protocol adapted from Brown et al. (1991) and Merchel & Herpers (1999). Magnetic separation was used to isolate the quartz fraction, followed by successive leaching in an H_2SiF_6/HCl mixture. In order to speed up the purification of quartz and save leaching cycles, magnetic separation with fine magnetite powder was performed between leaching cycles, to remove partially altered minerals. Meteoric Be purification was achieved with three sequential dissolutions using diluted HF (Kohl & Nishiizumi, 1992). The purified quartz samples (13-26 g for each individual sample) were completely dissolved in concentrated HF after being spiked with ~510 mg of a 998 mg/L Be carrier solution (Scharlab ICP Standard, batch 16107901) to fix the ^{10}Be/^{9}Be ratio (Table 2). After HF evaporation, perchloric and nitric acids were added and evaporated to remove organic compounds and fluorides. Beryllium was extracted by successive alkaline precipitations of Be(OH)$_2$ alternated with separation on anion and cation columns. Samples were then oxidized at 700°C for 1h and the final BeO mixed with Nb powder and loaded into nickel cathodes. ^{10}Be concentration were measured at ASTER national facility (Cerege, France) against standard BeO_STD-11 (1.191 ±0.013×10^{11}; Braucher et al., 2013) and were corrected for the full process blank with a ^{10}Be/^{9}Be ratio of 6.278 ±0.534×10^{-15}.

3.2.3 Surface-exposure age calculation

Surface-exposure ages were computed with the CREp online calculator (Martin et al., 2017) using the LSD scaling scheme (Lifton et al., 2014), the ERA40 atmospheric model (Uppala et al., 2005) and the Lifton VDM 2016 geomagnetic database (Pavón-Carrasco et al., 2014). We used the Chironico landslide production rate (with sea-level high-latitude value of 4.16 ±0.10 atoms g/a; Claude et al., 2014), scaled according to the sample longitude, latitude and elevation.

The production rate was corrected for sample thickness (Table 2) and density (2.75 g/cm^3). Shielding correction includes the topographic shielding due to surrounding landscape and the dip of the sampled surface calculated with the online calculators CRONUS-Earth (Balco et al., 2008, http://hess.ess.washington.edu/math). In addition, we explore the influence of snow-cover attenuation using the (Gosse & Phillips, 2001) equation with snow density of 0.3 g/cm^3 and an attenuation length for fast neutrons in snow of 150 g/cm^2 (Delunel et al., 2014). According to a previous study dating a rock avalanche less than 1 km north of our site (Chenet et al. 2016), we use an estimate of 50 cm cover of snow for 6 months of the year, values that are most often cited in the literature for the Alpine regions for these altitudes (Hormes et al., 2008; Susan Ivy-Ochs et al., 2006; Kelly et al., 2004; Schindelwig et al., 2012; Wirsig et al., 2016; Chenet et al., 2016).

3.2.4 Inheritance/pre-exposure estimation

The measured ^{10}Be concentrations of rock glacier boulder surfaces should always be interpreted with caution as multiple external processes can affect them. Surface erosion can cause a depletion of ^{10}Be concentration at the rock boulder surface, as can complex exposure histories (discontinuous exposure, snow/sediment cover), both of which would lead to an underestimation of the "accurate" ^{10}Be surface-exposure age. Note that, in this study we do not consider the effect of boulder surface erosion; consequently, our reported ^{10}Be surface-exposure ages must be seen as minimum estimates. On the other hand, inheritance (i.e., headwall pre-exposure before rock collapse on the rock glacier), will lead to overestimation of the ^{10}Be surface-exposure age. We choose two approaches to quantify the potential inheritance/pre-exposure bias. The first one is to use linear regression between ^{10}Be surface exposure age and distance to the headwall. Without inheritance, boulders located at the contact between the headwall and the talus slope (distance to the headwall equals to zero) should have a negligible ^{10}Be concentration. Any ^{10}Be concentration given by linear regression at the headwall would be interpreted as time spent (inheritance) in the cliff before the rock fall event. The second approach is to compare the ^{10}Be concentration of samples collected on the same ridge. Any difference in ^{10}Be concentration could be interpreted as a difference in time spent on the cliff face before the rock fall event. In this case, the inheritance time is calculated using the ^{10}Be concentration difference between replicates using the ^{10}Be production rate at the elevation of 2997 m a.s.l. (corresponding to the middle elevation of the cliff source).

3.3 Surface velocity estimation

Armed with both geochronological and remote sensing datasets, the time-averaged surface velocity of the rock glacier system can be estimated. When considering ^{10}Be surface-exposure dating, the mean surface speeds are calculated by dividing the distance to the headwall of either the individual sample or the unit (mean distance to the headwall evaluated at all pixels inside within the unit limits) by their corresponding individual or median ^{10}Be surface-exposure ages. Here we assumed that the ^{10}Be surface-exposure age represents exposure between the time of the rockfall event that delivered the block to the surface of the headwall/talus transition and its arrival at the sample site. ~~Surface-exposure ages were computed with the CREp online calculator (Martin et al., 2017) using the LSD scaling scheme (Lifton et al., 2014), the ERA40 atmospheric model (Uppala et al., 2005) and the Lifton VDM 2016 geomagnetic database (Pavón-Carrasco et al., 2014). We used the Chironico landslide production rate (with sea-level high-latitude value of 4.16 ±0.10 atoms.g/qtz/a; Claude et al., 2014), scaled according to the sample longitude, latitude and elevation.~~

~~The production rate was corrected for sample thickness (Table 2) and density (2.75 g cm^{-3}). Shielding correction includes the topographic shielding due to surrounding landscape and the dip of the sampled surface calculated with the online calculators CRONUS-Earth (Balco et al., 2008, http://hess.ess.washington.edu/math). In addition, we explore the influence of snow-cover attenuation using the Gosse and Phillips (2001) equation with snow density of 0.3 g/cm^3 and an attenuation length for fast neutrons in snow of 150 g/cm^2 (Delunel et al., 2014). According to a previous study dating a rock avalanche less than 1 km north of our site (Chenet et al., 2016), we use an estimate of 50 cm cover of snow for 6 months of the year, values that are most often cited in the literature for the Alpine regions for these altitudes areas (Hormes et al., 2008; Ivy-Ochs et al., 2006; Kelly et al., 2004; Schindelwig et al., 2012; Wirsig et al., 2016; Chenet et al., 2016). We do not consider the effects of boulder surface erosion, consequently reported ^{10}Be surface-exposure ages must be seen as minimum estimates but according to the age range they can be considered as the time duration of boulders on the rock glacier.~~

In contrast, the modern velocities derived from remote sensing analysis are calculated by dividing the measured displacement or the median values for each unit, by the time between the two orthomosaics, in this case 58 years (1960-2018 period).

4 Results

According to the geomorphological mapping and identification approach described in section 3.1.1, the rock glacier system was divided into five different units, in which we apply the approach presented above to reconstruct the chronology of the rock glacier displacement since the onset of the Holocene.

4.1 Field observations

~~Unit I (ranging from 2867 and 2685 m a.s.l.) and unit~~At the lower part of the rock glacier system, the units I and II, with elevation ranges of 2585-2521 and 2718-2557 m a.s.l., respectively (and covering about 0.214 and 0.177 km^2, respectively), clearly display relict morphologies with no geomorphological evidence of recent surface movement. Their metric to pluri-metric debris layers are highly covered by superficial material and vegetation (Figures 2c). The unit III, spanning from 2685 to 2556 m a.s.l. and covering 0.155 km^2, was evaluated to be transitional. Indeed, the evidence of downslope movement is less visible (but still detectable) than for units IV and V, as the ridge-and-furrow topography is less prominent. The unit IV (ranging from 2735 and 2626 m a.s.l.) and the unit V (ranging from 2867 and 2685 m a.s.l.) were classified as active and cover areas of about ~~7.29~~0.542 and ~~5.42 ×10^5 m^2~~0.729 km^2, respectively. They ~~present~~display evidence of downslope creep movement such as steep fronts~~ (steeper than the angle of repose),~~, strongly marked ~~ridges~~ridge-and-~~furrows~~furrow topography, absence of vegetation cover and active layers composed of decimetric to metric angular debris. These two units are talus-connected, meaning that they are part of a downslope sequence including headwall – talus slope – rock glacier (~~Figs.~~Figures 2a-b). The delivery of debris is likely accomplished by rockfall activity, surface runoff, debris flow and/or avalanche events from the headwall bedrock. ~~The horizontal limit between the talus slope and rock-glacier units is determined with about 50 m of~~

~~uncertainty. Unit III, spanning from 2685 to 2556 m a.s.l. and covering 1.550 ×10^5 m^2, was evaluated to be transitional. Indeed, the evidence of downslope movement is less visible (but still detectable) than for units I and II, the ridge-and-furrow topography is less prominent. Finally, units IV and V, with elevation ranges of 2718-2557 and 2585-2521 m a.s.l., respectively (and covering about 1.776 ×10^5 and 2.147 ×10^5 m^2, respectively), clearly display relict morphologies with no geomorphological evidence of recent surface movement. Their metric to pluri-metric debris layers are highly covered by superficial material and vegetation.~~The horizontal limit between the talus slope and rock glacier units can be estimated with about 50 m of uncertainty. This top to bottom organization from active, to transitional and relict units is common in alpine settings. The surfaces of the boulders evolve along the rock glacier longitudinal transect. The boulders of units I and II are rounded and display quartz phenocrystals, a rugged surface, millimetric weathered crust and about 80% lichen cover (Figure 2c). On the other hand, boulders of the units IV and V are more angular, with only about 10 to 30% of lichen cover and less obvious surface weathering features (Figure 2d).

4.2 Image correlation

As described in section 3.2, we used ~~pairs~~a pair of ~~orthorectified images~~orthomosaics to reconstruct surface displacement of the rock~~-~~ glacier system. ~~After testing all the possible combinations between the four orthorectified images (1952, 1960, 1989 and 2018), the 1960-2018 pair was chosen for being the~~ The 1960-2018 pair is the most adapted to reconstruct the activity of the rock~~-~~ glacier system over decadal timescales. As the aim of this study is to compare modern to Holocene rock~~-~~ glacier activity, we focus on the integrated displacement over the longest and best-quality time series ~~(1960-2018)~~available, instead of focusing on shorter-scale variations in surface displacement over modern timescales (e.g., ~~Cusicanqui et al., 2021). The 1960-2018 correlation gives the most extended spatial coverage and lead to the best image correlation results with respect to the difference in shading, snow cover and quality between the two rectified images. The results of the time series 1952-1960, 1960-1989 and 1989-2018 can be found in the supplementary material (Fig. A2).~~

Cusicanqui et al., 2021). Figures 3, 4 and ~~4~~5 present the results obtained using the IMCORR feature-tracking module. The surface displacement of the control ~~area~~areas (dashed outlined area in ~~Fig.~~Figures 3 and A1) within stable terrain shows ~~an averaged~~a median displacement of ~~1.55~~0.79 ±0.~~92~~43 m~~, which we use~~ (Figures 4g, A2 and Table A3). This value represents the accumulation of error from the orthomosaic production and the image correlation procedure. The quality of the orthomosaic production can be assessed using the statistics on the GCPs showing a median absolute error of 0.57 ±0.34 m (Table A1) and the manual control points presenting a median mismatch distance between the two orthomosaics of about 1.04 ±0.45 m (Figure 4h and Table A2). This last value, being the highest of the three error estimations, is used hereafter as a threshold value to control the confidence level of our ~~image-correlation protocol. This threshold value corresponds to failed correlation in between pixel group and does not correspond to real surface displacement.~~remote sensing analysis, and should be considered as the detection limit. Consequently, all rock~~-~~ glacier areas showing surface displacement lower than 1.~~55~~04 m ~~should be~~are consequently considered ~~stable~~as below the detection level (dashed area in ~~Figs. 4a-b).~~ Figure 5).

Surface displacements calculated over the entire rock~~-~~ glacier system for the last 58 years (i.e., between 1960 and 2018) show a maximum value of ~~16.9~~20.4 m, with a median displacement of 1.~~7~~3 m and a standard deviation of ~~4.~~2.0 m over the ~~total~~entire rock~~-~~ glacier area~~.~~ (Figures 3, 4f and Table A3). Note that those estimates integrate displacements over 58 years, and do not allow us to assess whether the displacements have been steady or not. The spatial distribution (~~Fig.~~Figure 3) and the longitudinal transect (~~Fig. 4a~~Figure 5a, location by red line in ~~Fig.~~Figure 3) show that significant surface displacements are concentrated in the upper part of the rock~~-~~ glacier system. Indeed, units ~~I~~IV and ~~II~~V show median surface displacements over the 1960-2018 period of 8.~~1 ±4.7~~5 ±2.9 m and 8.3 ±4~~ ±3.0~~.9 m, respectively (values calculated for all the values inside each unit~~, Table 5).~~ outline; Figures 3, 4d-e and Tables 4, A3). This agrees with our classification as “active” from geomorphological observations (~~Fig.~~Figure 2 and Section 4.1). ~~Unit~~The unit III presents surface displacements of ~~2.0 ±~~1.~~5~~9 ±1.4 m~~,~~ (Figures 3, 4c and Tables 5, A3), which is~~ just~~ above the detection limit. Our classification of transitional activity (Section 4.1) thus seems appropriate. Finally, units ~~IV~~I and ~~V~~II, with median displacement of 1.~~0 ±0.6 and 1.~~2 ±0.4 and 0.9 ±0.6 m, respectively, are similar within ±1σ and below the detection limit (~~Table 5, Figs.~~Figures 3, 4a-b and ~~4b~~Tables 4, A3). These parts of the rock~~-~~ glacier system can thus be considered ~~without modern motion,~~to be immobile over this period and correspond well with the relict classification determined from geomorphological observations (Section 4.1). The rock glacier becomes inactive around 945 m from the headwall, corresponding to an elevation of about 2600 m a.s.l. Also, two displacement peaks can be observed in the upper part of the rock glacier system (~~Figs.~~Figures 3 and ~~4a~~5a), one in unit ~~I~~IV and another in unit ~~II~~V, potentially indicating different debris sources for the two units.

4.3 Surface-exposure dating results

~~Figures 5 and 6, together with Tables 2-4, present the analytical results of ^{10}Be surface-exposure dating for each individual boulder sample, as well as for statistics within landforms and units. Our ^{10}Be-age results range from 1.88 ±0.14 to 13.10 ±0.51 ka for the entire dataset. The correction for snow-cover shielding ranges between 7 and 9% between samples. In view of the controversy over whether wind could remove snow from moraine/rock-glacier ridges during the Holocene period (Federici et al., 2008; Schimmelpfennig et al., 2014; Moran et al., 2016; Chenet et al. 2016), we refrain from correcting the output ^{10}Be ages for snow cover in the following discussion. This imply that the obtained ^{10}Be ages, with neither snow-cover nor surface-erosion correction, are considered as minimum estimates.~~

Figures 6 and 7, together with Tables 2-4, present the analytical results of ^{10}Be surface-exposure dating for each individual boulder sample, as well as for statistics within ridges and units. Our ^{10}Be-age results range from 13.10 ±0.51 to 1.88 ±0.14 ka for the entire dataset. The correction for snow-cover shielding ranges between 7 and 9% between samples. In view of the controversy over whether wind could remove snow from moraine/rock glacier ridges during the Holocene period (Federici et al., 2008; Schimmelpfennig et al., 2014; Moran et al., 2016; Chenet et al., 2016), we refrain from correcting the output ^{10}Be ages for snow cover in the following discussion. This implies that our reported ^{10}Be ages, with neither snow-cover nor surface-erosion correction, should be considered as minimum estimates.

Our results clearly reveal a first-order inverse correlation between ^{10}Be surface-exposure age and elevation, and a positive correlation between ^{10}Be surface-exposure age and horizontal distance from the headwall (~~Fig. 6). These correlations support the hypothesis that rock boulders originate from the headwall and are then transported downward on the surface of the rock glacier: the further from the headwall (and the lower the elevation) the boulder is, the older its ^{10}Be surface-exposure age.~~Figure 7). These correlations remain valid when we consider the ~~weighted-average~~ median values of the ^{10}Be surface-exposure ages for ~~every landform (Figs. 6c~~each unit (Figures 7c-d, Table 3) and ~~unit (Figs. 6e-f~~ridge (Figure A3, Table 4).

~~If considered in more detail,~~Visual inspection of the ^{10}Be-age dataset ~~shows~~allows the identification of two clusters: cluster 1 ~~combining the highest units I and II, and cluster 2 including~~includes the lowermost units (~~III,~~ I, II and II) whereas cluster 2 combines the highest units IV and V~~).~~. Cluster 1 ~~shows ^{10}Be ages between 1.88 ±0.14 and 4.88 ±0.29 ka; and cluster 2~~ presents ^{10}Be ages between 9.25 ±0.40 and 13.1 ±0.51 ka~~.~~ and cluster 2 shows ^{10}Be ages between 1.88 ±0.14 and 4.88 ±0.29 ka. These results agree with the geomorphological classification we proposed for these rock~~-~~ glacier units~~:~~, in which units I and II are viewed as ~~active~~relict, unit III as transitional, and units IV and V as ~~relict~~active.

To assess the reproducibility of our dating approach, we sampled 2 different boulders on 6 of the rock glacier ridges (A, D, G, I, K and L; Figures 2d, 6 and 8). The minimum and maximum horizontal distances between two replicates are about 8 and 82 m for ridges D (samples VR12 and VR13) and L (samples VR18 and VR19), respectively; a minimum elevation difference of about 2 m for ridges G (VR8 and VR9) and A (VR16 and VR17) and a maximum elevation difference of 14 m for ridge D (Figure 6 and Tables 1 and 2). Significant variability in ^{10}Be surface-exposure age occurs at the ridge scale, although it does not affect the correlations discussed above (Table 3 and Figure 7). Ridge K presents the higher age variability (99%, ^{10}Be surface-exposure ages of 1.32 ±0.21 and 4.88 ±0.29 ka for samples VR2 and VR3, respectively, Table 3 and Figure 8d). The age variability for the other ridges is correlated with elevation and anticorrelated with distance to the headwall (26%, 13%, 10%, 8% and 2% of age variability for 2 samples per ridge for ridges L, I, G, D and A, respectively, Table 3 and Figure 8). Only ridge A displays variability that is smaller than the absolute uncertainty on individual ^{10}Be surface-exposure ages and may therefore be considered non-significant. The same pattern is observable for variability at the scale of the units (Table 4 and Figure A4). Finally, samples from cluster 2 show much higher variability than samples from cluster 1.

4.4 Surface velocity

Figure 9 and Table 4 compile and illustrate the rock glacier surface velocities calculated from the ^{10}Be surface-exposure dating and from the correlation of aerial and satellite orthomosaics. The surface velocities based upon ^{10}Be surface-exposure dating range from 0.08 ±0.004 to 0.33 ±0.05 m/a with a median value of 0.13 m/a (Figure 9). When we calculate the median value for the different units, the surface velocities range from 0.09 ±0.01 to 0.18 ±0.11 m/a (Table 4).

For the remote-sensing analysis, we define a detection limit of 0.02 m/a corresponding to the median mismatch distance between the manual control point integrated over the 1960-2018 period (Figures 4h, 5 and Table A2). As the displacements of units I and II show surface velocities identical to the detection limit, we consider them immobile over the six last decades. Measurable motion occurs above 2600 m a.s.l., with velocities of 0.03 ±0.03 m/a in unit III. The upper units display higher velocities of the same order, about 0.15 ±0.05 and 0.14 ±0.08 m/a for units IV and V, respectively (Figure 9).

5 Discussion

The surface-displacement reconstructions of the rock-glacier system of the Vallon de la Route from both image correlation and ^{10}Be surface-exposure dating provide interesting and original insights on the applicability of such methodology on rock glacier landforms. It also suggests potential feedback between rock glacier activity, past climate, and geomorphological processes such as headwall erosion. Here we discuss the implications of the results obtained at the Vallon de la Route rock glacier system.

5.1 Inheritance/pre-exposure and loss/incomplete exposure

The ~~measured ^{10}Be concentrations~~evaluation of ~~rock-glacier boulders surfaces should always be interpreted with caution as multiple external processes can affect it. Surface erosion can cause a depletion of ^{10}Be concentration at the rock-boulder surface, as well as complex exposure histories (discontinuous exposure, snow/sediment covering), both of which would lead to an underestimation of the “accurate” ^{10}Be surface-exposure age (7% and 9% in the specific case for snow cover, see Section 4.3). On the other hand, inheritance (i.e., headwall pre-exposure before rock collapse on the rock glacier), will lead to overestimation of the ^{10}Be surface-exposure age.~~
~~We employ linear regression of the ^{10}Be dataset presented in (Fig. 6) to evaluate~~ the source of debris elevation and ~~estimate~~the estimation of the inheritance/pre-exposure of investigated boulders ~~(~~was performed using linear regression of the ^{10}Be dataset presented in Figure 7, as explained in Section 3.4 (Amschwand et al., 2021~~2020~~). For instance, when we calculate the intercept of cluster ~~1~~2 regression (i.e~~.~~., elevation at which the ^{10}Be surface-exposure age is null), we obtain an elevation of 2737 m a.s.l.; whereas if we include all the samples together (red and black dotted lines in ~~Fig. 6a~~Figure 7a, respectively), we obtain 2748 m a.s.l. From our geomorphological observations, the elevation at which the talus slope connects to the headwall is close to 2880 m a.s.l. (mean elevation of the foot of upper headwall), which may safely be considered the elevation at which debris ~~are~~is delivered to the rock glacier. The difference between ~~the different~~these elevations ~~mentioned above~~ could lead to the interpretation that the ^{10}Be surface-exposure ages are underestimated. ~~This can~~We argue that this discrepancy can instead be explained by the fact that our sampling strategy ~~was targeting~~targeted the biggest boulder at the surface of the rock glacier, so that the likelihood of any burial event was minimized. The sampled metric and pluri-metric boulders ~~we sampled~~ might ~~roll far~~have rolled farther from the cliff and might therefore be incorporated onto the rock glacier surface at a higher distance/lower elevation than the present-day limit between the talus and the headwall. The relationship between ^{10}Be surface-exposure age and elevation is also dependent on the relation between elevation and distance along the rock glacier (i.e., hypsometric distribution of the rock~~-~~ glacier surface) and the potential inheritance/pre-exposure effects on the measured ^{10}Be concentrations.

Formatted: Font color: Black

Linear regression between horizontal distance from the headwall and ^{10}Be surface-exposure age (Figure 7b) allows us to quantify potential inheritance/pre-exposure bias ~~(Fig. 6b).~~(e.g., Amschwand et al. 2021). By considering cluster ~~1~~2, the samples have experienced inheritance/pre-exposure of about 2.16 ka (intercept of red dashed line in ~~Fig. 6b~~Figure 7b). This assumes that (i) blocks fall at the talus/headwall contact and, (ii) the displacement rate is continuous over the temporal range of the considered ^{10}Be surface-exposure ages. Once again, this inheritance/pre-exposure estimate ~~has to~~must be put in proper geomorphic perspective, as units ~~I~~IV and ~~II~~V do not share the same headwall source (with potentially different slope aspects and thus different erosion rates~~), unit II being more to the southeast (Section 4.2).~~). When regressed individually for units ~~I~~IV and ~~II, potential~~V, the estimated inheritances are about 2.79 and 1.59 ~~and 2.79~~ ka for units ~~I~~IV and ~~II~~V, respectively. For above calculations, we only used samples from cluster ~~1~~2, being the youngest and closest to the headwall. Samples from cluster ~~2~~1, with the oldest ^{10}Be surface-exposure ages and the greatest distances from the headwall, could also involve other biases that include non-continuous displacement rate over this timescale and loss/incomplete exposure due to surface erosion or tilting and burial of the sampled surface.

~~To assess the reproducibility of our dating approach, we sampled 2 different boulders on 6 of the rock-glacier ridges (landforms B, C, E, G, J and M; Figs. 2d, 5 and 7). The minimum and maximum horizontal distances between two replicates are about 8 and 82 m for landforms J (samples VR12 and VR13) and B (samples VR12 and VR13), respectively; a minimum elevation difference of about 2 m for landforms G (VR8 and VR9) and M (VR16 and VR17) and a maximum elevation difference of 14 m for landform (J) (Fig. 5 and Tables 1 and 2). Significant variability in ^{10}Be surface-exposure age occurs at the landform/ridge scale, although it does not affect the output correlations discussed above (Table 3 and Fig. 6). Landform C presents the higher age variability (99%, ^{10}Be surface-exposure ages of 1.32 ±0.21 and 4.88 ±0.29 ka for samples VR2 and VR3, respectively, Table 3 and Fig. 7). The age variability of the other landforms is correlated with the elevation and anticorrelated with the distance to the headwall (26%, 13%, 10%, 8% and 2% of age variability for 2 samples per landform for landforms B, E, G, J and M, respectively, Table 3 and Fig. 7). Only landform M displays variability that is smaller than the absolute uncertainty on individual ^{10}Be surface-exposure ages, and may therefore be considered non-significant. The same pattern is observable for variability at the scale of the units (Table 4 and Fig. A3). Samples from cluster 1 show much higher variability than samples from cluster 2. A first interpretation is that samples that the variability is smoothed between samples during transport an exposure on the rock glacier (cluster 2).~~The variabilities of our ^{10}Be surface-exposure ages of the ridges and the units are lower at low elevation and far from the headwall (Tables 3-4 and Figures 8-A4). A first interpretation is that of the samples whose variability is smoothed between samples during transport and exposure on the rock glacier (cluster 1). We interpret this as highlighting that the events of tilting, burial and/or erosion of the sampled boulders do not strongly influence the reported ^{10}Be surface-exposure ages, and that the variability likely arises instead from differing exposure times on the headwall prior to rockfall delivery onto the rock~~-~~ glacier surface. Secondly, the importance of inheritance/pre-exposure events would have less importance for the oldest ^{10}Be surface-exposure ages than for the youngest ^{10}Be surface-exposure ages. The high variability in cluster ~~1~~2 of ^{10}Be surface-exposure ages could be explained by variation in ^{10}Be inheritance due to pre-exposure in the headwall. Using the difference in ^{10}Be concentration between replicates, we estimated an inheritance~~ considering that the ^{10}Be~~

~~concentration difference for each replicate correspond to a ^{10}Be production rate at the elevation of rock in the headwall (taken as 2997 m a.s.l. middle elevation of the cliff source). Results show~~. The calculated age differences ~~of~~are about 0.~~88~~17 ±0.01, 0.67 ±0.03, 1.06 ±0.04, 0.39 ±0.03, 2.88 ±0.47, 0.~~39 ±0.03, 1.06~~88 ±0.04~~, 0.67 ±0.03, 0.17 ±0.01~~ ka for ~~landforms B, C, E~~ridges A, D, G, ~~J~~I, K and ~~M~~L, respectively (Table 3). The median value of those results is 0.78 ±0.97 ka and can now be compared ~~to~~with the inheritance estimate of 2.16 ka derived from using linear regression between ^{10}Be surface-exposure age and distance to the headwall of cluster ~~1~~2.

~~We interpret the observed variability in ^{10}Be surface-exposure ages as representing the stochastic nature of rockfall events. This leads to both different residence times of boulders in the headwall before rock fall, and different sites of incorporation of boulders in the talus/rock glacier system. Interestingly, all sample ^{10}Be surface-exposure ages suggest low inheritance compared to other settings in the European Alps. In the Mont Blanc massif, for example, the more competent granitic spurs result in potential inheritance of >10 ka (Gallach et al. 2018; 2020) with commensurately lower rate of debris supply and lower frequency of rockfall events (see Section 5.3 for discussion about headwall erosion rates).~~

We interpret the majority of the observed variability in ^{10}Be surface-exposure ages as representing the stochastic nature of rockfall events. This leads to both different residence times of boulders in the headwall before rock fall, and different sites of incorporation of boulders in the talus/rock glacier system. Interestingly, all sample ^{10}Be surface-exposure ages suggest low inheritance compared to other settings in the European Alps. In the Mont Blanc massif, for example, the more competent granitic spurs result in potential inheritance of >10 ka (Gallach et al., 2018, 2020), with commensurately lower rate of debris supply and lower frequency of rockfall events (see Section 5.3 for discussion about headwall erosion rates).

5.2 Surface velocity comparison and reconstruction

~~Figure 8 and Table 5 compile and illustrate the rock~~ The 1960-2018 rock glacier surface velocities calculated from the ~~^{10}Be surface-exposure dating and from the~~ correlation of aerial and satellite ~~orthorectified~~ orthomosaics~~. When considering ^{10}Be surface-exposure dating, the mean surface speeds were calculated by dividing the distance to the headwall of either the individual sample or the unit (mean distance to the headwall evaluated at all pixels inside within the unit limits) by their corresponding individual or median ^{10}Be surface-exposure ages. Here we assumed that the ^{10}Be surface-exposure age represents exposure between the time of the rockfall event that delivered the block to the surface of the headwall/talus transition and its arrival at the sample site. The modern velocities from remote sensing analysis are calculated by dividing the measured displacement or the median values for each unit, by the time between the two orthorectified images, in this case 58 years (1960-2018).~~

~~The surface velocities based upon ^{10}Be surface-exposure dating range from 8.3 ±0.4 to 33.3 ±5.3 cm/a with a median value of 13.1 cm/a and a standard deviation of 6.4 cm/a (Fig. 6). When we average over the different units, the calculated surface velocities range from 8.9 ±1.1 to 17.9 ±11.3 cm/a (Table 5).~~ validate our proposed geomorphological classification for the activity of the different units (units I and II relict, unit III: transitional and units IV and V: active). This activity is occurring above 2600 m a.s.l. While no correlation between the distance from the headwall and the surface velocity is clearly visible;

the variability in surface velocity is significantly higher for units ~~I~~IV and ~~II~~V. The difference between units ~~I~~IV and ~~II~~V likely reflects their different debris- and snow-avalanche sources; they may therefore have independent age and ~~speed~~surface-velocity profiles. ~~As a consequence, this~~This could therefore lead to an overestimation of the distance to the headwall for unit ~~II~~IV (as the central line is defined with respect to ~~Unit I, Fig. 5~~unit V, Figure 6), and by consequence to an overestimation of its surface velocity.

~~For the remote-sensing analysis, we define a detection limit of 2.7 cm/a corresponding to the median speed of the control area (Figs. 3 and 4). As the displacements of units IV and V show surface velocities below the detection limit, we consider them immobile over the six last decades. Measurable motion occurs above 2600 m a.s.l., with velocities of 3.4 ±2.6 cm/a in unit III. The upper units display higher velocities of the same order, about 13.9 ±8.0 and 14.6 ±5.1 cm/a for units I and II, respectively. Once more, these observations validate our proposed geomorphological classification for the activity of the different units (units I and II: active, unit III: transitional and units IV and V: relict).~~

~~One striking observation is that active units (I and II~~The velocity of the two upper units above 2600 m a.s.l., which show surface velocity of about ~0.15 m/a between 1960 and 2018, are slower than the reconstructed surface velocity of the Laurichard rock glacier, located in the adjacent cirque 1 km north to our study site and facing north (Cusicanqui et al., 2021). In this study, the authors quantified an acceleration of the average surface velocity changing from 0.5 ±0.09 m/a for the 1952–1994 period to 1 ±0.09 m/a for the period 2013–2017 for this landform ranging from 2430 to 2630 m a.s.l. The difference of activity between the two sites could be explained by the control of insolation and mean annual temperature on the permafrost conditions, which are more favourable to the north facing slopes (Laurichard) than the southeast facing slopes (Vallon de la Route). This has been highlighted by the Permafrost Favorable Index distribution of the area (Marcer et al. 2017). Also, Marcer et al. (2021) have estimated the rock glacier kinematics over the past seven decades for the entire French Alps using aerial orthoimagery. Mean displacement rates increased from 0.3 m/a (for the period from 1948–1952 to 2001–2004) to 0.97 m/a (for the period between 2001–2004 to 2008–2009) to 1.25 m/a (from 2008–2009 to 2015–2017). Note that the values obtained in our study site are below the detection limit of this regional reconstruction (0.52 m/a for the period from 2008-2009 to 2015-2017; Marcer et al., 2021).

The velocity obtained by integrating ^{10}Be surface exposure age over the distance to the headwall, ranging from 0.08 ±0.004 to 0.33 ±0.05 m/a, are about the same order of magnitude as that obtained by Amschwand et al. (2021) using the same approach (~0.3 m/a). Comparing the surface velocity obtained with our two datasets (orthomosaics correlation and ^{10}Be surface-exposure dating), we see that active units (IV and V) share similar surface velocities ~~but these are also comparable~~ between long-term and short-term approaches (blue and red dataset on ~~Fig. 8~~Figure 9). Integration of the short-term surface velocities over the late Holocene appears to predict well the ^{10}Be surface-exposure ages of investigated rock~~-~~ glacier boulders. This suggests that the climatic and geomorphological conditions controlling the activity of the rock glacier have been stable above 2600 m a.s.l. over the last ca. 5 ka.

These observations should be put in a spatial perspective. The remote sensing analysis results in an estimate of the mean surface velocity over the entire area of the unit. On contrast, the velocity estimated from the ^{10}Be surface-exposure dating was

Formatted: Font: +Headings (Times New Roman)

Formatted: Font: +Headings (Times New Roman)

Formatted: Font: +Headings (Times New Roman)

Formatted: Font: +Headings (Times New Roman)

Formatted: Font: +Headings (Times New Roman)

Formatted: Font: +Headings (Times New Roman) calculated from samples collected at the center of the rock glacier system, where the surface velocity is likely to be the fastest regarding a transversal cross section. The median velocity of the unit will be lower than the maximum centerline speed, as lower thicknesses at the margins should slow the surface speeds. It is therefore expected that the ^{10}Be-based method would likely yield faster speeds than the remote-sensing method. Consequently, the agreement and relationship between the two datasets and the two timescales should be interpreted with caution.

5.3 ~~Rock~~History of rock glacier activity

~~In the following~~The Vallon de la Route cirque is occupied by a rock glacier system with well-defined rock glacier geomorphological attributes such as steep fronts, margins, ridges and furrows topography (Figure 1b and 2). No evidence of former occupation of the cirque by a clean ice or debris covered glacier is visible (no moraine nor polished bedrock surface). Consequently, we interpret the correlations presented in Section 4.3 between the ^{10}Be surface-exposure age and distance to the headwall to support the hypothesis that rock boulders originate from the headwall and are then transported downward on the surface of the rock glacier: the further from the headwall (and the lower the elevation) the boulder is, the older its ^{10}Be surface-exposure age.

Following this reasoning and acknowledging the ^{10}Be surface-exposure age distribution along the rock glacier, we propose a possible history for the rock~~-~~ glacier activity that includes two pulses of constant surface velocity. Figure ~~9~~10 presents schematically our interpretation~~ of the repartition~~ of the two clusters of ^{10}Be surface-exposure ages according to their distances from the headwall (~~Figs. 6b~~Figures 7b and ~~10b~~11b). During a first phase of activity, boulders fall from the headwall onto the surface of the rock glacier (~~Fig. 9a~~Figure 10a). The random distance from the headwall at which the boulder is incorporated in the rock glacier is representing the stochasticity of rockfall travel. The ^{10}Be inheritance, corresponding to the residence time of the rock in the headwall, is also stochastic. As rockfall-derived boulders are transported down-valley, both their ^{10}Be surface-exposure ages and distances from headwall increase from these initial values (red lines in ~~Fig. 9a~~Figure 10a). When the motion halts (presumably because the rock glacier thins beyond some threshold thickness), this first phase of activity ends, and boulders remain stationary while their ^{10}Be surface-exposure ages continue to increase (~~Fig. 9b).~~Figure 10b). During this phase of inactivity, we consider that neither snow nor rock avalanches are active. Finally, a new phase of activity begins at the base of the talus (red points in ~~Fig. 9c~~Figure 10c), and the new rock glacier overrides the up-valley boulders on the relict ~~forms~~rock glacier (shadow points in ~~Fig. 9c~~Figure 10c). In this conceptual model, we assume that the first phase of activity ~~transports~~transported the boulders further downstream than the second phase of activity.

We therefore argue that cluster ~~2~~1, corresponding to ^{10}Be surface-exposure ages of units I, II and III, ~~IV and V,~~ represents a first phase of activity of the rock glacier, and that cluster ~~1~~2, with units ~~I~~IV and ~~II~~V, represents a second phase of activity. To constrain both the timing and the surface velocities of these phases of activity, we numerically simulate the evolution of ^{10}Be surface-exposure ages of boulders during their movement at the surface of the rock glacier (~~Fig. 10b~~Figure 11b). To represent its stochasticity, we prescribed the inheritance (b in ~~Fig. 9~~Figure 10) with random values between 0 and 2.16 ka (as determined in Section 5.1). In the same way, the distance of incorporation of boulders on the rock glacier surface (a in ~~Fig. 9~~Figure 10) is randomly sampled between 0 and a maximum of 100 m. In this model, ~~3~~three different times ~~should~~must be prescribed. The initiation of the first phase of activity is set at 12.1 ka (t1 in ~~Fig. 10a~~Figure 11a), which is the ^{10}Be surface-exposure median age of unit ~~V~~I. The second phase of activity is set to start at 3.4 ka (t3 in ~~Fig. 10a~~Figure 11a) as this is the ^{10}Be surface-exposure median age of unit III and is still active now. Only the time at which the first phase of activity ends cannot be directly extracted from the ~~experimental~~ data (t2 in ~~Fig. 10a~~Figure 11a). Consequently, we simulate the ^{10}Be surface-exposure age structure of the rock~~-~~ glacier complex for 100 values of t2 ranging from t3 (3.4 ka) to the youngest age of cluster ~~2~~1 (i.e., 9.25 ka for sample VR8). The velocity of phase 1 is calculated using the maximum distance a block travelled at the surface of the rock glacier (1720 m) and the activity duration of phase 1 (t1-t2). The velocity of phase 2 is fixed at 0.22 m/a, a value calculated using the maximum distance a block travelled at the surface of the rock glacier during this phase (740 m) and the ~~time~~duration of activity (t3 in ~~Fig. 10a~~Figure 11a).

The 100 simulations are evaluated against the measured ^{10}Be concentrations using chi-square per degree of freedom, $\chi_v^2 = \frac{\chi^2}{v}$. The chi-squared is a weighted sum of squared deviations: $\chi^2 = \sum_i \frac{(O_i - C_i)^2}{\sigma_i^2}$ where σ is the variance on our ^{10}Be dataset, O are the observations, and C are the modeled data. The degree of freedom, $v = n - m$, equals the number of observations n minus the number of fitted parameters m (here 4: maximum inheritance, maximum distance of incorporation of a boulder on the rock glacier, initiation of phase 1: t1 and phase 2: t3). The likelihood probability function is then calculated as $\mathcal{L} = 1/\exp\left({\chi_v^2}/{2}\right)$ and normalized with its maximum ~~in order~~ to extract the median value and the standard variation (±1σ) of t2 (~~Fig. 10c~~Figure 11c). The inversion results ~~show~~suggest that the first phase of activity lasted from 12.1 to 6.26 ±1.96 (±1σ) ka, with a surface velocity of 0.29 ±0.15 (±1σ) m/a. The second phase of activity starts at 3.4 ka and has a surface velocity of 0.22 m/a (~~Fig. 10a~~Figure 11a). The ~~more~~most recent phase of activity overrides the ^{10}Be surface-exposure ages of the two upper units. We now discuss how these two phases of rock~~-~~ glacier activity can be connected to what is known about the paleo-environmental conditions in the western European Alps.

~~**5.4 Reconstruction of paleo-environmental conditions**~~

~~In the European Alps, the final Lateglacial period (i.e., Younger Dryas) led to readvance of the mountain glaciers reaching a maximum extent around 12 ka for both the eastern and western Alps (e.g., Ivy-Ochs et al., 2008; Protin et al., 2019). Directly downstream of the Vallon de la Route catchment, ^{10}Be surface-exposure ages of moraines show ages of 13.0 ±1.1 ka and 12.4 ±1.5 ka, providing evidence for two stages of glacial advance or standstill at the end of the Lateglacial period (Chenet et al., 2016). Immediately after the onset of the Alpine glacier retreat (12.2 ±1.5 ka in the same valley, Chenet et al., 2016), several advance episodes lasting ~1 ka were identified (in the Ecrins massif), before the retreat starts again at ~10.4 ka (in the Mont Blanc massif, Protin et al., 2019). Cossart et al. (2010) reported histories of glacier retreat and rock-glacier generation in the~~

~~Clarée valley (about 10 km to the east of our study site). They identified three generations of rock-glacier development during the second half of the Holocene, ranging in elevation from ~2400 to 2800 m a.s.l.~~

~~In the Vallon de la Route catchment, the first phase of rock-glacier activity appears to start around 12.1 ka from our oldest ^{10}Be surface exposure age (Unit V). We suggest that this coincides with the final glacier retreat at the end of the Lateglacial period. The upper mountain catchments and cirques then became free of glacier, allowing the headwall and scree field to feed a rock glacier with debris thickness sufficient to insulate the ice. In this case, the rock-glacier development would be considered to be geomorphically-controlled by contrast to a climatic control (Cossart et al., 2010). According to our reconstruction, the second generation of rock-glacier development occurred at about 3.4 ka. This is earlier than the estimate proposed by Bodin (2013) from the relationship between slope and velocity, with an estimated time of 1.7 ka for debris to reach the front of unit I lying at around 2740 m a.s.l.~~

5.4 Reconstruction of paleo-environmental conditions

In the European Alps, the final Lateglacial period (i.e., Egesen) led to readvance of the mountain glaciers reaching a maximum extent around 12 ka for both the eastern and western Alps (e.g., Susan Ivy-Ochs et al., 2008; Protin et al., 2019; Hofmann et al. 2019). Directly downstream of the Vallon de la Route catchment, ^{10}Be surface-exposure ages of moraines show ages of 13.0 ±1.1 ka and 12.4 ±1.5 ka, providing evidence for two stages of glacial advance or standstill at the end of the Lateglacial period (Chenet et al. 2016). In a southern valley of the Ecrins Pelvoux massif, morainic deposits at Pré de la Chaumette (downvalley from Rougnoux Valley) have been dated at 12.5 ±0.6 ka (Hofmann et al. 2019). Immediately after the onset of the Alpine glacier retreat (12.2 ±1.5 ka in the same valley, Chenet et al., 2016), several advance episodes lasting ~1 ka were identified in the Ecrins massif. Dating in the southern part of this massif has shown glacial activity during the Lateglacial that may have lasted until the Early Holocene before final glacial retreat (around 11 ka, Hofmann et al. 2019). Cossart et al. (2010) reported histories of glacier retreat and rock glacier generation in the Clarée valley (about 10 km to the east of our study site). They identified three generations of rock glacier development during the second half of the Holocene, ranging in elevation from ~2400 to 2800 m a.s.l. Recent dating of Charton et al. (2021) on two rock glaciers located ~3 km to the north of our site and at an elevation of about 2050 m a.s.l. reveals ^{10}Be surface-exposure ages of ca. 11 ka. They interpreted the ^{10}Be surface-exposure ages as marking the end of activity of the rock glacier.

In the present study, we interpret the ^{10}Be surface-exposure ages as being the sum of its residence time on the headwall cliff, the time spent traveling on the surface of the rock glacier, and the time since deactivation of the relict portion of the rock glacier for the relict units. We argue that rock boulders remain at the surface of the rock glacier while being transported down valley. This is supported by the small variability in ^{10}Be surface-exposure ages obtained from the ridge replicates far from the headwall, which implies little occurrence of tilting and burial events (c.f. Section 5.1). This is also supported by the rock boulder weathering evolution along the rock glacier, which displays more weathered surfaces far from the headwall (c.f. Section 4.1). Consequently, in the Vallon de la Route catchment, the first phase of rock glacier activity appears to start around 12.1 ka from our oldest ^{10}Be surface-exposure age (median value of the unit I). We suggest that this coincides with the final glacier retreat at the end of the Lateglacial period at the onset of the warm period marking the Younger Dryas – Holocene transition (e.g., Liu et al., 2014). The upper mountain catchments and cirques then became free of glaciers, allowing the headwall and scree field to feed a rock glacier with debris thickness sufficient to insulate the ice. In this case, the rock glacier development would be geomorphically-controlled by contrast to a climatic control (Cossart et al., 2010). As presented above, this first phase of activity would have ended around 6.26 ±1.96 (±1σ) ka. According to our reconstruction, the second generation of rock glacier development occurred starting at about 3.4 ka. This is earlier than the estimate proposed by Bodin (2013) from the relationship between slope and velocity, based upon an estimated time of 1.7 ka for debris to reach the front of the unit V lying at around 2740 m a.s.l.

Whereas lateral glacier moraines dated using ^{10}Be surface-exposure approach suggest minor but several glacier re-advances between ca. 4.25 and 0.92 ka in the main glacierized valleys of the Ecrins-Pelvoux massif ~~(Le Roy et al., 2017),~~(Le Roy et al. 2017), there is no evidence for glacial re-occupation during the Neoglacial/Little Ice Age periods in the Vallon de la Route. This specific cirque does not share upstream connection with any of the main glacierized valleys of the massif. The headwall and scree taluses were ice free and could therefore feed the rock~~-~~ glacier system with debris and snow avalanches, maintaining the rock glacier during the last 3.4 ka, ~~while~~when the Neoglacial/Little Ice Age climate was favourable for glacier/rock glacier activity.

Formatted: Indent: First line: 0 cm

~~Recent dating of Charton et al. (2021) on two rock glaciers located ~3 km to the north of our site and at an elevation of about 2050 m a.s.l. reveals ^{10}Be surface-exposure ages of ca. 11 ka. In their study, Charton et al. (2021) interpreted the ^{10}Be surface-exposure ages as marking the end of activity of the rock glacier. In the present study, we interpret the ^{10}Be surface-exposure ages of the relict units as being the sum of its residence time on the headwall cliff, the time spent traveling on the surface of the rock glacier, and the time since deactivation of the relict portion of the rock glacier. Consequently, the inspection of the age structure of our rock glacier agrees with the following interpretation. The age structure (Fig. 10b) suggests two episodes of motion (Fig. 10a). The first phase, starting around 12 ka, displays a gradient in age with rock-glacier surface velocity of about 0.45 m/a. The rock-glacier activity then declines and stops at 6.26 ±1.96 ka. By around 3.4 ka, the climate again becomes conducive to rock glacier motion at elevations above 2600 m a.s.l. and the presently active upper two units are emplaced. Again, the ^{10}Be surface-exposure ages reveal an age gradient that reflects the surface velocity of 0.18 m/a (Fig. 10a) which agrees with modern estimates.~~

Consequently, the inspection of the age structure of our rock glacier suggests two episodes of motion (Figure 11a). The first phase, starting around 12.1 ka, displays a gradient in age with rock glacier surface velocity of about 0.45 m/a. The rock glacier activity then declines and stops at 6.26 ±1.96 ka. By around 3.4 ka, the climate again becomes conducive to rock glacier motion at elevations above 2600 m a.s.l. and the presently active upper two units have been emplaced. Even if climate during the Late Holocene has fluctuated (e.g., Liu et al., 2014), the integrated velocities calculated with the ^{10}Be surface-exposure ages reveal that the surface velocity of 0.18 m/a (Figure 11a) agrees with modern estimates.

5.5 Headwall erosion and implications

The reconstruction of the rock~~-~~ glacier activity provides a way to quantify the erosion rate of the surrounding headwalls over Holocene timescales~~.~~ (e.g, Humlum 2000; Amschwand et al. 2021). Bodin (2013) has performed geophysical measurement of the rock~~-~~ glacier area and could determine a maximum thickness of the active layer of about 9 m and a maximum thickness of the ice-rich layer of about 15 m at 2630 m a.s.l. The entire area of the rock glacier is 6.745×10^5 m^2. An approximation of the total volume of debris, considering a total thickness of between 9.5 m (active layer thickness of 5 m and ice-rich layer of 4.5 m thick at 2720 m a.s.l.; ~~Bodin, 2013)~~Bodin, 2013) and 24 m (combining maximum of active layer thickness of 9 m and ice-rich layer of 15 m thick at 2630 m a.s.l.; ~~Bodin, 2013),~~Bodin, 2013), gives respectively 3.37×10^6 and 13.49×10^6 m^3. Regarding the low surface velocity estimated between ~~1968~~1960 and 2018, between 0.14 and 0.03 m/a over 42% of the total area (units ~~I, II~~III, IV and ~~III~~V) and no movement of the other 58% of the total rock~~-~~ glacier area (units ~~IV~~I and ~~V~~II), we can assume a negligible ice concentration over the ~~all~~full volume of the rock~~-~~ glacier system. ~~We then integrate~~Taking this volume of debris over 12.1 ka (the median ^{10}Be surface-exposure age of unit ~~V), we consider~~I), and considering that all boulders are derived from bedrock exposed above the rock glacier system (about 5.351×10^5 m^2), ~~and~~we can~~ thus~~ calculate a mean rate of erosion of the headwalls of between 1.0 and 2.5 mm/a. These results agree with estimates of erosion rate (~1.2-4.1 mm/a) from the granodioritic headwall of Bleis Marscha rock glacier in the eastern part of the Swiss Alps ~~(Amschwand et al., 2021).~~(Amschwand et al. 2021a). The catchment-wide denudation rate of the Ecrins-Pelvoux massif has been estimated to range from around 0.3 to 1.1 mm/a on millennial timescales using ^{10}Be concentrations in stream sediment (Delunel et al., 2010), suggesting that frost-cracking processes strongly control the post-glacial topographic evolution of mid-latitude mountain belts. The high erosion rates estimated in our study highlight that the steep rock walls that serve as the sources for debris on the rock glacier are retreating rapidly. This may be aided by the downstream conveyance of boulders/debris by the rock glaciers that prevent the headwalls from burying themselves in their own debris. This system therefore promotes the maintenance of high rockwall erosion rates~~ and~~, the development of cirques~~.~~, and the possibility of distinctly asymmetric mountain ridges where the local climate is more conducive to rock glacier development on one side of a ridge than the other (Gilbert, 1904).

Conclusion

In this study, we quantitatively constrain the surface displacement field of an alpine rock~~-~~ glacier system over Holocene and modern timescales, by using both remote-sensing and geochronological datasets. The ^{10}Be surface-exposure dating of individual boulders ~~sampled following~~along the main center line of the rock glacier ~~reveal~~reveals ages from ~~1.8 to~~ 13.1 to 1.8 ka, corresponding to elevations of ~~2751 and~~ 2535 and 2751 m a.s.l., respectively. Our first-order observation shows an inverse correlation between ^{10}Be surface-exposure age and elevation, as well as a positive correlation between ^{10}Be surface-exposure age and distance from the headwall. This confirms the simple conceptual model in which rock debris falls from the headwall and remains ~~on~~at the surface as they are transported down valley by the rock glacier. Comparison of replicates from the transverse ridges along the rock glacier ~~show~~shows that loss/incomplete exposure due to surface erosion, burial or tilting of the boulders is negligible. These replicates also show that ^{10}Be concentrations of boulders close to the headwall can vary, ~~constraining any~~ which in turn provides constraint on the inheritance/pre-exposure ~~effect.~~of rock boulders. We estimate the possible maximum inheritance of 2.16 ka in our ~~studied~~study area, corresponding to the residence time of boulders in the headwall.

~~The inverstigation~~Comparison of orthoimages from both aerial (1960) and satellite (2018) surveys shows that the rock~~-~~ glacier system is composed of two uppermost active units with surface velocity of about 0.14 m/a at elevations from 2867 and 2626 m a.s.l., and a transitional unit with surface velocity of about 0.03 m/a at elevations between 2685 and 2556 m a.s.l. Analysis of a stable area outboard of the rock~~-~~ glacier system constrains the detection limit to be 0.02 m/a. Reported values of less than this detection threshold ~~implies~~imply that the downstream part of the rock glacier, below 2600 m a.s.l. is presently immobile, confirming our geomorphic analysis ~~or~~of the feature as relict. The comparison of the surface ~~velocity~~velocities estimated using the ^{10}Be surface-exposure dating relative to distance to the headwall, and from the surface displacement integrated over the 1960-2018 period between the orthoimage surveys, shows that late Holocene and modern velocities are comparable on the active units of the rock~~-~~ glacier system.

~~Our~~Comparison of these results ~~suggest~~for the entire rock glacier allows us to propose an activity ~~of~~history for the Vallon de la Route rock glacier ~~consisting~~that consists of two main phases of surface displacement. The first episode lasted between about 12.1 ka and 6.26 ±1.96 ka, with onset around the end of the Younger Dryas cooling event, when the cirques became ice free, allowing the headwall and scree field to feed the rock glacier with debris, with insulation of the ice beneath. After a period of quiescence, the second phase of activity started around 3.4 ka and continues ~~to~~towards the present, possibly attributed to the more favourable climate of the Neoglacial/Little Ice Age periods. Finally, we use the surface ~~velocity~~velocities obtained using ^{10}Be surface-exposure dating to reconstruct the erosion rate of the headwalls. The ~~output~~suggested erosion rates are between 1.0 and 2.5 mm/a. These are higher than catchment-wide denudation rates estimated over millennial timescales over the entire Ecrins-Pelvoux massif, suggesting that the rock~~-~~ glacier system promotes the maintenance of high rock~~-~~ wall erosion (back-wearing) rates and the development of cirques. To go further in reconstructing the paleo-environmental conditions of this specific region, physically~~-~~ based numerical modeling of rock glacier evolution (e.g., Anderson et al., 2018) should be applied using the existing topography, the spatial patterns of ^{10}Be surface-exposure ages and the modern surface ~~velocity~~velocities as modeling targets.

Author contribution

BL and RSA designed the study. BL and XB chose the study site and collected the samples in the field. PGV and JC supervised the TCN lab work of BL and provides the financial support for the TCN dating. BL and DC performed the remote-sensing analysis. BL and RSA wrote the numerical modelling experiments. All authors contributed to the writing of the manuscript.

Competing interest

The authors declare that they have no conflict of interest.

Acknowledgements

This study has been funded through the Mobility followship P2LAP2_191400 of the Swiss National Science Foundation. The authors acknowledge the Joseph Fourier alpine station for providing logistical and hosting support during the field campaign and the ASTER team (K. Keddadouche, G. Aumaitre, R. Braucher and V. Godard) for AMS analyses. The TRB team (ISTerre) is acknowledged for providing financial support for TCN dating. P.G.V. acknowledges funding from the Swiss National Science Foundation SNSF (Grant 639 PP00P2_170559) and the French ANR-PIA programme (ANR-18- MPGA-0006).

References

~~Amschwand, D., Ivy-Ochs, S., Frehner, M., Steinemann, O., Christl, M., & Vockenhuber, C. (2021). Deciphering the evolution of the Bleis Marscha rock glacier (Val d'Err, eastern Switzerland) with cosmogenic nuclide exposure dating, aerial image correlation, and finite element modeling. *Cryosphere*, *15*(4), 2057–2081. https://doi.org/10.5194/tc-15-2057-2021~~

~~Anderson, R. S., Anderson, L. S., Armstrong, W. H., Rossi, M. W., & Crump, S. E. (2018). Glaciation of alpine valleys: The glacier-debris-covered glacier-rock glacier continuum. *Geomorphology*, *311*, 127–142. https://doi.org/10.1016/j.geomorph.2018.03.015~~

~~Andrés, N., Gómez-Ortiz, A., Fernández-Fernández, J. M., Tanarro, L. M., Salvador-Franch, F., Oliva, M., & Palacios, D. (2018). Timing of deglaciation and rock glacier origin in the southeastern Pyrenees: a review and new data. *Boreas*, *47*(4), 1050–1071. https://doi.org/10.1111/bor.12324~~

~~Balco, G., Stone, J. O., Lifton, N. A., & Dunai, T. J. (2008). A complete and easily accessible means of calculating surface exposure ages or erosion rates from ^{10}Be and ^{26}Al measurements. *Quaternary Geochronology*, *3*(3), 174–195. https://doi.org/10.1016/j.quageo.2007.12.001~~

~~Barboux, C., Delaloye, R., & Lambiel, C. (2014). Inventorying slope movements in an Alpine environment using DInSAR. *Earth Surface Processes and Landforms*, *39*(15), 2087–2099. https://doi.org/10.1002/esp.3603~~

~~Barsch, D. (1977). Nature And Importance Of Mass-Wasting By Rock Glaciers In Alpine Permafrost Environments. *Earth Surf Process*, *2*(2–3), 231–245. https://doi.org/10.1002/esp.3290020213~~

~~Berthling, I. (2011a). Beyond confusion: Rock glaciers as cryo-conditioned landforms. *Geomorphology*, *131*(3–4), 98–106. https://doi.org/10.1016/j.geomorph.2011.05.002~~

~~Berthling, I. (2011b). Beyond confusion: Rock glaciers as cryo-conditioned landforms. *Geomorphology*, *131*(3–4), 98–106. https://doi.org/10.1016/j.geomorph.2011.05.002~~

~~Blöthe, J. H., Halla, C., Schwalbe, E., Bottegal, E., Trombotto Liaudat, D., & Schrott, L. (2021). Surface velocity fields of active rock glaciers and ice-debris complexes in the Central Andes of Argentina. *Earth Surface Processes and Landforms*, *46*(2), 504–522. https://doi.org/10.1002/esp.5042~~

~~Bodin, X. (2013). Present status and development of rock glacier complexes in south-faced valleys (45°N, French Alps). *Geografia Fisica e Dinamica Quaternaria*, *36*(1), 27–38. https://doi.org/10.4461/GFDQ.2013.36.2~~

~~Bodin, X., Thibert, E., Sanchez, O., Rabatel, A., & Jaillet, S. (2018). Multi-Annual kinematics of an active rock glacier quantified from very high-resolution DEMs: An application-case in the French Alps. *Remote Sensing*, *10*(4). https://doi.org/10.3390/rs10040547~~

~~Böhlert, R., Compeer, M., Egli, M., Brandová, D., Maisch, M., Kubik, P. W., & Haeberli, W. (2011). A combination of relative-numerical dating methods indicates two high alpine rock glacier activity phases after the glacier advance of the younger dryas. *Open Geography Journal*, *4*, 115–130. https://doi.org/10.2174/1874923201104010115~~

~~Braucher, R., Bourlès, D., Merchel, S., … J. R.-N. I. and, & 2013, undefined. (n.d.). Determination of muon attenuation lengths in depth profiles from in situ produced cosmogenic nuclides. *Elsevier*. Retrieved December 13, 2021, from https://www.sciencedirect.com/science/article/pii/S0168583X12002911~~

~~Brown, E. T., Edmond, J. M., Raisbeck, G. M., Yiou, F., Kurz, M. D., & Brook, E. J. (1991). Examination of surface exposure ages of Antarctic moraines using in situ produced ^{10}Be and ^{26}Al. *Geochimica et Cosmochimica Acta*, *55*(8), 2269–2283. https://doi.org/10.1016/0016-7037(91)90103-C~~

~~Charton, J., Verfaillie, D., Jomelli, V., & Francou, B. (2021). Early Holocene rock glacier stabilisation at col du Lautaret (French Alps): Palaeoclimatic implications. *Geomorphology*, *394*. https://doi.org/10.1016/j.geomorph.2021.107962~~

~~Chenet, M., Brunstein, D., Jomelli, V., Roussel, E., Rinterknecht, V., Mokadem, F., Biette, M., Robert, V., & Léanni, L. (2016). ^{10}Be cosmic-ray exposure dating of moraines and rock avalanches in the Upper Romanche valley (French Alps): Evidence of two glacial advances during the Late Glacial/Holocene transition. *Quaternary Science Reviews*, *148*, 209–221. https://doi.org/10.1016/j.quascirev.2016.07.025~~

~~Claude, A., Ivy-Ochs, S., Kober, F., Antognini, M., Salcher, B., & Kubik, P. W. (2014). The Chironico landslide (Valle Leventina, southern Swiss Alps): age and evolution. *Swiss Journal of Geosciences*, *107*(2–3), 273–291. https://doi.org/10.1007/s00015-014-0170-z~~

~~Cossart, E., Fort, M., Bourles, D., Carcaillet, J., Perrier, R., Siame, L., & Braucher, R. (2010a). Climatic significance of glacier~~

~~retreat and rockglaciers re-assessed in the light of cosmogenic dating and weathering rind thickness in Clarée valley (Briançonnais, French Alps). *Catena*, *80*(3), 204–219. https://doi.org/10.1016/j.catena.2009.11.007~~

~~Cossart, E., Fort, M., Bourles, D., Carcaillet, J., Perrier, R., Siame, L., & Braucher, R. (2010b). Climatic significance of glacier retreat and rockglaciers re-assessed in the light of cosmogenic dating and weathering rind thickness in Clarée valley (Briançonnais, French Alps). *Catena*, *80*(3), 204–219. https://doi.org/10.1016/j.catena.2009.11.007~~

~~Coûteaux, M., & Edouard, J.-L. (1987). La déglaciation du site du lac des Bèches (Massif des Ecrins). Etude pollenanalytique et glacio-morphologique. *Revue de Géographie Alpine*, *75*(1), 63–77. https://doi.org/10.3406/rga.1987.2666~~

~~Cremonese, E., Gruber, S., Phillips, M., Pogliotti, P., Boeckli, L., Noetzli, J., Suter, C., Bodin, X., Crepaz, A., Kellerer-Pirklbauer, A., Lang, K., Letey, S., Mair, V., Morra Di Cella, U., Ravanel, L., Scapozza, C., Seppi, R., & Zischg, A. (2011). Brief communication: "An inventory of permafrost evidence for the European Alps." *Cryosphere*, *5*(3), 651–657. https://doi.org/10.5194/tc-5-651-2011~~

~~Cusicanqui, D., Rabatel, A., & Vincent, C. (2021). *Interpretation of Volume and Flux Changes of the Laurichard Rock Glacier Between 1952 and 2019 , French Alps Journal of Geophysical Research : Earth Surface*. https://doi.org/10.1029/2021JF006161~~

~~Cusicanqui, D., Rabatel, A., Vincent, C., Bodin, X., Thibert, E., & Francou, B. (2021a). Interpretation of Volume and Flux Changes of the Laurichard Rock Glacier Between 1952 and 2019, French Alps. *Journal of Geophysical Research: Earth Surface*, *126*(9), e2021JF006161. https://doi.org/10.1029/2021JF006161~~

~~Cusicanqui, D., Rabatel, A., Vincent, C., Bodin, X., Thibert, E., & Francou, B. (2021b). Interpretation of Volume and Flux Changes of the Laurichard Rock Glacier Between 1952 and 2019, French Alps. *Journal of Geophysical Research: Earth Surface*, *126*(9), e2021JF006161. https://doi.org/10.1029/2021JF006161~~

~~Dall'Asta, E., Forlani, G., Roncella, R., Santise, M., Diotri, F., & Morra di Cella, U. (2017). Unmanned Aerial Systems and DSM matching for rock glacier monitoring. *ISPRS Journal of Photogrammetry and Remote Sensing*, *127*, 102–114. https://doi.org/10.1016/j.isprsjprs.2016.10.003~~

~~Delaloye, R., & Echelard, T. (2020). IPA Action Group Rock glacier inventories and kinematics (version 4.1). *International Permafrost Association*, 1–13.~~

~~Delaloye, R., Lambiel, C., & Gärtner-Roer, I. (2010). Aperçu de la cinématique des glaciers rocheux dans les alpes suisses. Rythme saisonnier, variations interannuelles et tendance pluri-décennale. *Geographica Helvetica*, *65*(2), 135–145. https://doi.org/10.5194/gh-65-135-2010~~

~~Delunel, R. (2010). Evolution géomorphologique du massif des Ecrins-Pelvoux depuis le Dernier Maximum Glaciaire – Apports des nucléides cosmogéniques produits in-situ. *Ecole Doctorale Terre Univers Environnement Laboratoire de*~~

~~*Géodynamique Des Chaînes Alpines, Ph. D. The*, 236.~~

~~Delunel, Romain, Bourlès, D. L., van der Beek, P. A., Schlunegger, F., Leya, I., Masarik, J., & Paquet, E. (2014). Snow shielding factors for cosmogenic nuclide dating inferred from long-term neutron detector monitoring. *Quaternary Geochronology*, *24*, 16–26. https://doi.org/10.1016/j.quageo.2014.07.003~~

~~Delunel, Romain, van der Beek, P. A., Carcaillet, J., Bourlès, D. L., & Valla, P. G. (2010). Frost-cracking control on catchment denudation rates: Insights from in situ produced ^{10}Be concentrations in stream sediments (Ecrins-Pelvoux massif, French Western Alps). *Earth and Planetary Science Letters*, *293*(1–2), 72–83. https://doi.org/10.1016/j.epsl.2010.02.020~~

~~Eriksen, H., Rouyet, L., Lauknes, T. R., Berthling, I., Isaksen, K., Hindberg, H., Larsen, Y., & Corner, G. D. (2018). Recent Acceleration of a Rock Glacier Complex, Ádjet, Norway, Documented by 62 Years of Remote Sensing Observations. *Geophysical Research Letters*, *45*(16), 8314–8323. https://doi.org/10.1029/2018GL077605~~

~~Federici, P. R., Granger, D. E., Pappalardo, M., Ribolino, A., Spagnolo, M., & Cyr, A. J. (2008). Exposure age dating and Equilibrium Line Altitude reconstruction of an Egesen moraine in the Maritime Alps, Italy. *Boreas*, *37*(2), 245–253. https://doi.org/10.1111/j.1502-3885.2007.00018.x~~

~~Fernández-Fernández, J. M., Palacios, D., Andrés, N., Schimmelpfennig, I., Tanarro, L. M., Brynjólfsson, S., López-Acevedo, F. J., Sæmundsson, Þ., & Team, A. S. T. E. R. (2020). Constraints on the timing of debris-covered and rock glaciers: An exploratory case study in the Hólar area, northern Iceland. *Geomorphology*, *361*, 107196. https://doi.org/10.1016/j.geomorph.2020.107196~~

~~Francou, B. (1982). Chutes de pierres et éboulisation dans les parois de l'étage périglaciaire. *Revue de Géographie Alpine*, *70*(3), 279–300. https://doi.org/10.3406/rga.1982.2508~~

~~Francou, B., & Reynaud, L. (1992). 10 year surficial velocities on a rock glacier (Laurichard, French Alps). *Permafrost and Periglacial Processes*, *3*(3), 209–213. https://doi.org/10.1002/ppp.3430030306~~

~~Frehner, M., Ling, A. H. M., & Gärtner-Roer, I. (2015). Furrow-and-ridge morphology on rockglaciers explained by gravity-driven buckle folding: A case study from the murtèl rockglacier (Switzerland). *Permafrost and Periglacial Processes*, *26*(1), 57–66. https://doi.org/10.1002/ppp.1831~~

~~Fuchs, M. C., Böhlert, R., Krbetschek, M., Preusser, F., & Egli, M. (2013). Exploring the potential of luminescence methods for dating Alpine rock glaciers. *Quaternary Geochronology*, *18*, 17–33. https://doi.org/10.1016/j.quageo.2013.07.001~~

~~Gallach, X., Carcaillet, J., Ravanel, L., Deline, P., Ogier, C., Rossi, M., Malet, E., & Garcia-Sellés, D. (2020). Climatic and structural controls on Late-glacial and Holocene rockfall occurrence in high-elevated rock walls of the Mont Blanc massif (Western Alps). *Earth Surface Processes and Landforms*, *45*(13), 3071–3091. https://doi.org/10.1002/esp.4952~~

~~Gallach, X., Ravanel, L., Egli, M., Brandova, D., Schaepman, M., Christl, M., Gruber, S., Deline, P., Carcaillet, J., & Pallandre, F. (2018). Timing of rockfalls in the Mont Blanc massif (Western Alps): evidence from surface exposure dating with cosmogenic ^{10}Be. *Landslides, 15*(10), 1991–2000. https://doi.org/10.1007/s10346-018-0999-8~~

~~Gardent, M., Rabatel, A., Dedieu, J. P., & Deline, P. (2014). Multitemporal glacier inventory of the French Alps from the late 1960s to the late 2000s. *Global and Planetary Change*, *120*, 24–37. https://doi.org/10.1016/j.gloplacha.2014.05.004~~

~~Giardino, J. R., & Vitek, J. D. (1988). The significance of rock glaciers in the glacial-periglacial landscape continuum. *Journal of Quaternary Science*, *3*(1), 97–103. https://doi.org/10.1002/jqs.3390030111~~

~~Gosse, J. C., & Phillips, F. M. (2001). Terrestrial in situ cosmogenic nuclides: Theory and application. *Quaternary Science Reviews*, *20*(14), 1475–1560. https://doi.org/10.1016/S0277-3791(00)00171-2~~

~~Haeberli, W. (2013). Mountain permafrost - research frontiers and a special long-term challenge. *Cold Regions Science and Technology*, *96*, 71–76. https://doi.org/10.1016/j.coldregions.2013.02.004~~

~~Haeberli, W., Hallet, B., Arenson, L., Elconin, R., Humlum, O., Kääb, A., Kaufmann, V., Ladanyi, B., Matsuoka, N., Springman, S., & Mühll, D. V. (2006). Permafrost creep and rock glacier dynamics. *Permafrost and Periglacial Processes*, *17*(3), 189–214. https://doi.org/10.1002/ppp.561~~

~~Hippolyte, J. C., Bourlès, D., Braucher, R., Carcaillet, J., Léanni, L., Arnold, M., & Aumaitre, G. (2009). Cosmogenic ^{10}Be dating of a sackung and its faulted rock glaciers, in the Alps of Savoy (France). *Geomorphology*, *108*(3–4), 312–320. https://doi.org/10.1016/j.geomorph.2009.02.024~~

~~Hormes, A., Ivy-Ochs, S., Kubik, P. W., Ferreli, L., & Maria Michetti, A. (2008). ^{10}Be exposure ages of a rock avalanche and a late glacial moraine in Alta Valtellina, Italian Alps. *Quaternary International*, *190*(1), 136–145. https://doi.org/10.1016/j.quaint.2007.06.036~~

~~Ikeda, A., Matsuoka, N., & Kääb, A. (2008). Fast deformation of perennially frozen debris in a warm rock glacier in the Swiss Alps: An effect of liquid water. *Journal of Geophysical Research: Earth Surface*, *113*(1). https://doi.org/10.1029/2007JF000859~~

~~Ivy-Ochs, S. (2015). Variaciones glaciares en los Alphs europoes al final de la última glaciación. *Cuadernos de Investigacion Geografica*, *41*(2), 295–315. https://doi.org/10.18172/cig.2750~~

~~Ivy-Ochs, Susan, Kerschner, H., Kubik, P. W., & Schlüchter, C. (2006). Glacier response in the European Alps to Heinrich Event 1 cooling: The Gschnitz stadial. In *Journal of Quaternary Science* (Vol. 21, Issue 2, pp. 115–130). https://doi.org/10.1002/jqs.955~~

~~Ivy-Ochs, Susan, Kerschner, H., Reuther, A., Preusser, F., Heine, K., Maisch, M., Kubik, P. W., & Schlüchter, C. (2008). Chronology of the last glacial cycle in the European Alps. *Journal of Quaternary Science*, *23*(6–7), 559–573. https://doi.org/10.1002/jqs.1202~~

~~Jones, D. B., Harrison, S., Anderson, K., & Whalley, W. B. (2019). Rock glaciers and mountain hydrology: A review. *Earth-Science Reviews*, *193*(March), 66–90. https://doi.org/10.1016/j.earscirev.2019.04.001~~

~~Kaab, A., Haeberli, W., & Hilmar Gudmundsson, G. (1997). Analysing the creep of mountain permafrost using high precision aerial photogrammetry: 25 years of monitoring Gruben rock glacier, Swiss Alps. *Permafrost and Periglacial Processes*, *8*(4), 409–426. https://doi.org/10.1002/(SICI)1099-1530(199710/12)8:4<409::AID-PPP267>3.0.CO;2-C~~

~~Kellerer-Pirklbauer, A. (2017). Potential weathering by freeze-thaw action in alpine rocks in the European Alps during a nine year monitoring period. *Geomorphology*, *296*, 113–131. https://doi.org/10.1016/j.geomorph.2017.08.020~~

~~Kellerer-Pirklbauer, A., & Rieckh, M. (2016). Monitoring nourishment processes in the rooting zone of an active rock glacier in an alpine environment. *Zeitschrift Fur Geomorphologie*, *60*, 99–121. https://doi.org/10.1127/zfg_suppl/2016/00245~~

~~Kelly, M. A., Buoncristiani, J. F., & Schlüchter, C. (2004). A reconstruction of the last glacial maximum (LGM) ice-surface geometry in the western Swiss Alps and contiguous Alpine regions in Italy and France. *Eclogae Geologicae Helvetiae*, *97*(1), 57–75. https://doi.org/10.1007/s00015-004-1109-6~~

~~Kenner, R., Phillips, M., Limpach, P., Beutel, J., & Hiller, M. (2018). Monitoring mass movements using georeferenced time-lapse photography: Ritigraben rock glacier, western Swiss Alps. *Cold Regions Science and Technology*, *145*, 127–134. https://doi.org/10.1016/j.coldregions.2017.10.018~~

~~Kohl, C. P., & Nishiizumi, K. (1992). Chemical isolation of quartz for measurement of in-situ -produced cosmogenic nuclides. In *Geochimica et Cosmochimica Acta* (Vol. 56, Issue 9, pp. 3583–3587). Pergamon. https://doi.org/10.1016/0016-7037(92)90401-4~~

~~Krainer, K., Bressan, D., Dietre, B., Haas, J. N., Hajdas, I., Lang, K., Mair, V., Nickus, U., Reidl, D., Thies, H., & Tonidandel, D. (2015). A 10,300-year-old permafrost core from the active rock glacier Lazaun, southern Ötztal Alps (South Tyrol, northern Italy). *Quaternary Research (United States)*, *83*(2), 324–335. https://doi.org/10.1016/j.yqres.2014.12.005~~

~~Le Roy, M., Deline, P., Carcaillet, J., Schimmelpfennig, I., & Ermini, M. (2017). ^{10}Be exposure dating of the timing of Neoglacial glacier advances in the Ecrins-Pelvoux massif, southern French Alps. *Quaternary Science Reviews*, *178*(December), 118–138. https://doi.org/10.1016/j.quascirev.2017.10.010~~

~~Lifton, N., Sato, T., & Dunai, T. J. (2014). Scaling in situ cosmogenic nuclide production rates using analytical approximations to atmospheric cosmic-ray fluxes. *Earth and Planetary Science Letters*, *386*, 149–160. https://doi.org/10.1016/j.epsl.2013.10.052~~

~~Liu, L., Millar, C. I., Westfall, R. D., & Zebker, H. A. (2013). Surface motion of active rock glaciers in the Sierra Nevada, California, USA: Inventory and a case study using InSAR. *Cryosphere*, *7*(4), 1109–1119. https://doi.org/10.5194/tc-7-1109-2013~~

~~Marcer, M., Cicoira, A., Cusicanqui, D., Bodin, X., Echelard, T., Obregon, R., & Schoeneich, P. (2021). Rock glaciers throughout the French Alps accelerated and destabilised since 1990 as air temperatures increased. *Communications Earth & Environment*, *2*(1), 1–11. https://doi.org/10.1038/s43247-021-00150-6~~

~~Martin, L. C. P., Blard, P. H., Balco, G., Lavé, J., Delunel, R., Lifton, N., & Laurent, V. (2017). The CREp program and the ICE-D production rate calibration database: A fully parameterizable and updated online tool to compute cosmic-ray exposure ages. *Quaternary Geochronology*, *38*, 25–49. https://doi.org/10.1016/j.quageo.2016.11.006~~

~~Matthews, J. A., & Wilson, P. (2015). Improved Schmidt-hammer exposure ages for active and relict pronival ramparts in southern Norway, and their palaeoenvironmental implications. *Geomorphology*, *246*, 7–21. https://doi.org/10.1016/j.geomorph.2015.06.002~~

~~Merchel, S., & Herpers, U. (1999). An update on radiochemical separation techniques for the determination of long-lived radionuclides via accelerator mass spectrometry. *Radiochimica Acta*, *84*(4), 215–219. https://doi.org/10.1524/ract.1999.84.4.215~~

~~Micheletti, N., Tonini, M., & Lane, S. N. (2017). Geomorphological activity at a rock glacier front detected with a 3D density-based clustering algorithm. *Geomorphology*, *278*, 287–297. https://doi.org/10.1016/j.geomorph.2016.11.016~~

~~Monegato, G., Scardia, G., Hajdas, I., Rizzini, F., & Piccin, A. (2017). The Alpine LGM in the boreal ice-sheets game. *Scientific Reports*, *7*(1), 1–8. https://doi.org/10.1038/s41598-017-02148-7~~

~~Moran, A. P., Ivy-Ochs, S., Schuh, M., Christl, M., & Kerschner, H. (2016). Evidence of central Alpine glacier advances during the Younger Dryas–early Holocene transition period. *Boreas*, *45*(3), 398–410. https://doi.org/10.1111/bor.12170~~

~~Necsoiu, M., Onaca, A., Wigginton, S., & Urdea, P. (2016). Rock glacier dynamics in Southern Carpathian Mountains from high-resolution optical and multi-temporal SAR satellite imagery. *Remote Sensing of Environment*, *177*, 21–36. https://doi.org/10.1016/j.rse.2016.02.025~~

~~Nuth, C., & Kääb. (2011). Co-registration and bias corrections of satellite elevation data sets for quantifying glacier thickness change. *Cryosphere*, *5*(1), 271–290. https://doi.org/10.5194/tc-5-271-2011~~

~~Paasche, Ø., Dahl, S. O., Løvlie, R., Bakke, J., & Nesje, A. (2007). Rockglacier activity during the Last Glacial–Interglacial transition and Holocene spring snowmelting. *Quaternary Science Reviews*, *26*(5–6), 793–807. https://doi.org/10.1016/j.quascirev.2006.11.017~~

~~Palacios, D., Oliva, M., Gómez-Ortiz, A., Andrés, N., Fernández-Fernández, J. M., Schimmelpfennig, I., Léanni, L., & Team, A. S. T. E. R. (2020). Climate sensitivity and geomorphological response of cirque glaciers from the late glacial to the Holocene, Sierra Nevada, Spain. *Quaternary Science Reviews*, *248*. https://doi.org/10.1016/j.quascirev.2020.106617~~

~~Pavón-Carrasco, F. J., Osete, M. L., Torta, J. M., & De Santis, A. (2014). A geomagnetic field model for the Holocene based on archaeomagnetic and lava flow data. *Earth and Planetary Science Letters*, *388*, 98–109. https://doi.org/10.1016/j.epsl.2013.11.046~~

~~Protin, M., Schimmelpfennig, I., Mugnier, J. L., Ravanel, L., Le Roy, M., Deline, P., Favier, V., Buoncristiani, J. F., Aumaître, G., Bourlès, D. L., & Keddadouche, K. (2019). Climatic reconstruction for the Younger Dryas/Early Holocene transition and the Little Ice Age based on paleo-extents of Argentière glacier (French Alps). *Quaternary Science Reviews*, *221*. https://doi.org/10.1016/j.quascirev.2019.105863~~

~~RGIK. (2020). *Rock glacier inventory using InSAR (kinematic approach), Practical Guidelines v3.0.2*. https://bigweb.unifr.ch/Science/Geosciences/Geomorphology/Pub/Website/CCI/CurrentVersion/Current_InSAR-based_Guidelines.pdf~~

~~Robson, B. A., Bolch, T., MacDonell, S., Hölbling, D., Rastner, P., & Schaffer, N. (2020). Automated detection of rock glaciers using deep learning and object-based image analysis. *Remote Sensing of Environment*, *250*, 112033. https://doi.org/10.1016/j.rse.2020.112033~~

~~Rodríguez-Rodríguez, L., Jiménez-Sánchez, M., Domínguez-Cuesta, M. J., Rinterknecht, V., & Pallàs, R. (2017). Timing of last deglaciation in the Cantabrian Mountains (Iberian Peninsula; North Atlantic Region) based on in situ-produced ^{10}Be exposure dating. *Quaternary Science Reviews*, *171*, 166–181. https://doi.org/10.1016/j.quascirev.2017.07.012~~

~~Sandeman, A. F., & Ballantyne, C. K. (1996). Talus rock glaciers in scotland: Characteristics and controls on formation. *Scottish Geographical Magazine*, *112*(3), 138–146. https://doi.org/10.1080/14702549608554947~~

~~Scambos, T. A., Dutkiewicz, M. J., Wilson, J. C., & Bindschadler, R. A. (1992). Application of image cross-correlation to the measurement of glacier velocity using satellite image data. *Remote Sensing of Environment*, *42*(3), 177–186. https://doi.org/10.1016/0034-4257(92)90101-O~~

~~Scapozza, C., Lambiel, C., Bozzini, C., Mari, S., & Conedera, M. (2014). Assessing the rock glacier kinematics on three different timescales: A case study from the southern Swiss Alps. *Earth Surface Processes and Landforms*, *39*(15), 2056–2069. https://doi.org/10.1002/esp.3599~~

~~Schimmelpfennig, I., Schaefer, J. M., Akçar, N., Koffman, T., Ivy-Ochs, S., Schwartz, R., Finkel, R. C., Zimmerman, S., & Schlüchter, C. (2014). A chronology of Holocene and Little Ice Age glacier culminations of the Steingletscher, Central Alps, Switzerland, based on high-sensitivity beryllium-10 moraine dating. *Earth and Planetary Science Letters*, *393*, 220–230. https://doi.org/10.1016/j.epsl.2014.02.046~~

~~Schindelwig, I., Akçar, N., Kubik, P. W., & Schlüchter, C. (2012). Lateglacial and early Holocene dynamics of adjacent valley glaciers in the Western Swiss Alps. *Journal of Quaternary Science*, *27*(1), 114–124. https://doi.org/10.1002/jqs.1523~~

~~Shean, D. E., Alexandrov, O., Moratto, Z. M., Smith, B. E., Joughin, I. R., Porter, C., & Morin, P. (2016). An automated, open-source pipeline for mass production of digital elevation models (DEMs) from very-high-resolution commercial stereo satellite imagery. *ISPRS Journal of Photogrammetry and Remote Sensing*, *116*, 101–117. https://doi.org/10.1016/j.isprsjprs.2016.03.012~~

~~Steinemann, O., Reitner, J. M., Ivy-Ochs, S., Christl, M., & Synal, H. A. (2020). Tracking rockglacier evolution in the Eastern Alps from the Lateglacial to the early Holocene. *Quaternary Science Reviews*, *241*. https://doi.org/10.1016/j.quascirev.2020.106424~~

~~Strozzi, T., Caduff, R., Jones, N., Barboux, C., Delaloye, R., Bodin, X., Kääb, A., Mätzler, E., & Schrott, L. (2020). Monitoring Rock Glacier Kinematics with Satellite Synthetic Aperture Radar. *Remote Sensing*, *12*(3), 559. https://doi.org/10.3390/rs12030559~~

~~Thibert, E., Bodin, X., Bonnefoy-Demongeot, M., & Finance, F. (2018). Extracting the time signal in surface velocity changes along 3 decades at Laurichard rock glacier (French Alps). In *researchgate.net*. https://www.researchgate.net/publication/326648894~~

~~Uppala, S. M., KÅllberg, P. W., Simmons, A. J., Andrae, U., Bechtold, V. D. C., Fiorino, M., Gibson, J. K., Haseler, J., Hernandez, A., Kelly, G. A., Li, X., Onogi, K., Saarinen, S., Sokka, N., Allan, R. P., Andersson, E., Arpe, K., Balmaseda, M. A., Beljaars, A. C. M., … Woollen, J. (2005). The ERA-40 re-analysis. *Quarterly Journal of the Royal Meteorological Society*, *131*(612), 2961–3012. https://doi.org/10.1256/qj.04.176~~

~~Valla, P. G., van der Beek, P. A., & Carcaillet, J. (2010). Dating bedrock gorge incision in the French Western Alps (Ecrins-Pelvoux massif) using cosmogenic ^{10}Be. *Terra Nova*, *22*(1), 18–25. https://doi.org/10.1111/j.1365-3121.2009.00911.x~~

~~Vivero, S., & Lambiel, C. (2019). Monitoring the crisis of a rock glacier with repeated UAV surveys. *Geographica Helvetica*, *74*(1), 59–69. https://doi.org/10.5194/gh-74-59-2019~~

~~Wahrhaftig, C., & Cox, A. (1959). Rock glaciers in the Alaska Range. *Bulletin of the Geological Society of America*, *70*(4), 383–436. https://doi.org/10.1130/0016-7606(1959)70[383:RGITAR]2.0.CO;2~~

~~Whalley, W. B. (1974). Origin of rock glaciers. *Journal of Glaciology*, *13*(68), 323–324. https://doi.org/10.3189/s0022143000023145~~

~~Williams, M. W., Knauf, M., Caine, N., Liu, F., & Verplanck, P. L. (2006). Geochemistry and source waters of rock glacier outflow, Colorado Front Range. *Permafrost and Periglacial Processes*, *17*(1), 13–33. https://doi.org/10.1002/ppp.535~~

~~Winkler, S., & Lambiel, C. (2018). Age constraints of rock glaciers in the Southern Alps/New Zealand – Exploring their palaeoclimatic potential. *Holocene*, *28*(5), 778–790. https://doi.org/10.1177/0959683618756802~~

~~Wirsig, C., Zasadni, J., Ivy-Ochs, S., Christl, M., Kober, F., & Schlüchter, C. (2016). A deglaciation model of the Oberhasli, Switzerland. *Journal of Quaternary Science*, *31*(1), 46–59. https://doi.org/10.1002/jqs.2831~~

~~Wirz, V., Gruber, S., Purves, R. S., Beutel, J., Gärtner-Roer, I., Gubler, S., & Vieli, A. (2016). Short-term velocity variations at three rock glaciers and their relationship with meteorological conditions. *Earth Surface Dynamics*, *4*(1), 103–123. https://doi.org/10.5194/esurf-4-103-2016~~

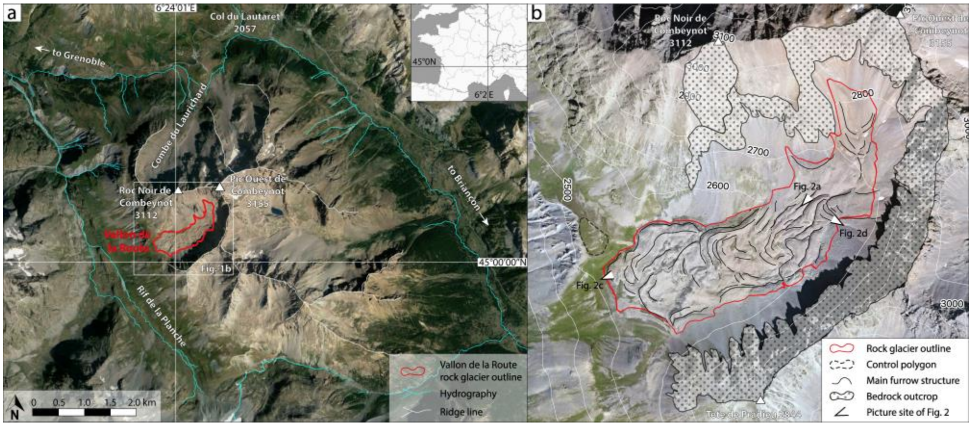

Amschwand, Dominik, Susan Ivy-Ochs, Marcel Frehner, Olivia Steinemann, Marcus Christl, and Christof Vockenhuber. 2021a. “Deciphering the Evolution of the Bleis Marscha Rock Glacier (Val d’Err, Eastern Switzerland) with Cosmogenic Nuclide Exposure Dating, Aerial Image Correlation, and Finite Element Modeling.” *Cryosphere* 15 (4): 2057–81. https://doi.org/10.5194/tc-15-2057-2021.

Anderson, Robert S., Leif S. Anderson, William H. Armstrong, Matthew W. Rossi, and Sarah E. Crump. 2018. “Glaciation of Alpine Valleys: The Glacier – Debris-Covered Glacier – Rock Glacier Continuum.” *Geomorphology* 311: 127–42. https://doi.org/10.1016/j.geomorph.2018.03.015.

Andrés, Nuria, Antonio Gómez-Ortiz, José M. Fernández-Fernández, Luis M. Tanarro, Ferran Salvador-Franch, Marc Oliva, and David Palacios. 2018. “Timing of Deglaciation and Rock Glacier Origin in the Southeastern Pyrenees: A Review and New Data.” *Boreas* 47 (4): 1050–71. https://doi.org/10.1111/bor.12324.

Balco, Greg, John O. Stone, Nathaniel A. Lifton, and Tibor J. Dunai. 2008. “A Complete and Easily Accessible Means of Calculating Surface Exposure Ages or Erosion Rates from ^{10}Be and ^{26}Al Measurements.” *Quaternary Geochronology* 3 (3): 174–95. https://doi.org/10.1016/j.quageo.2007.12.001.

Barboux, Chloé, Reynald Delaloye, and Christophe Lambiel. 2014. “Inventorying Slope Movements in an Alpine Environment Using DInSAR.” *Earth Surface Processes and Landforms* 39 (15): 2087–99. https://doi.org/10.1002/esp.3603.

Barsch, Dietrich. 1977. “nature and importance of mass-wasting by rock glaciers in alpine permafrost environments.” *Earth Surf Process* 2 (2–3): 231–45. https://doi.org/10.1002/esp.3290020213.

Berthling, Ivar. 2011. “Beyond Confusion: Rock Glaciers as Cryo-Conditioned Landforms.” *Geomorphology* 131 (3–4): 98–106. https://doi.org/10.1016/j.geomorph.2011.05.002.

Blöthe, Jan Henrik, Christian Halla, Ellen Schwalbe, Estefania Bottegal, Dario Trombotto Liaudat, and Lothar Schrott. 2021. “Surface Velocity Fields of Active Rock Glaciers and Ice-debris Complexes in the Central Andes of Argentina.” *Earth Surface Processes and Landforms* 46 (2): 504–22. https://doi.org/10.1002/esp.5042.

Bodin, Xavier. 2013. “Present Status and Development of Rock Glacier Complexes in South-Faced Valleys (45°N, French Alps).” *Geografia Fisica e Dinamica Quaternaria* 36 (1): 27–38. https://doi.org/10.4461/GFDQ.2013.36.2.

Bodin, Xavier, Emmanuel Thibert, Olivier Sanchez, Antoine Rabatel, and Stéphane Jaillet. 2018. “Multi-Annual Kinematics of an Active Rock Glacier Quantified from Very High-Resolution DEMs: An Application-Case in the French Alps.” *Remote Sensing* 10 (4). https://doi.org/10.3390/rs10040547.

Böhlert, Ralph, Michael Compeer, Markus Egli, Dagmar Brandová, Max Maisch, Peter W. Kubik, and Wilfried Haeberli. 2011. “A Combination of Relative-Numerical Dating Methods Indicates Two High Alpine Rock Glacier Activity Phases after the Glacier Advance of the Younger Dryas.” *Open Geography Journal* 4: 115–30. https://doi.org/10.2174/1874923201104010115.

Braucher R., D. Bourlès, S. Merchel, J. Vidal Romani, D. Fernadez-Mosquera, K. Marti, L. Léanni, F. Chauvet, M. Arnold, G. Aumaître, K. Keddadouche, Determination of muon attenuation lengths in depth profiles from in situ produced cosmogenic nuclides, Nuclear Instruments and Methods in Physics Research Section B: Beam Interactions with Materials and Atoms, Volume 294, 2013, Pages 484-490, ISSN 0168-583X, https://doi.org/10.1016/j.nimb.2012.05.023.

Brown, Erik Thorson, John M. Edmond, Grant M. Raisbeck, Françoise Yiou, Mark D. Kurz, and Edward J. Brook. 1991. “Examination of Surface Exposure Ages of Antarctic Moraines Using in Situ Produced ^{10}Be and ^{26}Al.” *Geochimica et Cosmochimica Acta* 55 (8): 2269–83. https://doi.org/10.1016/0016-7037(91)90103-C.

Charton, Joanna, Deborah Verfaillie, Vincent Jomelli, and Bernard Francou. 2021. “Early Holocene Rock Glacier Stabilisation at Col Du Lautaret (French Alps): Palaeoclimatic Implications.” *Geomorphology* 394. https://doi.org/10.1016/j.geomorph.2021.107962.

Chenet, Marie, Daniel Brunstein, Vincent Jomelli, Erwan Roussel, Vincent Rinterknecht, Fatima Mokadem, Melody Biette, Vincent Robert, and Laëtitia Léanni. 2016. “^{10}Be Cosmic-Ray Exposure Dating of Moraines and Rock Avalanches in the Upper Romanche Valley (French Alps): Evidence of Two Glacial Advances during the Late Glacial/Holocene Transition." *Quaternary Science Reviews* 148: 209–21. https://doi.org/10.1016/j.quascirev.2016.07.025.

Claude, Anne, Susan Ivy-Ochs, Florian Kober, Marco Antognini, Bernhard Salcher, and Peter W. Kubik. 2014. "The Chironico Landslide (Valle Leventina, Southern Swiss Alps): Age and Evolution." *Swiss Journal of Geosciences* 107 (2–3): 273–91. https://doi.org/10.1007/s00015-014-0170-z.

Cossart, Etienne, Monique Fort, Didier Bourles, Julien Carcaillet, Romain Perrier, Lionel Siame, and Régis Braucher. 2010. "Climatic Significance of Glacier Retreat and Rockglaciers Re-Assessed in the Light of Cosmogenic Dating and Weathering Rind Thickness in Clarée Valley (Briançonnais, French Alps)." *Catena* 80 (3): 204–19. https://doi.org/10.1016/j.catena.2009.11.007.

Coûteaux, Michel, and Jean-Louis Edouard. 1987. "La Déglaciation Du Site Du Lac Des Bèches (Massif Des Ecrins). Etude Pollenanalytique et Glacio-Morphologique." *Revue de Géographie Alpine* 75 (1): 63–77. https://doi.org/10.3406/rga.1987.2666.

Cusicanqui, Diego, Antoine Rabatel, and Christian Vincent. 2021. "Interpretation of Volume and Flux Changes of the Laurichard Rock Glacier Between 1952 and 2019, French Alps." *Journal of Geophysical Research : Earth Surface*. https://doi.org/10.1029/2021JF006161.

Dall'Asta, Elisa, Gianfranco Forlani, Riccardo Roncella, Marina Santise, Fabrizio Diotri, and Umberto Morra di Cella. 2017. "Unmanned Aerial Systems and DSM Matching for Rock Glacier Monitoring." *ISPRS Journal of Photogrammetry and Remote Sensing* 127 (May): 102–14. https://doi.org/10.1016/j.isprsjprs.2016.10.003.

Delaloye, Reynald, and Thomas Echelard. 2020. "IPA Action Group Rock Glacier Inventories and Kinematics (Version 4.1)." *International Permafrost Association*, 1–13.

Delaloye, Reynald, Christophe Lambiel, and Isabelle Gärtner-Roer. 2010. "Aperçu de La Cinématique Des Glaciers Rocheux Dans Les Alpes Suisses. Rythme Saisonnier, Variations Interannuelles et Tendance Pluri-Décennale." *Geographica Helvetica* 65 (2): 135–45. https://doi.org/10.5194/gh-65-135-2010.

Delunel, R. 2010. "Evolution Géomorphologique Du Massif Des Ecrins-Pelvoux Depuis Le Dernier Maximum Glaciaire – Apports Des Nucléides Cosmogéniques Produits in-Situ." *Université Joseph Fourier (Grenoble, France)* Ph. D. Thesis: 236pp.

Delunel, Romain, Peter A. van der Beek, Julien Carcaillet, Didier L. Bourlès, and Pierre G. Valla. 2010. "Frost-Cracking Control on Catchment Denudation Rates: Insights from in Situ Produced ^{10}Be Concentrations in Stream Sediments (Ecrins-Pelvoux Massif, French Western Alps)." *Earth and Planetary Science Letters* 293 (1–2): 72–83. https://doi.org/10.1016/j.epsl.2010.02.020.

Delunel, Romain, Didier L. Bourlès, Peter A. van der Beek, Fritz Schlunegger, Ingo Leya, Jozef Masarik, and Emmanuel Paquet. 2014. "Snow Shielding Factors for Cosmogenic Nuclide Dating Inferred from Long-Term Neutron Detector Monitoring." *Quaternary Geochronology* 24: 16–26. https://doi.org/10.1016/j.quageo.2014.07.003.

Eriksen, H., L. Rouyet, T. R. Lauknes, I. Berthling, K. Isaksen, H. Hindberg, Y. Larsen, and G. D. Corner. 2018. “Recent Acceleration of a Rock Glacier Complex, Ádjet, Norway, Documented by 62 Years of Remote Sensing Observations.” *Geophysical Research Letters* 45 (16): 8314–23. https://doi.org/10.1029/2018GL077605.

Federici, Paolo Roberto, Darryl E. Granger, Marta Pappalardo, Adriano Ribolino, Matteo Spagnolo, and Andrew J. Cyr. 2008. “Exposure Age Dating and Equilibrium Line Altitude Reconstruction of an Egesen Moraine in the Maritime Alps, Italy.” *Boreas* 37 (2): 245–53. https://doi.org/10.1111/j.1502-3885.2007.00018.x.

Fernández-Fernández, José M., David Palacios, Nuria Andrés, Irene Schimmelpfennig, Luis M. Tanarro, Skafti Brynjólfsson, Francisco J. López-Acevedo, Þorsteinn Sæmundsson, and A.S.T.E.R. Team. 2020. “Constraints on the Timing of Debris-Covered and Rock Glaciers: An Exploratory Case Study in the Hólar Area, Northern Iceland.” *Geomorphology* 361: 107196. https://doi.org/10.1016/j.geomorph.2020.107196.

Fleischer, Fabian, Florian Haas, Livia Piermattei, Madlene Pfeiffer, Tobias Heckmann, Moritz Altmann, Jakob Rom, et al. n.d. “Multi-Decadal (1953–2017) Rock Glacier Kinematics Analysed by High-Resolution Topographic Data in the Upper Kaunertal, Austria.” *Tc.Copernicus.Org*. Accessed March 24, 2022. https://tc.copernicus.org/preprints/tc-2021-77/.

Francou, Bernard. 1982. “Chutes de Pierres et Éboulisation Dans Les Parois de l’étage Périglaciaire.” *Revue de Géographie Alpine* 70 (3): 279–300. https://doi.org/10.3406/rga.1982.2508.

Francou, Bernard, and Louis Reynaud. 1992. “10 Year Surficial Velocities on a Rock Glacier (Laurichard, French Alps).” *Permafrost and Periglacial Processes* 3 (3): 209–13. https://doi.org/10.1002/ppp.3430030306.

Frauenfelder, R., and A. Kääb. 2000. “Towards a Palaeoclimatic Model of Rock Glacier Formation in the Swiss Alps.” *Annals of Glaciology* 31: 281–86. https://doi.org/10.3189/172756400781820264.

Frehner, Marcel, Anna Hui Mee Ling, and Isabelle Gärtner-Roer. 2015. “Furrow-and-Ridge Morphology on Rockglaciers Explained by Gravity-Driven Buckle Folding: A Case Study from the Murtèl Rockglacier (Switzerland).” *Permafrost and Periglacial Processes* 26 (1): 57–66. https://doi.org/10.1002/ppp.1831.

Fuchs, Margret C., Ralph Böhlert, Matthias Krbetschek, Frank Preusser, and Markus Egli. 2013. “Exploring the Potential of Luminescence Methods for Dating Alpine Rock Glaciers.” *Quaternary Geochronology* 18: 17–33. https://doi.org/10.1016/j.quageo.2013.07.001.

Gallach, Xavi, Julien Carcaillet, Ludovic Ravanel, Philip Deline, Christophe Ogier, Magali Rossi, Emmanuel Malet, and David Garcia-Sellés. 2020. “Climatic and Structural Controls on Late-glacial and Holocene Rockfall Occurrence in High-elevated Rock Walls of the Mont Blanc Massif (Western Alps).” *Earth Surface Processes and Landforms* 45 (13): 3071–91. https://doi.org/10.1002/esp.4952.

Gallach, Xavi, Ludovic Ravanel, Markus Egli, Dagmar Brandova, Michael Schaepman, Marcus Christl, Stephan Gruber, Philip Deline, Julien Carcaillet, and François Pallandre. 2018. “Timing of Rockfalls in the Mont Blanc Massif (Western Alps): Evidence from Surface Exposure Dating with Cosmogenic ^{10}Be.” *Landslides* 15 (10): 1991–2000. https://doi.org/10.1007/s10346-018-0999-8.

García-Ruiz,JM, D. Palacios, JM Fernández-Fernández, N. Andrés, J. Arnáez, A. Gómez-Villar, J. Santos-González, J. Álvarez-Martínez, N. Lana-Renault, L. Léanni, Glacial stages in the Peña Negra valley, Iberian Range, northern Iberian Peninsula: Assessing the importance of the glacial record in small cirques in a marginal mountain area, Geomorphology, Volume 362, 2020, 107195, ISSN 0169-555X, https://doi.org/10.1016/j.geomorph.2020.107195.

Gardent, Marie, Antoine Rabatel, Jean Pierre Dedieu, and Philip Deline. 2014. "Multitemporal Glacier Inventory of the French Alps from the Late 1960s to the Late 2000s." *Global and Planetary Change* 120: 24–37. https://doi.org/10.1016/j.gloplacha.2014.05.004.

Giardino, John R., and John D. Vitek. 1988. "The Significance of Rock Glaciers in the Glacial-periglacial Landscape Continuum." *Journal of Quaternary Science* 3 (1): 97–103. https://doi.org/10.1002/jqs.3390030111.

Gilbert, G. K. 1904. "Systematic Asymmetry of Crest Lines in the High Sierra of California." *The Journal of Geology* 12 (7): 579–88. https://doi.org/10.1086/621182.

Gosse, John C., and Fred M. Phillips. 2001. "Terrestrial in Situ Cosmogenic Nuclides: Theory and Application." *Quaternary Science Reviews* 20 (14): 1475–1560. https://doi.org/10.1016/S0277-3791(00)00171-2.

Haeberli, Wilfried. 2013. "Mountain Permafrost - Research Frontiers and a Special Long-Term Challenge." *Cold Regions Science and Technology* 96 (December): 71–76. https://doi.org/10.1016/j.coldregions.2013.02.004.

Haeberli, Wilfried, Bernard Hallet, Lukas Arenson, Roger Elconin, Ole Humlum, Andreas Kääb, Viktor Kaufmann, et al. 2006. "Permafrost Creep and Rock Glacier Dynamics." *Permafrost and Periglacial Processes* 17 (3): 189–214. https://doi.org/10.1002/ppp.561.

Hippolyte, Jean Claude, Didier Bourlès, Régis Braucher, Julien Carcaillet, Laëtitia Léanni, Maurice Arnold, and Georges Aumaitre. 2009. "Cosmogenic ^{10}Be Dating of a Sackung and Its Faulted Rock Glaciers, in the Alps of Savoy (France)." *Geomorphology* 108 (3–4): 312–20. https://doi.org/10.1016/j.geomorph.2009.02.024.

Hofmann, Felix Martin, Helena Alexanderson, Philippe Schoeneich, Jordan R. Mertes, and Laëtitia Léanni. 2019. "Post-Last Glacial Maximum Glacier Fluctuations in the Southern Écrins Massif (Westernmost Alps): Insights from ^{10}Be Cosmic Ray Exposure Dating." *Boreas* 48 (4): 1019–41. https://doi.org/10.1111/BOR.12405.

Hormes, Anne, Susan Ivy-Ochs, Peter W. Kubik, Luca Ferreli, and Alessandro Maria Michetti. 2008. "^{10}Be Exposure Ages of a Rock Avalanche and a Late Glacial Moraine in Alta Valtellina, Italian Alps." *Quaternary International* 190 (1): 136–45. https://doi.org/10.1016/j.quaint.2007.06.036.

Humlum, Ole. 2000. "The Geomorphic Significance of Rock Glaciers: Estimates of Rock Glacier Debris Volumes and Headwall Recession Rates in West Greenland." *Geomorphology* 35 (1–2): 41–67. https://doi.org/10.1016/S0169-555X(00)00022-2.

Ikeda, Atsushi, and Norikazu Matsuoka. 2006. "Pebbly versus Bouldery Rock Glaciers: Morphology, Structure and Processes." *Geomorphology* 73 (3–4): 279–96. https://doi.org/10.1016/j.geomorph.2005.07.015.

Ikeda, Atsushi, Norikazu Matsuoka, and Andreas Kääb. 2008. “Fast Deformation of Perennially Frozen Debris in a Warm Rock Glacier in the Swiss Alps: An Effect of Liquid Water.” *Journal of Geophysical Research: Earth Surface* 113 (1). https://doi.org/10.1029/2007JF000859.

Ivy-Ochs, S. 2015. “Variaciones Glaciares En Los Alphs Europoes al Final de La Última Glaciación.” *Cuadernos de Investigacion Geografica* 41 (2): 295–315. https://doi.org/10.18172/cig.2750.

Ivy-Ochs, Susan, Hanns Kerschner, Peter W. Kubik, and Christian Schlüchter. 2006. “Glacier Response in the European Alps to Heinrich Event 1 Cooling: The Gschnitz Stadial.” *Journal of Quaternary Science*. https://doi.org/10.1002/jqs.955.

Ivy-Ochs, Susan, Hanns Kerschner, Anne Reuther, Frank Preusser, Klaus Heine, Max Maisch, Peter W. Kubik, and Christian Schlüchter. 2008. “Chronology of the Last Glacial Cycle in the European Alps.” *Journal of Quaternary Science* 23 (6–7): 559–73. https://doi.org/10.1002/jqs.1202.

Johnson, P. G. 1980. “Glacier- Rock Glacier Transition in the Southwest Yukon Territory, Canada.” *Arctic and Alpine Research* 12 (2): 195–204. https://doi.org/10.2307/1550516.

Jones, Darren B., Stephan Harrison, Karen Anderson, and W. Brian Whalley. 2019. “Rock Glaciers and Mountain Hydrology: A Review.” *Earth-Science Reviews* 193 (March): 66–90. https://doi.org/10.1016/j.earscirev.2019.04.001.

Kaab, A., W. Haeberli, and G. Hilmar Gudmundsson. 1997. “Analysing the Creep of Mountain Permafrost Using High Precision Aerial Photogrammetry: 25 Years of Monitoring Gruben Rock Glacier, Swiss Alps.” *Permafrost and Periglacial Processes* 8 (4): 409–26. https://doi.org/10.1002/(SICI)1099-1530(199710/12)8:4<409::AID-PPP267>3.0.CO;2-C.

Kääb, Andreas, Tazio Strozzi, Tobias Bolch, Rafael Caduff, H. kon Trefall, Markus Stoffel, and Alexander Kokarev. 2021. “Inventory and Changes of Rock Glacier Creep Speeds in Ile Alatau and Kungöy Ala-Too, Northern Tien Shan, since the 1950s.” *Cryosphere* 15 (2): 927–49. https://doi.org/10.5194/tc-15-927-2021.

Kellerer-Pirklbauer, Andreas. 2017. “Potential Weathering by Freeze-Thaw Action in Alpine Rocks in the European Alps during a Nine Year Monitoring Period.” *Geomorphology* 296: 113–31. https://doi.org/10.1016/j.geomorph.2017.08.020.

Kellerer-Pirklbauer, Andreas, and Matthias Rieckh. 2016. “Monitoring Nourishment Processes in the Rooting Zone of an Active Rock Glacier in an Alpine Environment.” *Zeitschrift Fur Geomorphologie* 60 (August): 99–121. https://doi.org/10.1127/zfg_suppl/2016/00245.

Kelly, Meredith A., Jean François Buoncristiani, and Christian Schlüchter. 2004. “A Reconstruction of the Last Glacial Maximum (LGM) Ice-Surface Geometry in the Western Swiss Alps and Contiguous Alpine Regions in Italy and France.” *Eclogae Geologicae Helvetiae* 97 (1): 57–75. https://doi.org/10.1007/s00015-004-1109-6.

Kenner, Robert, Marcia Phillips, Philippe Limpach, Jan Beutel, and Martin Hiller. 2018. “Monitoring Mass Movements Using Georeferenced Time-Lapse Photography: Ritigraben Rock Glacier, Western Swiss Alps.” *Cold Regions Science and Technology* 145 (January): 127–34. https://doi.org/10.1016/j.coldregions.2017.10.018.

Kohl, C. P., and K. Nishiizumi. 1992. “Chemical Isolation of Quartz for Measurement of In-Situ -Produced Cosmogenic Nuclides.” *Geochimica et Cosmochimica Acta*. Pergamon. https://doi.org/10.1016/0016-7037(92)90401-4.

Krainer, Karl, David Bressan, Benjamin Dietre, Jean Nicolas Haas, Irka Hajdas, Kathrin Lang, Volkmar Mair, et al. 2015. "A 10,300-Year-Old Permafrost Core from the Active Rock Glacier Lazaun, Southern Ötztal Alps (South Tyrol, Northern Italy)." *Quaternary Research (United States)* 83 (2): 324–35. https://doi.org/10.1016/j.yqres.2014.12.005.

Lifton, Nathaniel, Tatsuhiko Sato, and Tibor J. Dunai. 2014. "Scaling in Situ Cosmogenic Nuclide Production Rates Using Analytical Approximations to Atmospheric Cosmic-Ray Fluxes." *Earth and Planetary Science Letters* 386 (January): 149–60. https://doi.org/10.1016/j.epsl.2013.10.052.

Liu, L., C. I. Millar, R. D. Westfall, and H. A. Zebker. 2013. "Surface Motion of Active Rock Glaciers in the Sierra Nevada, California, USA: Inventory and a Case Study Using InSAR." *Cryosphere* 7 (4): 1109–19. https://doi.org/10.5194/tc-7-1109-2013.

Liu, Zhengyu, Jiang Zhu, Yair Rosenthal, Xu Zhang, Bette L. Otto-Bliesner, Axel Timmermann, Robin S. Smith, Gerrit Lohmann, Weipeng Zheng, and Oliver Elison Timm. 2014. "The Holocene Temperature Conundrum." *Proceedings of the National Academy of Sciences of the United States of America* 111 (34): E3501. https://doi.org/10.1073/PNAS.1407229111/-/DCSUPPLEMENTAL.

Marcer, Marco, Xavier Bodin, Alexander Brenning, Philippe Schoeneich, Raphaële Charvet, and Frédéric Gottardi. 2017. "Permafrost Favorability Index: Spatial Modeling in the French Alps Using a Rock Glacier Inventory." *Frontiers in Earth Science* 5 (December). https://doi.org/10.3389/feart.2017.00105.

Marcer, Marco, Alessandro Cicoira, Diego Cusicanqui, Xavier Bodin, Thomas Echelard, Renée Obregon, and Philippe Schoeneich. 2021. "Rock Glaciers throughout the French Alps Accelerated and Destabilised since 1990 as Air Temperatures Increased." *Communications Earth & Environment* 2 (1): 1–11. https://doi.org/10.1038/s43247-021-00150-6.

Martin, L. C.P., P. H. Blard, G. Balco, J. Lavé, R. Delunel, N. Lifton, and V. Laurent. 2017. "The CREp Program and the ICE-D Production Rate Calibration Database: A Fully Parameterizable and Updated Online Tool to Compute Cosmic-Ray Exposure Ages." *Quaternary Geochronology* 38: 25–49. https://doi.org/10.1016/j.quageo.2016.11.006.

Matthews, John A., and Peter Wilson. 2015. "Improved Schmidt-Hammer Exposure Ages for Active and Relict Pronival Ramparts in Southern Norway, and Their Palaeoenvironmental Implications." *Geomorphology* 246: 7–21. https://doi.org/10.1016/j.geomorph.2015.06.002.

Merchel, S., and U. Herpers. 1999. "An Update on Radiochemical Separation Techniques for the Determination of Long-Lived Radionuclides via Accelerator Mass Spectrometry." *Radiochimica Acta* 84 (4): 215–19. https://doi.org/10.1524/ract.1999.84.4.215.

Micheletti, Natan, Marj Tonini, and Stuart N. Lane. 2017. "Geomorphological Activity at a Rock Glacier Front Detected with a 3D Density-Based Clustering Algorithm." *Geomorphology* 278: 287–97. https://doi.org/10.1016/j.geomorph.2016.11.016.

Monegato, Giovanni, Giancarlo Scardia, Irka Hajdas, Francesca Rizzini, and Andrea Piccin. 2017. "The Alpine LGM in the Boreal Ice-Sheets Game." *Scientific Reports* 7 (1): 1–8. https://doi.org/10.1038/s41598-017-02148-7.

Monnier, Sébastien, and Christophe Kinnard. 2015. “Reconsidering the Glacier to Rock Glacier Transformation Problem: New Insights from the Central Andes of Chile.” *Geomorphology* 238 (June): 47–55. https://doi.org/10.1016/j.geomorph.2015.02.025.

Moran, Andrew P., Susan Ivy-Ochs, Michael Schuh, Markus Christl, and Hanns Kerschner. 2016. “Evidence of Central Alpine Glacier Advances during the Younger Dryas–Early Holocene Transition Period.” *Boreas* 45 (3): 398–410. https://doi.org/10.1111/bor.12170.

Necsoiu, Marius, Alexandru Onaca, Sarah Wigginton, and Petru Urdea. 2016. “Rock Glacier Dynamics in Southern Carpathian Mountains from High-Resolution Optical and Multi-Temporal SAR Satellite Imagery.” *Remote Sensing of Environment* 177 (May): 21–36. https://doi.org/10.1016/j.rse.2016.02.025.

Nuth, C., and Kääb. 2011. “Co-Registration and Bias Corrections of Satellite Elevation Data Sets for Quantifying Glacier Thickness Change.” *Cryosphere* 5 (1): 271–90. https://doi.org/10.5194/tc-5-271-2011.

Paasche, Øyvind, Svein Olaf Dahl, Reidar Løvlie, Jostein Bakke, and Atle Nesje. 2007. “Rockglacier Activity during the Last Glacial-Interglacial Transition and Holocene Spring Snowmelting.” *Quaternary Science Reviews* 26 (5–6): 793–807. https://doi.org/10.1016/j.quascirev.2006.11.017.

Palacios, David, Marc Oliva, Antonio Gómez-Ortiz, Nuria Andrés, José M. Fernández-Fernández, Irene Schimmelpfennig, Laëtitia Léanni, and A.S.T.E.R. Team. 2020. “Climate Sensitivity and Geomorphological Response of Cirque Glaciers from the Late Glacial to the Holocene, Sierra Nevada, Spain.” *Quaternary Science Reviews* 248 (November). https://doi.org/10.1016/j.quascirev.2020.106617.

Pavón-Carrasco, Francisco Javier, María Luisa Osete, Joan Miquel Torta, and Angelo De Santis. 2014. “A Geomagnetic Field Model for the Holocene Based on Archaeomagnetic and Lava Flow Data.” *Earth and Planetary Science Letters* 388 (February): 98–109. https://doi.org/10.1016/j.epsl.2013.11.046.

Portenga, Eric W., and Paul R. Bierman. 2011. “Understanding Earth’s Eroding Surface with 10Be.” *GSA Today* 21 (8): 4–10. https://doi.org/10.1130/G111A.1.

Protin, M., I. Schimmelpfennig, Jean Louis Mugnier, Ludovic Ravanel, Melaine Le Roy, Philip Deline, Vincent Favier, et al. 2019. “Climatic Reconstruction for the Younger Dryas/Early Holocene Transition and the Little Ice Age Based on Paleo-Extents of Argentière Glacier (French Alps).” *Quaternary Science Reviews* 221 (October). https://doi.org/10.1016/j.quascirev.2019.105863.

RGIK. 2020. “Rock Glacier Inventory Using InSAR (Kinematic Approach), Practical Guidelines v3.0.2.”

Robson, Benjamin Aubrey, Tobias Bolch, Shelley MacDonell, Daniel Hölbling, Philipp Rastner, and Nicole Schaffer. 2020. “Automated Detection of Rock Glaciers Using Deep Learning and Object-Based Image Analysis.” *Remote Sensing of Environment* 250 (December): 112033. https://doi.org/10.1016/j.rse.2020.112033.

Robson, Benjamin Aubrey, Shelley MacDonell, Álvaro Ayala, Tobias Bolch, Pål Ringkjøb Nielsen, and Sebastián Vivero. 2022. “Glacier and Rock Glacier Changes since the 1950s in the La Laguna Catchment, Chile.” *The Cryosphere* 16 (2): 647–65. https://doi.org/10.5194/TC-16-647-2022.

Rodríguez-Rodríguez, Laura, Montserrat Jiménez-Sánchez, María José Domínguez-Cuesta, Vincent Rinterknecht, and Raimon Pallàs. 2017. "Timing of Last Deglaciation in the Cantabrian Mountains (Iberian Peninsula; North Atlantic Region) Based on in Situ-Produced 10Be Exposure Dating." *Quaternary Science Reviews* 171 (September): 166–81. https://doi.org/10.1016/j.quascirev.2017.07.012.

Le Roy, Melaine, Philip Deline, Julien Carcaillet, Irene Schimmelpfennig, and Magali Ermini. 2017. "^{10}Be Exposure Dating of the Timing of Neoglacial Glacier Advances in the Ecrins-Pelvoux Massif, Southern French Alps." *Quaternary Science Reviews* 178 (December): 118–38. https://doi.org/10.1016/j.quascirev.2017.10.010.

Sandeman, Alison F., and Colin K. Ballantyne. 1996. "Talus Rock Glaciers in Scotland: Characteristics and Controls on Formation." *Scottish Geographical Magazine* 112 (3): 138–46. https://doi.org/10.1080/14702549608554947.

Scambos, Theodore A., Melanie J. Dutkiewicz, Jeremy C. Wilson, and Robert A. Bindschadler. 1992. "Application of Image Cross-Correlation to the Measurement of Glacier Velocity Using Satellite Image Data." *Remote Sensing of Environment* 42 (3): 177–86. https://doi.org/10.1016/0034-4257(92)90101-O.

Scapozza, Cristian, Christophe Lambiel, Claudio Bozzini, Stefano Mari, and Marco Conedera. 2014. "Assessing the Rock Glacier Kinematics on Three Different Timescales: A Case Study from the Southern Swiss Alps." *Earth Surface Processes and Landforms* 39 (15): 2056–69. https://doi.org/10.1002/esp.3599.

Schimmelpfennig, Irene, Joerg M. Schaefer, Naki Akçar, Tobias Koffman, Susan Ivy-Ochs, Roseanne Schwartz, Robert C. Finkel, Susan Zimmerman, and Christian Schlüchter. 2014. "A Chronology of Holocene and Little Ice Age Glacier Culminations of the Steingletscher, Central Alps, Switzerland, Based on High-Sensitivity Beryllium-10 Moraine Dating." *Earth and Planetary Science Letters* 393: 220–30. https://doi.org/10.1016/j.epsl.2014.02.046.

Schindelwig, Inga, Naki Akçar, Peter W. Kubik, and Christian Schlüchter. 2012. "Lateglacial and Early Holocene Dynamics of Adjacent Valley Glaciers in the Western Swiss Alps." *Journal of Quaternary Science* 27 (1): 114–24. https://doi.org/10.1002/jqs.1523.

Shean, David E., Oleg Alexandrov, Zachary M. Moratto, Benjamin E. Smith, Ian R. Joughin, Claire Porter, and Paul Morin. 2016. "An Automated, Open-Source Pipeline for Mass Production of Digital Elevation Models (DEMs) from Very-High-Resolution Commercial Stereo Satellite Imagery." *ISPRS Journal of Photogrammetry and Remote Sensing* 116 (June): 101–17. https://doi.org/10.1016/j.isprsjprs.2016.03.012.

Steinemann, Olivia, Jürgen M. Reitner, Susan Ivy-Ochs, Marcus Christl, and Hans Arno Synal. 2020. "Tracking Rockglacier Evolution in the Eastern Alps from the Lateglacial to the Early Holocene." *Quaternary Science Reviews* 241 (August). https://doi.org/10.1016/j.quascirev.2020.106424.

Strozzi, Tazio, Rafael Caduff, Nina Jones, Chloé Barboux, Reynald Delaloye, Xavier Bodin, Andreas Kääb, Eva Mätzler, and Lothar Schrott. 2020. "Monitoring Rock Glacier Kinematics with Satellite Synthetic Aperture Radar." *Remote Sensing* 12 (3): 559. https://doi.org/10.3390/rs12030559.

Thibert, Emmanuel, Xavier Bodin, Mylène Bonnefoy-Demongeot, and François Finance. 2018. "Extracting the Time Signal in Surface Velocity Changes along 3 Decades at Laurichard Rock Glacier (French Alps)." In *5th European Conference on Permafrost, Book of Abstract.* Presented at the EUCOP5, Laboratoire EDYTEM, Chamonix, France (pp. 615-616).

Uppala, S. M., P. W. KÅllberg, A. J. Simmons, U. Andrae, V. Da Costa Bechtold, M. Fiorino, J. K. Gibson, et al. 2005. "The ERA-40 Re-Analysis." *Quarterly Journal of the Royal Meteorological Society* 131 (612): 2961–3012. https://doi.org/10.1256/qj.04.176.

Valla, Pierre G., Peter A. van der Beek, and Julien Carcaillet. 2010. "Dating Bedrock Gorge Incision in the French Western Alps (Ecrins-Pelvoux Massif) Using Cosmogenic ^{10}Be." *Terra Nova* 22 (1): 18–25. https://doi.org/10.1111/j.1365-3121.2009.00911.x.

Vivero, Sebastián, Xavier Bodin, David Farías-Barahona, Shelley MacDonell, Nicole Schaffer, Benjamin Aubrey Robson, and Christophe Lambiel. 2021. "Combination of Aerial, Satellite, and UAV Photogrammetry for Quantifying Rock Glacier Kinematics in the Dry Andes of Chile (30°S) Since the 1950s." *Frontiers in Remote Sensing* 2 (November). https://doi.org/10.3389/FRSEN.2021.784015/PDF.

Vivero, Sebastián, and Christophe Lambiel. 2019. "Monitoring the Crisis of a Rock Glacier with Repeated UAV Surveys." *Geographica Helvetica* 74 (1): 59–69. https://doi.org/10.5194/gh-74-59-2019.

Wahrhaftig, Clyde, and Allan Cox. 1959. "Rock Glaciers in the Alaska Range." *Bulletin of the Geological Society of America* 70 (4): 383–436. https://doi.org/10.1130/0016-7606(1959)70[383:RGITAR]2.0.CO;2.

Whalley, W. Brian. 1974. "Origin of Rock Glaciers." *Journal of Glaciology* 13 (68): 323–24. https://doi.org/10.3189/s0022143000023145.

Winkler, Stefan, and Christophe Lambiel. 2018. "Age Constraints of Rock Glaciers in the Southern Alps/New Zealand – Exploring Their Palaeoclimatic Potential." *Holocene* 28 (5): 778–90. https://doi.org/10.1177/0959683618756802.

Wirsig, Christian, Jerzy Zasadni, Susan Ivy-Ochs, Marcus Christl, Florian Kober, and Christian Schlüchter. 2016. "A Deglaciation Model of the Oberhasli, Switzerland." *Journal of Quaternary Science* 31 (1): 46–59. https://doi.org/10.1002/jqs.2831.

Wirz, V., S. Gruber, R. S. Purves, J. Beutel, I. Gärtner-Roer, S. Gubler, and A. Vieli. 2016. "Short-Term Velocity Variations at Three Rock Glaciers and Their Relationship with Meteorological Conditions." *Earth Surface Dynamics* 4 (1): 103–23. https://doi.org/10.5194/esurf-4-103-2016.

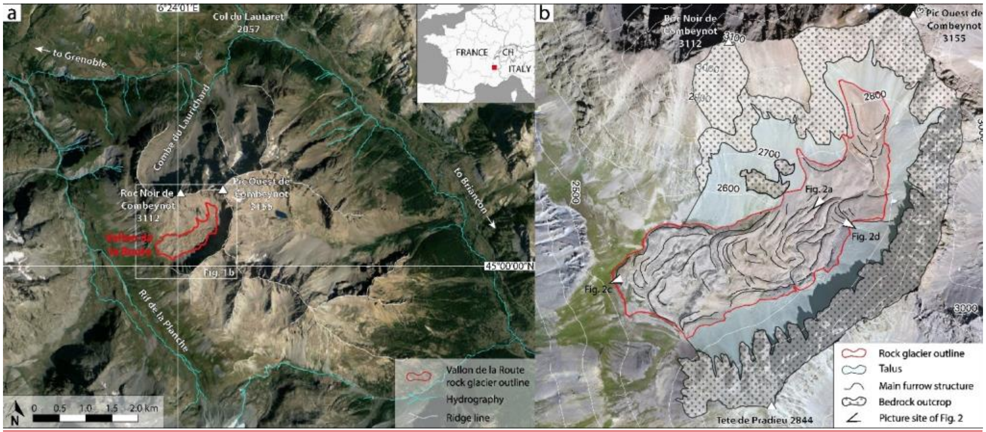

Figure 1: a. Regional map of the Combeynot massif showing the Vallon de la Route rock~~-~~ glacier and surrounding topography (Satellite image from ©~~-~~Google Earth 2020). Outline of the rock glacier (red), hydrography (cyan) and ridge line (white) from Bodin (2007). Inset ~~show~~shows location of the Vallon de la Route rock glacier within western Europe b. Map of the Vallon de la Route rock glacier, with outline of the rock glacier, main furrow structures, outline of the bedrock outcrops (from Bodin, 2007) and location/orientation of pictures presented in Figure 2. Satellite image from Bing Aerial ©~~-~~Microsoft.

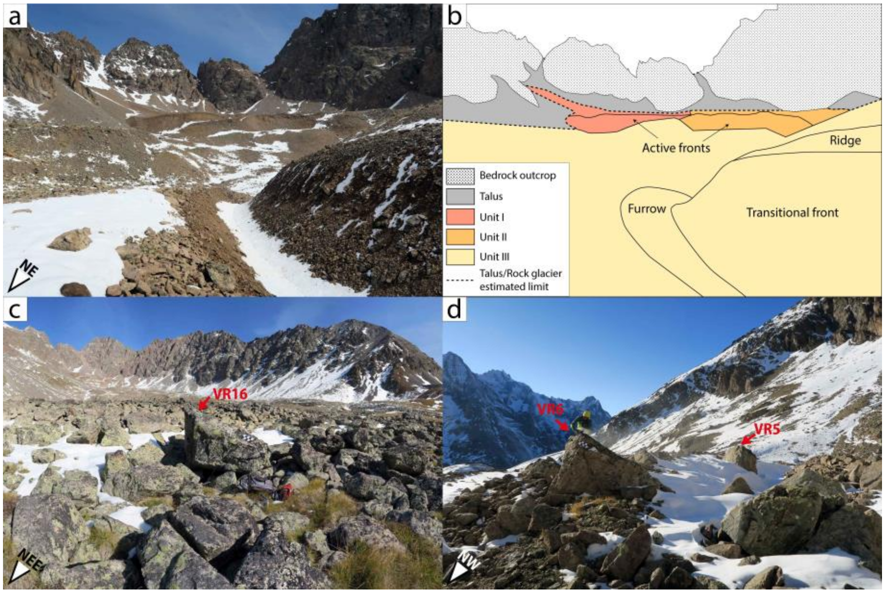
a
NE
b
Bedrock outcrop
Talus
Unit I
Unit II
Unit III
Talus/Rock glacier estimated limit
Active fronts
Ridge
Furrow
Transitional front
c
VR16
NEE
d
VR6
VR5
NW

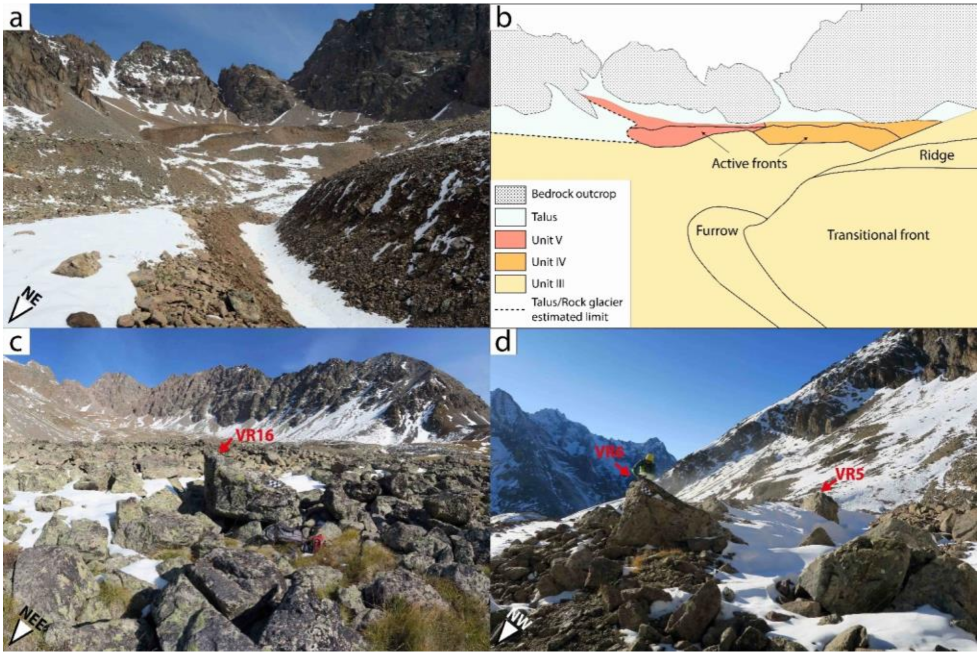

Figure 2: a-b. Picture (a) looking toward the NE and geomorphological interpretation (b) of the rock glacier units ~~I, II~~III, IV and ~~III~~V, with bedrock outcrops, talus, ridge, furrow and fronts. c. Picture looking toward the NEE of the relict unit ~~V~~I and sampled boulder (VR16). d. Picture looking toward the NW of the ~~landform E~~ridge I where two different boulders were sampled (VR5 and VR6). Picture locations and orientations are indicated on Figure 1b.

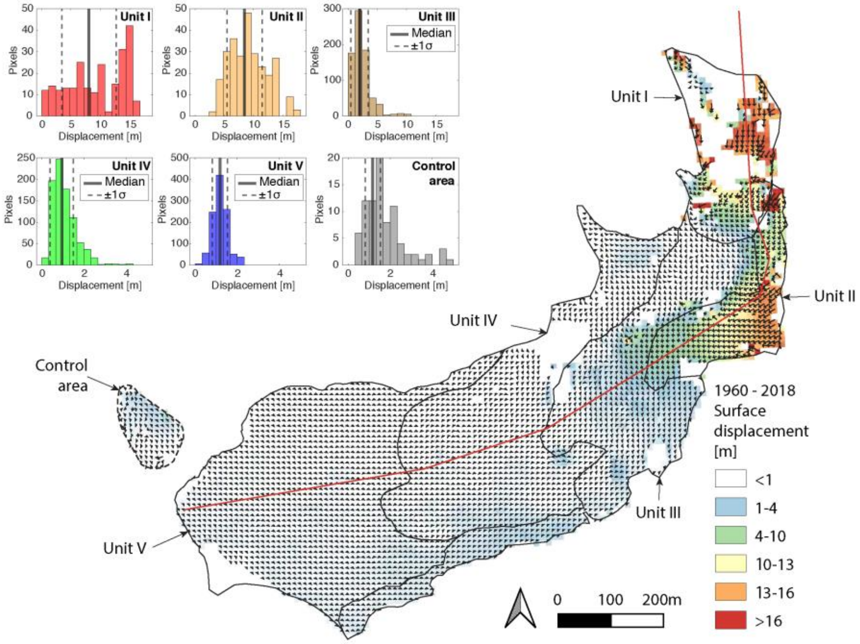
Unit I
Unit II
Unit III
Median
±1σ
Unit IV
Unit V
Control area
Pixels
Displacement [m]
Unit I
Unit II
Unit IV
Control area
Unit III
Unit V
1960 - 2018 Surface displacement [m]
<1
1-4
4-10
10-13
13-16
>16
0
100
200m

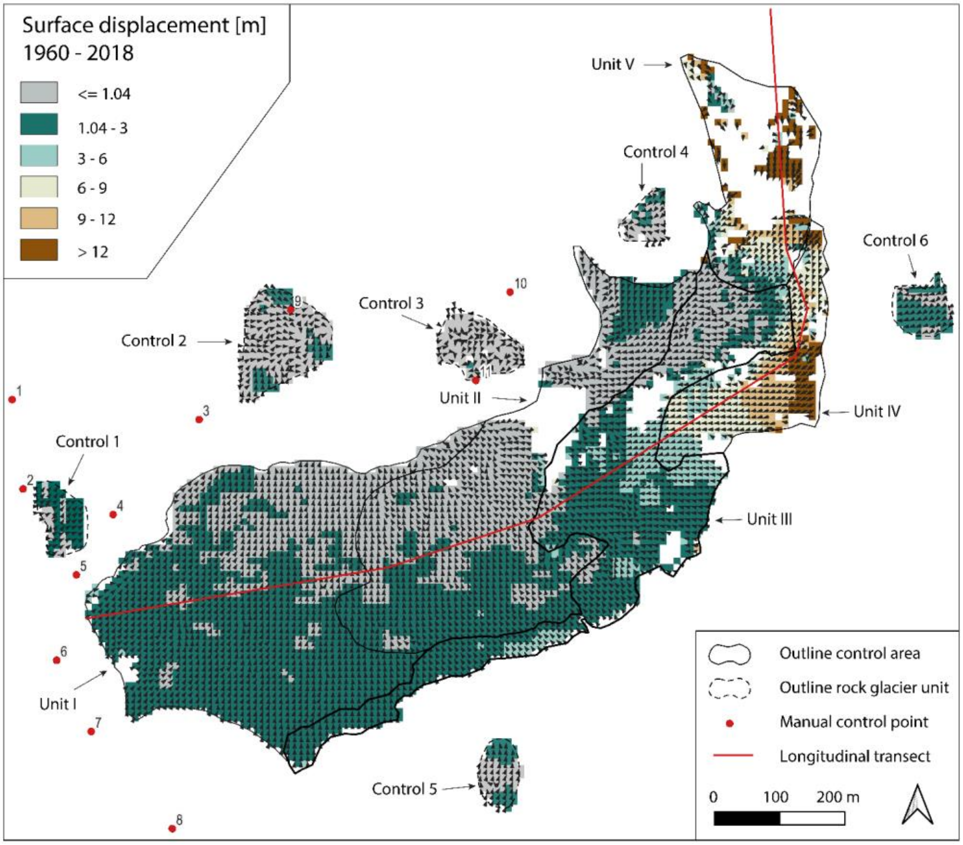

Figure 3: Surface displacement map (1960-2018) of the Vallon de la Route rock glacier. Red line is the longitudinal transect used to extract surface displacement (~~Fig. 4a~~Figure 5a). Black lines outline the different units of the rock~~-~~ glacier system. The dashed black line delimits the stable terrain control ~~area~~areas and red dots show the locations of the manual control points used to quantify uncertainties in the image correlation. ~~Inset histograms (upper-left corner) depict distribution of surface displacements within each individual unit and for the control area.~~ Non-mapped area are the results of the filtering process as described in Section 3.1.3.

Formatted: French (France)

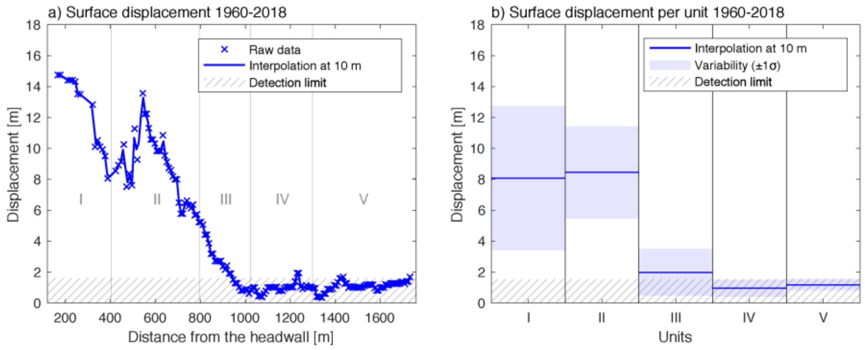
a) Surface displacement 1960-2018
Raw data
Interpolation at 10 m
Detection limit
Displacement [m]
Distance from the headwall [m]
I
II
III
IV
V
b) Surface displacement per unit 1960-2018
Interpolation at 10 m
Variability (±1σ)
Detection limit
Displacement [m]
Units

~~Figure 4: a.~~

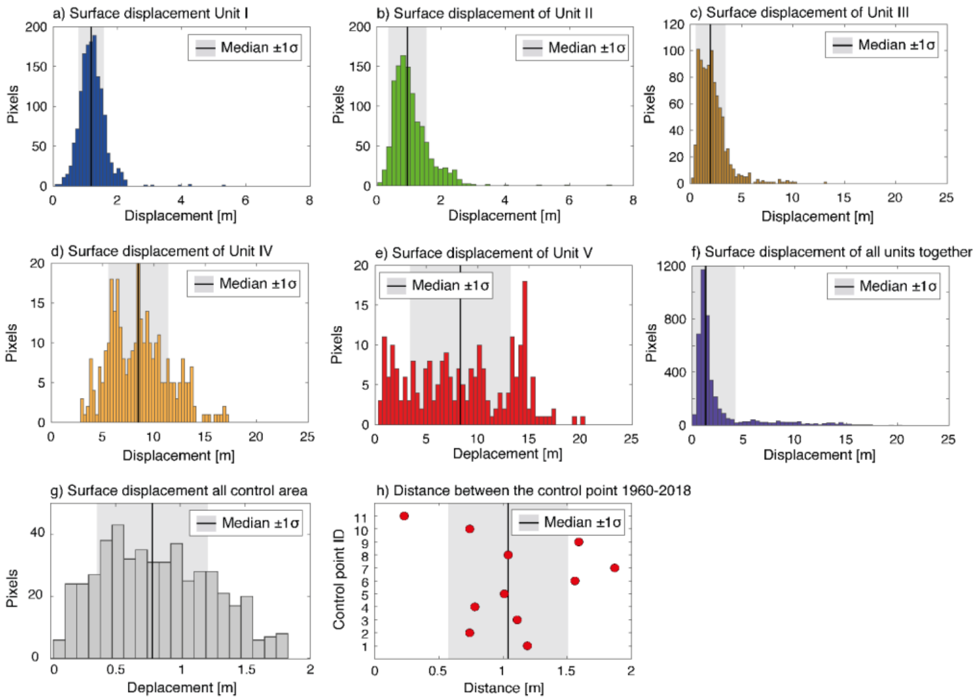
a) Surface displacement Unit I
b) Surface displacement of Unit II
c) Surface displacement of Unit III
d) Surface displacement of Unit IV
e) Surface displacement of Unit V
f) Surface displacement of all units together
g) Surface displacement all control area
h) Distance between the control point 1960-2018
Median ±1σ
Pixels
Displacement [m]
Deplacement [m]
Control point ID
Distance [m]

Figure 4: a-f. Histograms of the surface displacements and median (±1σ) values extracted for each unit are and the entire rock glacier. g. Histograms of the surface displacements and median (±1σ) values extracted from the entire control areas as shown in Figures 3 and A1. Independent histograms of surface displacement values for each control area are presented in Figure A3. h. Distance between the two orthomosaics (1960 and 2018) manually estimated on control point (stable features) as shown in Figures 3 and A1 and Table 2.

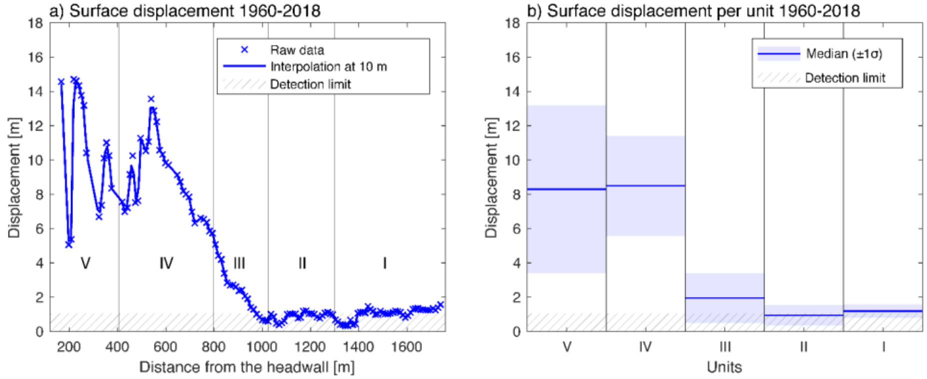

Figure 5: a. Surface displacement (1960-2018) extracted following the longitudinal transect (red line on Fig. 3) with identification of Units I to V. The blue line represents the 10-m interpolation of the raw data. b. Median surface displacement in each rock~~-~~ glacier unit with its ±1σ variability (see ~~Fig. 3~~Figure 4 for histograms). The cross-hatched pattern represents the detection limit defined by median value of the control ~~area (Fig. 3~~areas (Figure 4) used as a threshold value for detection of rock~~-~~ glacier surface displacement.

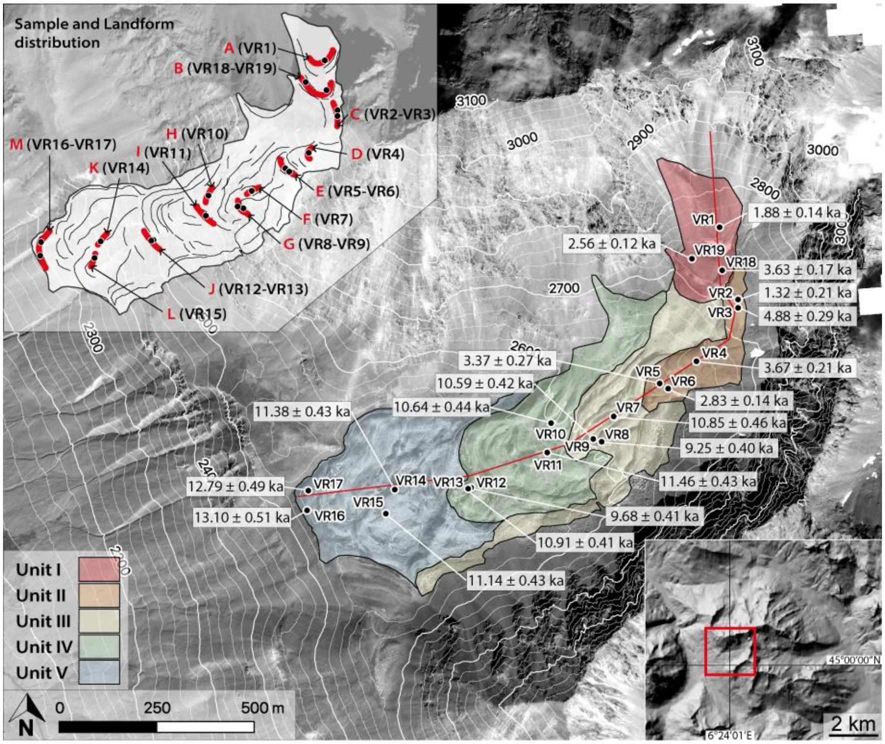
Sample and Landform distribution
A (VR1)
B (VR18-VR19)
C (VR2-VR3)
D (VR4)
E (VR5-VR6)
F (VR7)
G (VR8-VR9)
H (VR10)
I (VR11)
J (VR12-VR13)
K (VR14)
L (VR15)
M (VR16-VR17)
3100
3000
2900
2800
2700
2600
2400
2300
VR1
1.88 ± 0.14 ka
VR19
2.56 ± 0.12 ka
VR18
3.63 ± 0.17 ka
VR2
1.32 ± 0.21 ka
VR3
4.88 ± 0.29 ka
VR4
3.67 ± 0.21 ka
VR5
3.37 ± 0.27 ka
VR6
2.83 ± 0.14 ka
VR7
10.85 ± 0.46 ka
VR8
9.25 ± 0.40 ka
VR9
11.46 ± 0.43 ka
VR10
10.59 ± 0.42 ka
VR11
10.64 ± 0.44 ka
VR12
9.68 ± 0.41 ka
VR13
10.91 ± 0.41 ka
VR14
11.38 ± 0.43 ka
VR15
11.14 ± 0.43 ka
VR16
13.10 ± 0.51 ka
VR17
12.79 ± 0.49 ka
Unit I
Unit II
Unit III
Unit IV
Unit V
N
0
250
500 m
45°00'00"N
6°24'01'E
2 km

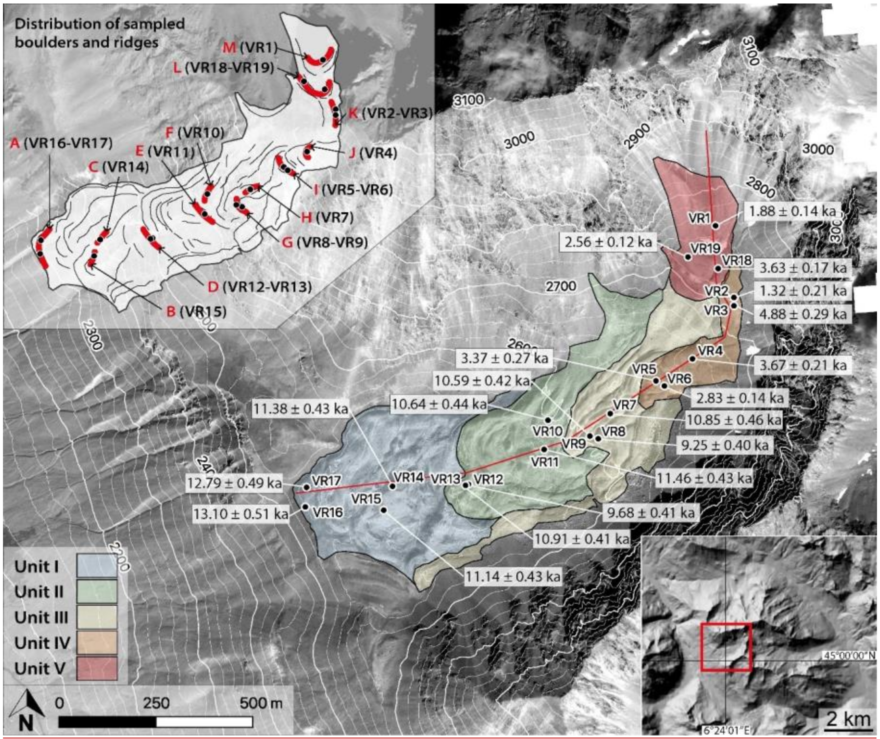

Figure ~~5~~6: Map of the Vallon de la Route rock glacier, with units and sample locations. Hillshade DEM has been produced from Lidar scanning with 0.5-m resolution~~,~~; white lines show elevation isolines. Red line is the longitudinal transect used to extract surface displacement (~~Fig. 4a~~Figure 5a). Individual ^{10}Be surface-exposure ages are shown with one standard deviation (Table 2). The lower right inset shows the location of the study area within the Combeynost massif (red box). Upper left inset shows the samples (black dots) and ~~landforms~~ridges (red lines) ~~distribution~~distributed over the main furrow structures (black lines).

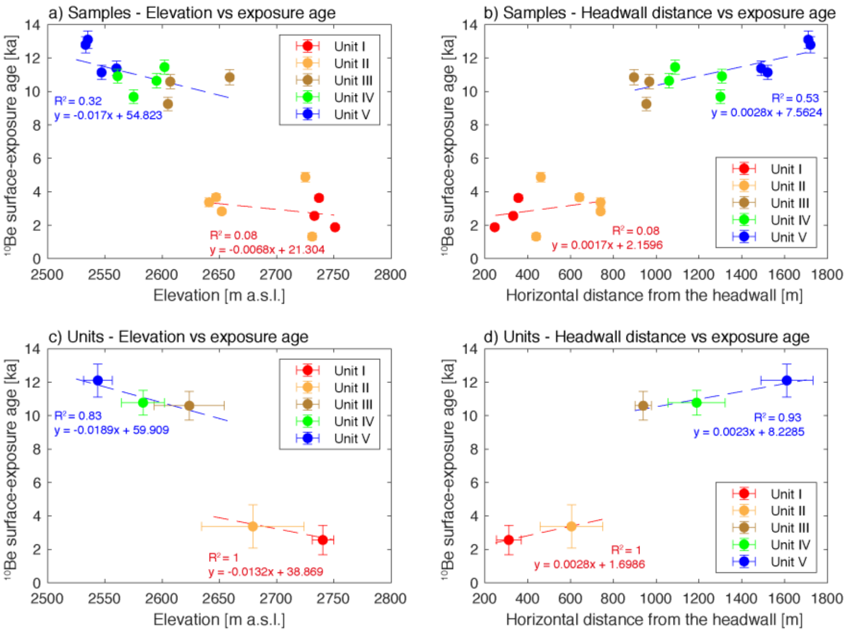
a) Samples - Elevation vs exposure age
b) Samples - Headwall distance vs exposure age
c) Units - Elevation vs exposure age
d) Units - Headwall distance vs exposure age
^{10}Be surface-exposure age [ka]
Elevation [m a.s.l.]
Horizontal distance from the headwall [m]
Unit I
Unit II
Unit III
Unit IV
Unit V
R² = 0.32
y = -0.017x + 54.823
R² = 0.08
y = -0.0068x + 21.304
R² = 0.53
y = 0.0028x + 7.5624
R² = 0.08
y = 0.0017x + 2.1596
R² = 0.83
y = -0.0189x + 59.909
R² = 1
y = -0.0132x + 38.869
R² = 0.93
y = 0.0023x + 8.2285
R² = 1
y = 0.0028x + 1.6986
0
2
4
6
8
10
12
14
2500
2550
2600
2650
2700
2750
2800
200
400
600
800
1000
1200
1400
1600
1800

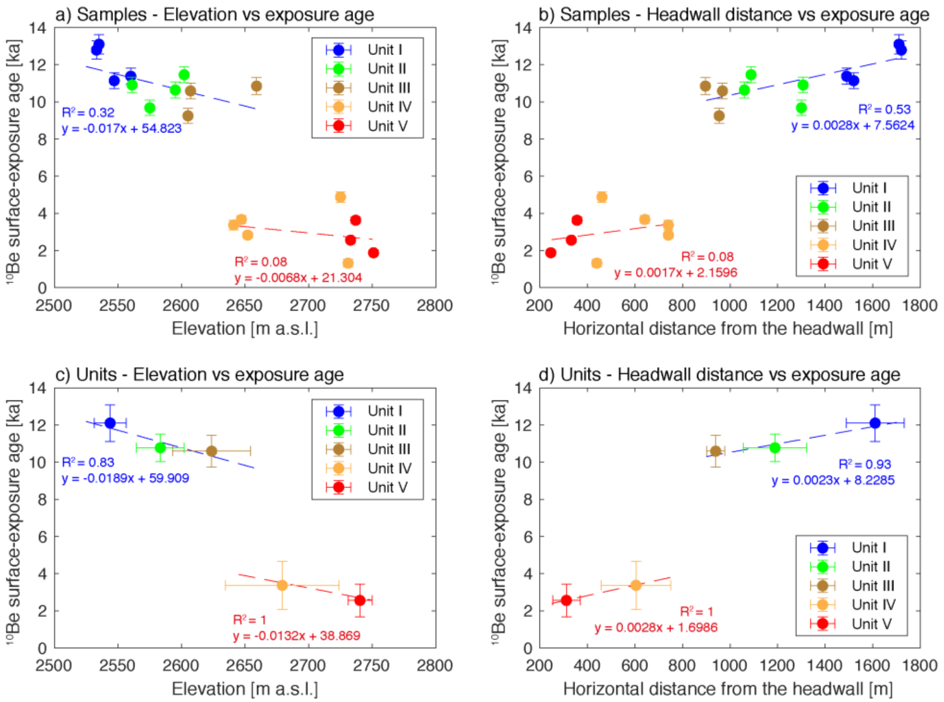

Figure ~~6~~7: ^{10}Be surface-exposure ages of individual samples (a, b) and units (c, d, median values) plotted against elevation (left panels) and horizontal distance to the headwall (right panels). The red and blue dashed lines represent the linear regressions for cluster 1 (Units I, II and ~~II~~III) and 2 (Units ~~II,~~ IV and V), respectively~~. The dotted black line represents the linear regression for the entire dataset~~.

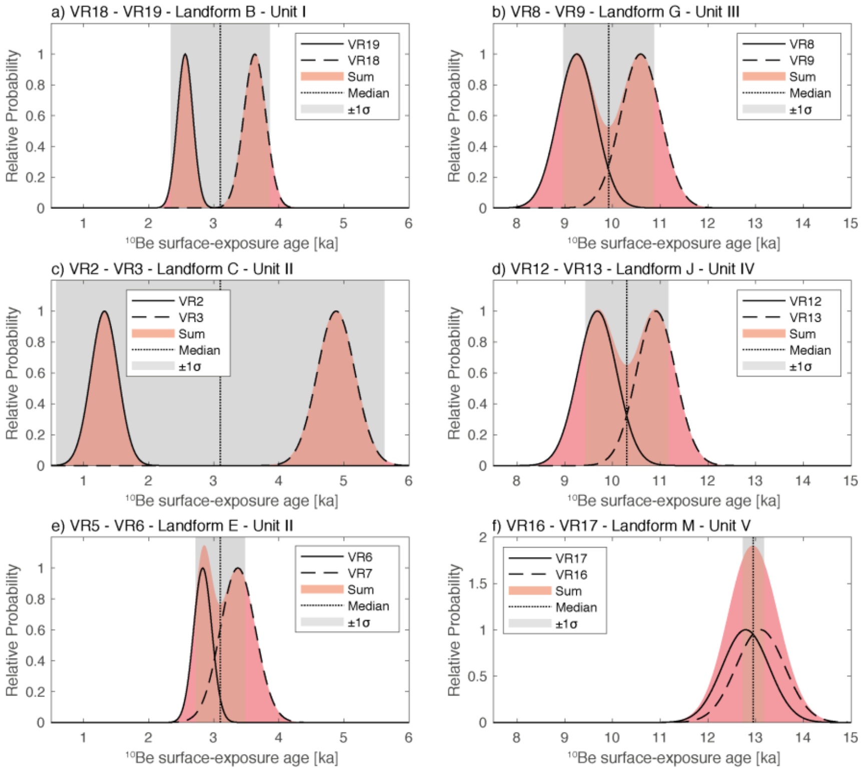
a) VR18 - VR19 - Landform B - Unit I
b) VR8 - VR9 - Landform G - Unit III
c) VR2 - VR3 - Landform C - Unit II
d) VR12 - VR13 - Landform J - Unit IV
e) VR5 - VR6 - Landform E - Unit II
f) VR16 - VR17 - Landform M - Unit V
Relative Probability
^{10}Be surface-exposure age [ka]
VR19
VR18
VR8
VR9
VR2
VR3
VR12
VR13
VR6
VR7
VR17
VR16
Sum
Median
±1σ
0
0.2
0.4
0.6
0.8
1
0.5
1.5
2
1
2
3
4
5
6
8
9
10
11
12
13
14
15

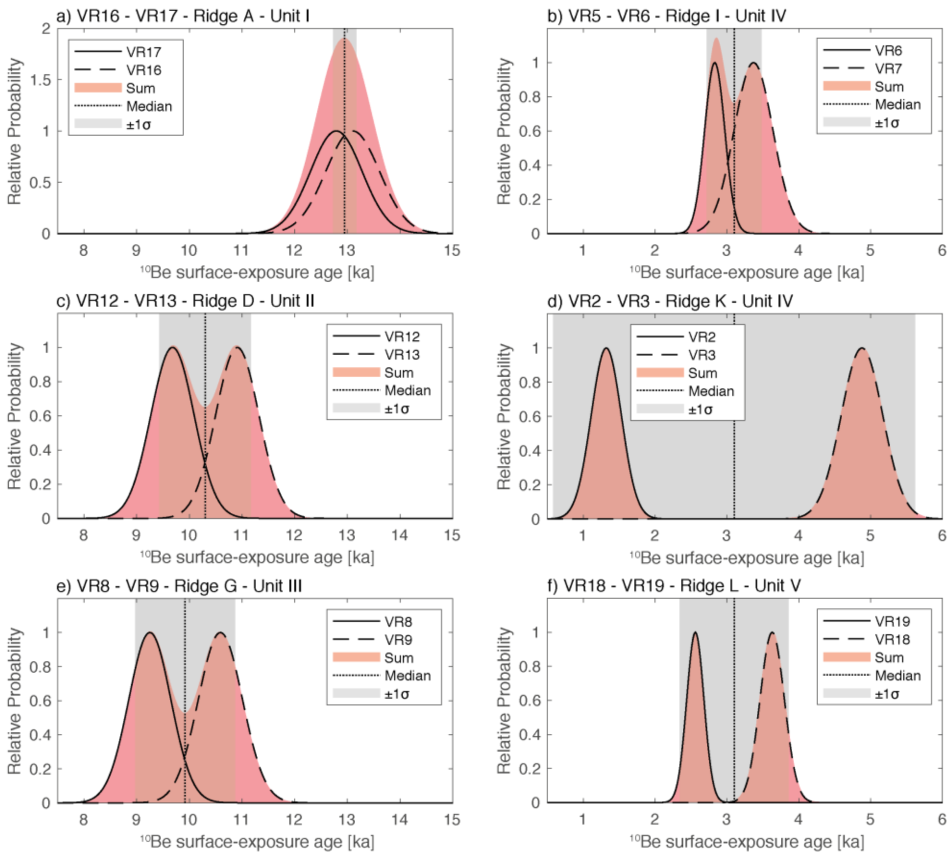

Figure ~~7~~8: Probability ~~plots~~distributions of the individual ^{10}Be surface-exposure ages, sum and median for each ~~landform~~ridge (similar results in ~~Fig. A3~~Figure A4 for each unit in Supplementary material).

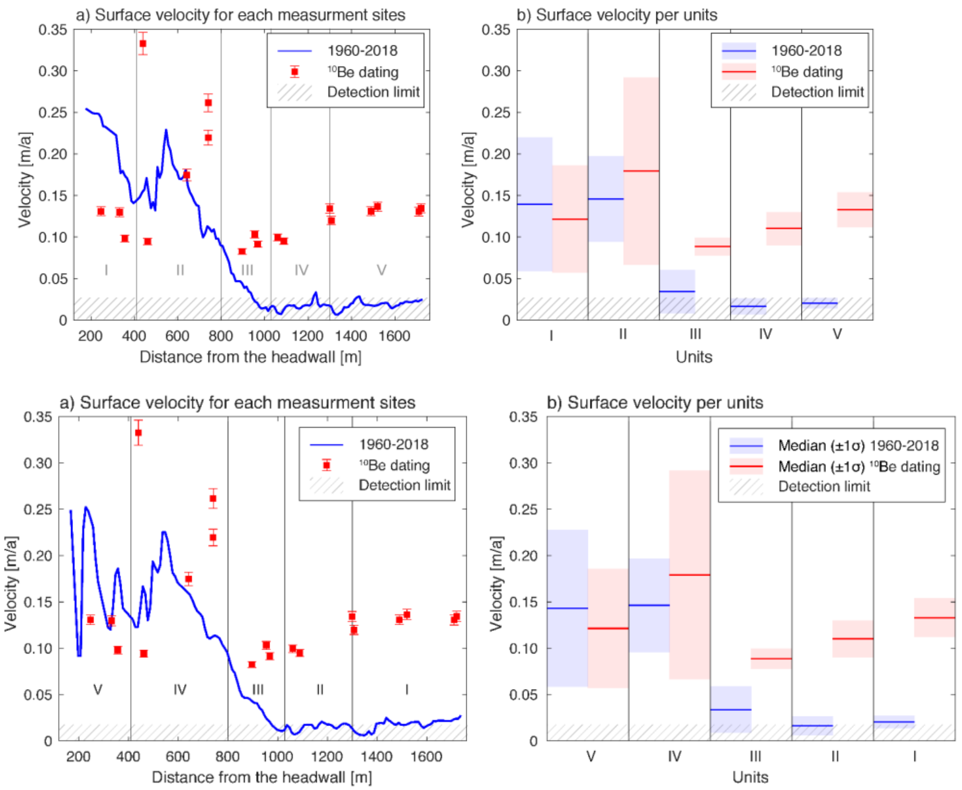

Figure ~~8~~9: a. Rock~~-~~ glacier surface velocity from ^{10}Be surface-exposure dating (distance from the headwall divided by the ^{10}Be surface-exposure age, red squares) and from orthoimage correlation (IMCORR, SAGA package in QGIS, 1960-2018 interval, ~~blueline~~blue line). b. Median surface velocities are presented for each independent method and each individual unit with their standard deviation (±1σ). The dashed pattern represents the detection limit (0.026 m/a) defined by median value of the control ~~area~~areas on Figure 3 (used as a threshold value to detect rock~~-~~ glacier surface movement).

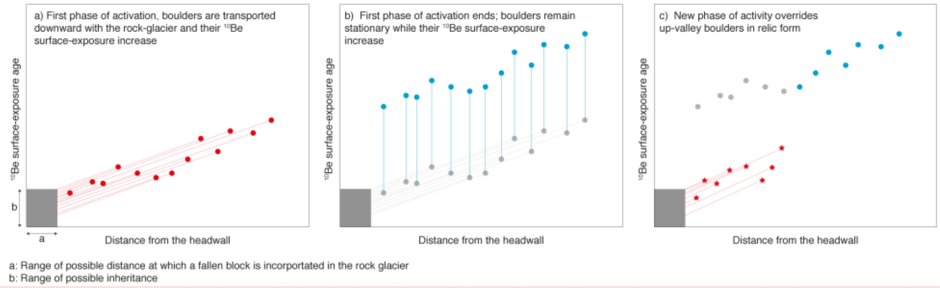

Formatted: English (United States)

Figure ~~9~~10: Schematic interpretation of the evolution of the ^{10}Be surface-exposure age patterns as a function of distance from the headwall, considering two phases of rock-glacier activity and stochastic rockfall delivery of boulders. See section 5.3 for details.

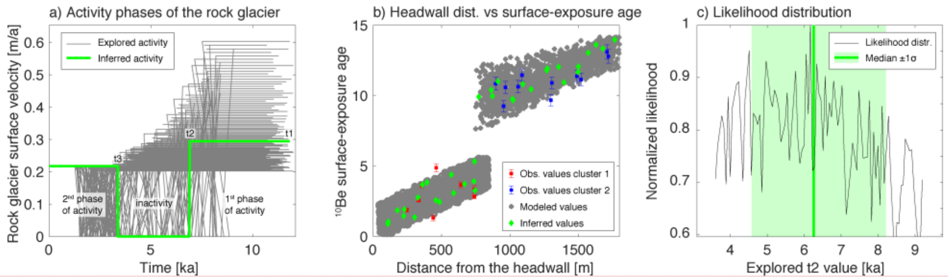

Formatted: English (United States)

Figure ~~10~~11: a) Activity phases of the rock glacier defined as the evolution of the rock glacier surface velocity in time (explored ~~ones~~histories and best-fitting ~~one~~history are shown respectively ~~in~~ grey and green lines). b) Relationship between ^{10}Be surface-exposure age and distance to the headwall. Observed values of the cluster 1 and 2, respectively in red and blue squares. ~~Modeled~~Modelled and best-fitting values in grey and green respectively. c) Likelihood distribution of the inversion exploring the time at which the 1st phase of activity ends (t2). See text for details.

Table 1: ~~Samples with geographic~~Geographic details within the rock~~-~~ glacier system of the Vallon de la Route (Combeynot massif, France~~).~~) of the samples collected for ^{10}Be surface-exposure dating. Units are area of the rock glacier that have been defined geomorphologically. ~~Landforms~~Ridges are ~~ridges where samples have been collected,~~also indicated (Figure 3), on 6 of them two replicate boulders have been sampled. Ridge code goes from A at the lowest elevation to M at the highest elevation. The distance to the headwall has been measured following the ~~center~~centre line of the rock glacier starting at the foot of the headwall (red line in ~~Fig. 3, black line in Fig. 5~~Figures 3 and 6).

Sample ID	Latitude [dec°]	Longitude [dec°]	Elevation [m a.s.l.]	Distance to the headwall [m]	Height of the sample from the ground [cm]	Unit	Landform
VR1	45.0081	6.4088	2751	246	130	I	A
VR2	45.0064	6.4093	2731	356	220	II	C
VR3	45.0063	6.4093	2725	332	230	II	C
VR4	45.0051	6.4079	2647	439	240	II	D
VR5	45.0046	6.4068	2641	461	300	II	E
VR6	45.0045	6.4069	2652	641	150	II	E
VR7	45.0039	6.4051	2659	740	240	III	F
VR8	45.0033	6.4047	2605	740	240	III	G
VR9	45.0034	6.4044	2607	896	150	III	G
VR10	45.0038	6.4031	2595	954	210	IV	H
VR11	45.0031	6.4029	2602	968	400	IV	I
VR12	45.0024	6.4004	2575	1060	320	IV	J
VR13	45.0024	6.4003	2561	1088	500	IV	J
VR14	45.0024	6.3979	2560	1300	160	V	K
VR15	45.0019	6.3976	2547	1307	400	V	L
VR16	45.0020	6.3950	2535	1490	160	V	M
VR17	45.0025	6.3951	2533	1520	180	V	M
VR18	45.0071	6.4089	2737	1710	70	I	B
VR19	45.0074	6.4079	2733	1720	100	I	B

Sample ID	Latitude [dec°]	Longitude [dec°]	Elevation [m a.s.l.]	Distance to the headwall [m]	Height of the sample from the ground [cm]	Unit	Ridge
VR1	45.0081	6.4088	2751	246	130	V	M
VR2	45.0064	6.4093	2731	356	220	IV	K
VR3	45.0063	6.4093	2725	332	230	IV	K
VR4	45.0051	6.4079	2647	439	240	IV	J
VR5	45.0046	6.4068	2641	461	300	IV	I
VR6	45.0045	6.4069	2652	641	150	IV	I
VR7	45.0039	6.4051	2659	740	240	III	H
VR8	45.0033	6.4047	2605	740	240	III	G
VR9	45.0034	6.4044	2607	896	150	III	G
VR10	45.0038	6.4031	2595	954	210	II	F
VR11	45.0031	6.4029	2602	968	400	II	E
VR12	45.0024	6.4004	2575	1060	320	II	D
VR13	45.0024	6.4003	2561	1088	500	II	D
VR14	45.0024	6.3979	2560	1300	160	I	C
VR15	45.0019	6.3976	2547	1307	400	I	B
VR16	45.0020	6.3950	2535	1490	160	I	A
VR17	45.0025	6.3951	2533	1520	180	I	A
VR18	45.0071	6.4089	2737	1710	70	V	L
VR19	45.0074	6.4079	2733	1720	100	V	L

Table 2: Sample details, analytical data related to ^{10}Be measurements and surface-exposure ages for the rock~~-~~ glacier system of the Vallon de la Route (Combeynot massif, France), and inputs for Crep calculator (crep.otelo.univ-lorraine.fr; Martin et al., 2017). We used the production rate (4.16 ±0.10 at/g~~$^{-1}$ a^{-1}~~/a) derived by Claude et al. (2014) at the Chironico landslide site. The ^{10}Be surface-exposure ages are presented with ±1σ external error and ±1σ internal error (in brackets). Shielding correction includes the topographic shielding due to surrounding landscape and the dip of the sampled surface calculated with the online calculators CRONUS-Earth online calculators (Balco et al., 2008, http://hess.ess.washington.edu/math). The density of the rock~~-~~ boulder samples is assumed to be 2.75 g~~ cm^{-3}~~/cm^3. ^{10}Be concentrations were corrected with blank ^{10}Be/^{9}Be ratio of 6.28 ±0.534 ×10^{-15}. Snow-cover correction was calculated using Gosse and Phillips (2001) equation with snow density of 0.3 g cm^{-3}, an attenuation length for fast neutrons in snow of 150 g cm^{-2} and a cover of 50 cm of snow for 6 months of the year.

Sample ID	Thickness [cm]	Shielding factor	Quartz weight [g]	Carrier [m ^{9}Be]	^{10}Be/^{9}Be × 10^{-14}	[^{10}Be] [× 10^3 at/g]	^{10}Be surface-exposure age [ka]	Snow corrected ^{10}Be surface-exposure age [ka]
VR1	3	0.87	19.61	0.5115	3.12 ± 0.21	55.9 ± 3.7	1.88 ± 0.14 (0.13)	2.04 ± 0.15 (0.14)
VR2	3	0.92	17.79	0.5073	2.19 ± 0.34	41.7 ± 6.5	1.32 ± 0.21 (0.21)	1.43 ± 0.23 (0.23)
VR3	5	0.91	26.18	0.5114	1.09 ± 0.62	142.6 ± 8.1	4.88 ± 0.29 (0.27)	5.25 ± 0.30 (0.28)
VR4	3	0.93	16.12	0.5100	5.02 ± 0.25	105.9 ± 5.3	3.67 ± 0.21 (0.19)	3.96 ± 0.22 (0.20)
VR5	3	0.93	19.01	0.5102	5.36 ± 0.40	96.0 ± 7.2	3.37 ± 0.27 (0.26)	3.63 ± 0.29 (0.28)
VR6	3	0.92	19.74	0.5121	4.70 ± 0.19	81.4 ± 3.4	2.83 ± 0.14 (0.12)	3.07 ± 0.15 (0.13)
VR7	3	0.93	13.29	0.5100	12.85 ± 0.48	32.9 ± 12.3	10.85 ± 0.46 (0.38)	11.64 ± 0.50 (0.42)
VR8	4	0.94	20.50	0.5106	16.12 ± 0.53	267.8 ± 8.9	9.25 ± 0.40 (0.32)	9.99 ± 0.39 (0.32)
VR9	4	0.93	23.10	0.5102	20.83 ± 0.71	306.8 ± 10.4	10.59 ± 0.42 (0.35)	11.37 ± 0.44 (0.36)
VR10	2	0.96	19.72	0.5110	18.50 ± 0.66	319.8 ± 11.5	10.64 ± 0.44 (0.38)	11.44 ± 0.46 (0.38)
VR11	4	0.95	17.48	0.5095	17.46 ± 0.56	339.5 ± 10.9	11.46 ± 0.43 (0.35)	12.37 ± 0.50 (0.40)
VR12	3	0.96	18.34	0.5104	15.25 ± 0.53	283.0 ± 10.0	9.68 ± 0.41 (0.34)	10.43 ± 0.43 (0.35)
VR13	3	0.93	22.29	0.5110	20.15 ± 0.64	308.1 ± 9.9	10.91 ± 0.41 (0.33)	11.71 ± 0.46 (0.37)
VR14	3	0.96	18.04	0.5100	17.71 ± 0.57	333.9 ± 10.8	11.38 ± 0.43 (0.34)	12.28 ± 0.50 (0.40)
VR15	3	0.97	18.81	0.5090	18.11 ± 0.61	326.8 ± 11.1	11.14 ± 0.43 (0.35)	11.98 ± 0.50 (0.41)
VR16	3	0.95	17.26	0.5092	19.03 ± 0.61	374.5 ± 12.2	13.10 ± 0.51 (0.40)	14.09 ± 0.55 (0.44)
VR17	4	0.97	19.76	0.5089	21.44 ± 0.68	368.3 ± 11.8	12.79 ± 0.49 (0.39)	13.75 ± 0.53 (0.42)
VR18	3	0.91	18.78	0.5086	6.05 ± 0.23	109.3 ± 4.2	3.63 ± 0.17 (0.14)	3.92 ± 0.18 (0.15)
VR19	3	0.91	21.18	0.5094	4.78 ± 0.18	76.5 ± 3.0	2.56 ± 0.12 (0.11)	2.76 ± 0.13 (0.11)

Sample ID	Thickness [cm]	Shielding factor	Quartz weight [g]	Carrier [m ^{9}Be]	^{10}Be/^{9}Be ×10^{-14}	[^{10}Be] [× 10^{3} at/g]	^{10}Be surface-exposure age [ka]	Snow corrected ^{10}Be surface-exposure age [ka]
VR1	3	0.87	19.61	0.5115	3.84 ±0.20	55.9 ±3.7	1.88 ±0.14 (0.13)	2.04 ±0.15 (0.14)
VR2	3	0.92	17.79	0.5073	2.82 ±0.33	41.7 ±6.5	1.32 ±0.21 (0.21)	1.43 ±0.23 (0.23)
VR3	5	0.91	26.18	0.5114	11.58 ±0.62	142.6 ±8.1	4.88 ±0.29 (0.27)	5.25 ±0.30 (0.28)
VR4	3	0.93	16.12	0.5100	5.65 ±0.24	105.9 ±5.3	3.67 ±0.21 (0.19)	3.96 ±0.22 (0.20)
VR5	3	0.93	19.01	0.5102	5.99 ±0.39	96.0 ±7.2	3.37 ±0.27 (0.26)	3.63 ±0.29 (0.28)
VR6	3	0.92	19.74	0.5121	5.33 ±0.18	81.4 ±3.4	2.83 ±0.14 (0.12)	3.07 ±0.15 (0.13)
VR7	3	0.93	13.29	0.5100	13.48 ±0.47	32.9 ±12.3	10.85 ±0.46 (0.38)	11.64 ±0.50 (0.42)
VR8	4	0.94	20.50	0.5106	16.75 ±0.53	267.8 ±8.9	9.25 ±0.40 (0.32)	9.99 ±0.39 (0.32)
VR9	4	0.93	23.10	0.5102	21.46 ±0.70	306.8 ±10.4	10.59 ±0.42 (0.35)	11.37 ±0.44 (0.36)
VR10	2	0.96	19.72	0.5110	19.13 ±0.66	319.8 ±11.5	10.64 ±0.44 (0.38)	11.44 ±0.46 (0.38)
VR11	4	0.95	17.48	0.5095	18.09 ±0.56	339.5 ±10.9	11.46 ±0.43 (0.35)	12.37 ±0.50 (0.40)
VR12	3	0.96	18.34	0.5104	15.88 ±0.53	283.0 ±10.0	9.68 ±0.41 (0.34)	10.43 ±0.43 (0.35)
VR13	3	0.93	22.29	0.5110	20.78 ±0.64	308.1 ±9.9	10.91 ±0.41 (0.33)	11.71 ±0.46 (0.37)
VR14	3	0.96	18.04	0.5100	18.34 ±0.56	333.9 ±10.8	11.38 ±0.43 (0.34)	12.28 ±0.50 (0.40)
VR15	3	0.97	18.81	0.5090	18.74 ±0.61	326.8 ±11.1	11.14 ±0.43 (0.35)	11.98 ±0.50 (0.41)
VR16	3	0.95	17.26	0.5092	19.66 ±0.61	374.5 ±12.2	13.10 ±0.51 (0.40)	14.09 ±0.55 (0.44)
VR17	4	0.97	19.76	0.5089	22.07 ±0.68	368.3 ±11.8	12.79 ±0.49 (0.39)	13.75 ±0.53 (0.42)
VR18	3	0.91	18.78	0.5086	6.68 ±0.22	109.3 ±4.2	3.63 ±0.17 (0.14)	3.92 ±0.18 (0.15)
VR19	3	0.91	21.18	0.5094	5.40 ±0.17	76.5 ±3.0	2.56 ±0.12 (0.11)	2.76 ±0.13 (0.11)

Table 3: ^{10}Be surface-exposure ages for each ~~landform~~ridge of the rock~~-~~ glacier system of the Vallon de la Route (Combeynot massif, France). n represents the number of samples per ~~landform~~ridge. For the ~~landform~~ridges with replicates, the median values are reported with the standard variation ±1σ. For the inheritance estimate, the difference in ^{10}Be concentration of each pair of replicates has been used and ^{10}Be surface-exposure ages have been recalculated assuming origin from the headwall (at an elevation of 2997 m a.s.l.).

Formatted: Superscript

Landform ID		Corresponding sample	Mean elevation [m a.s.l.]	Mean distance to the headwall [m]	Median ^{10}Be surface-exposure age ±1σ [ka]	Variability [%]	Inheritance est. ±1σ [ka]
A	(n=1)	VR1	2751	246	1.88 ± 0.14		
B	(n=2)	VR18 - VR19	2735	344	3.10 ± 0.76	26	0.88 ± 0.4
C	(n=2)	VR2 - VR3	2728	450	3.10 ± 2.52	99	2.88 ± 0.47
D	(n=1)	VR4	2647	641	3.67 ± 0.21		
E	(n=2)	VR5 - VR6	2646	740	3.10 ± 0.38	13	0.39 ± 0.03
F	(n=1)	VR7	2659	896	10.85 ± 0.46		
G	(n=2)	VR8 - VR9	2606	961	9.92 ± 0.95	10	1.06 ± 0.04
H	(n=1)	VR10	2595	1060	10.64 ± 0.44		
I	(n=1)	VR11	2602	1088	11.46 ± 0.43		
J	(n=2)	VR12 - VR13	2568	1303	10.30 ± 0.87	8	0.67 ± 0.03
K	(n=1)	VR14	2560	1490	11.38 ± 0.43		
L	(n=1)	VR15	2547	1520	11.14 ± 0.43		
M	(n=2)	VR16 - VR17	2534	1715	12.95 ± 0.22	2	0.17 ± 0.01

Ridge ID		Corresponding sample	Mean elevation [m a.s.l.]	Mean distance to the headwall [m]	^{10}Be surface-exposure age Median ±1σ [ka]	Variability [%]	Inheritance est. ±1σ [ka]
A	(n=2)	VR16 - VR17	2534	1715	12.95 ±0.22	2	0.17 ±0.01
B	(n=1)	VR15	2547	1520	11.14 ±0.43		
C	(n=1)	VR14	2560	1490	11.38 ±0.43		
D	(n=2)	VR12 - VR13	2568	1303	10.30 ±0.87	8	0.67 ±0.03
E	(n=1)	VR11	2602	1088	11.46 ±0.43		
F	(n=1)	VR10	2595	1060	10.64 ±0.44		
G	(n=2)	VR8 - VR9	2606	961	9.92 ±0.95	10	1.06 ±0.04
H	(n=1)	VR7	2659	896	10.85 ±0.46		
I	(n=2)	VR5 - VR6	2646	740	3.10 ±0.38	13	0.39 ±0.03
J	(n=1)	VR4	2647	641	3.67 ±0.21		
K	(n=2)	VR2 - VR3	2728	450	3.10 ±2.52	99	2.88 ±0.47
L	(n=2)	VR18 - VR19	2735	344	3.10 ±0.76	26	0.88 ±0.40
M	(n=1)	VR1	2751	246	1.88 ±0.14		

Table 4: Median value of the ^{10}Be surface-exposure ages for each unit of the rock-glacier system of the Vallon de la Route (Combeynot massif, France). n represents the number of samples per unit.

Unit ID	Mean elevation [m a.s.l.]	Mean distance to the headwall [m]	Median ^{10}Be surface exposure age ±1σ [ka]	Variability %
Unit I (n=3)	2740 ± 9	311 ± 58	2.56 ± 0.88	34
Unit II (n=5)	2679 ± 45	604 ± 147	3.37 ± 1.30	44
Unit III (n=3)	2624 ± 31	939 ± 38	10.59 ± 0.86	8
Unit IV (n=4)	2583 ± 19	1189 ± 133	10.78 ± 0.74	7
Unit V (n=4)	2544 ± 12	1610 ± 122	12.10 ± 0.99	8

~~**Table 5:**~~ **Surface velocity calculated from ^{10}Be surface-exposure dating (distance from the headwall divided by ^{10}Be surface-exposure age) and from image correlation (IMCORR, SAGA package on QGIS) of orthoimages (1960-2018 interval).** ~~**The median velocities are reported with the standard deviation ±1σ.**~~

Unit ID	Mean elevation [m a.s.l.]	Mean distance to the headwall [m]	Median ^{10}Be surface-exposure age [ka]	Median displacement 1960-2018 [m]	Integrated surface velocity [m/a]	
					^{10}Be surface-exposure age	1960-2018
Unit I	2740 ± 9	311 ± 58	2.56 ± 0.88	8.08 ± 4.66	0.12 ± 0.06	0.14 ± 0.08
Unit II	2679 ± 45	604 ± 147	3.37 ± 1.30	8.45 ± 2.98	0.18 ± 0.11	0.14 ± 0.05
Unit III	2624 ± 31	939 ± 38	10.59 ± 0.86	1.99 ± 1.50	0.89 ± 0.01	0.03 ± 0.02
Unit IV	2583 ± 19	1189 ± 133	10.78 ± 0.74	0.95 ± 0.55	0.11 ± 0.02	0.01 ± 0.01
Unit V	2544 ± 12	1610 ± 122	12.10 ± 0.99	1.18 ± 0.36	0.13 ± 0.02	0.02 ± 0.01

Formatted: English (United States), Kern at 14 pt

Formatted: English (United States), Kern at 14 pt

Formatted: Normal, Left

Formatted: Font: 10 pt, Not Bold

Unit ID	Mean elevation ±1σ [m a.s.l.]	Mean distance to the headwall ±1σ [m]	^{10}Be surface-exposure age		Displacement 1960-2018	Integrated velocity ±1σ [m/a]	
			Median ±1σ [ka]	Variability [%]	Median ±1σ [m]	^{10}Be surface-exposure age	1960-2018
Unit I (n=4)	2544 ±12	1610 ±122	12.10 ±0.99	8	1.19 ±0.40	0.13 ±0.02	0.02 ±0.01
Unit II (n=4)	2583 ±19	1189 ±133	10.78 ±0.74	7	0.95 ±0.60	0.11 ±0.02	0.02 ±0.01
Unit III (n=3)	2624 ±31	939 ±38	10.59 ±0.86	8	1.96 ±1.45	0.89 ±0.01	0.03 ±0.03
Unit IV (n=5)	2679 ±45	604 ±147	3.37 ±1.30	44	8.49 ±2.93	0.18 ±0.11	0.15 ±0.05
Unit V (n=3)	2740 ±9	311 ±58	2.56 ±0.88	34	8.30 ±4.90	0.12 ±0.06	0.14 ±0.08

Appendix

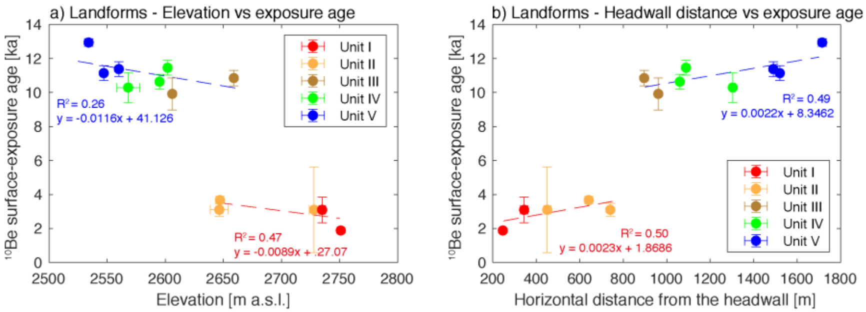
a) Landforms - Elevation vs exposure age
b) Landforms - Headwall distance vs exposure age
¹⁰Be surface-exposure age [ka]
Elevation [m a.s.l.]
Horizontal distance from the headwall [m]
Unit I
Unit II
Unit III
Unit IV
Unit V
R² = 0.26
y = -0.0116x + 41.126
R² = 0.47
y = -0.0089x + 27.07
R² = 0.49
y = 0.0022x + 8.3462
R² = 0.50
y = 0.0023x + 1.8686
0
2
4
6
8
10
12
14
2500
2550
2600
2650
2700
2750
2800
200
400
600
800
1000
1200
1400
1600
1800

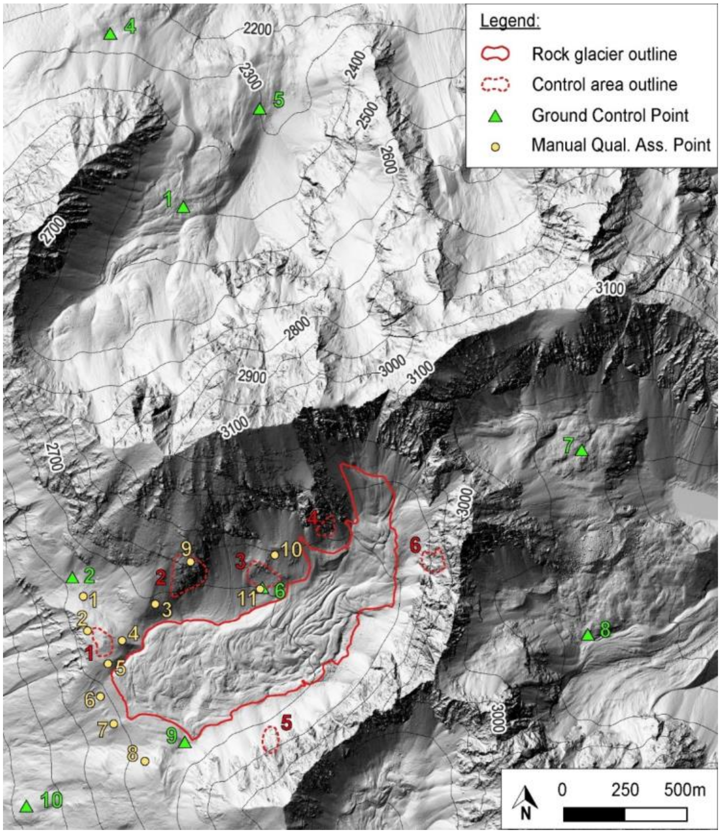

Figure A1: Map showing the location of the ground control points, the control areas and the manual control points used in the remote-sensing analysis.

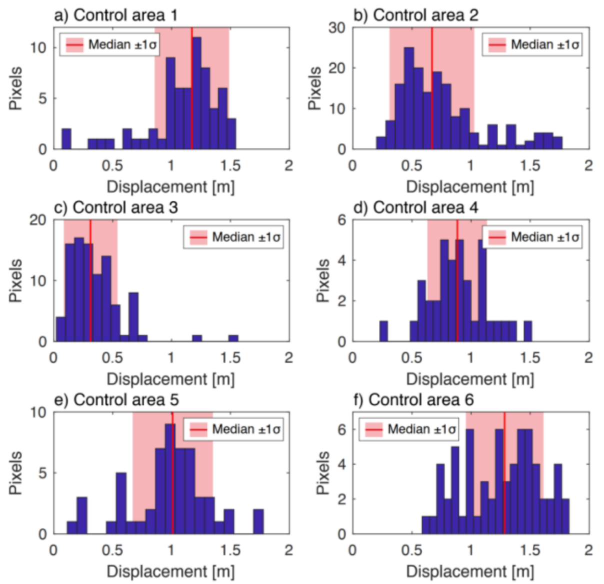

Figure A2: Histograms and median values of the surface displacement for each control area as shown in Figures 3 and A1.

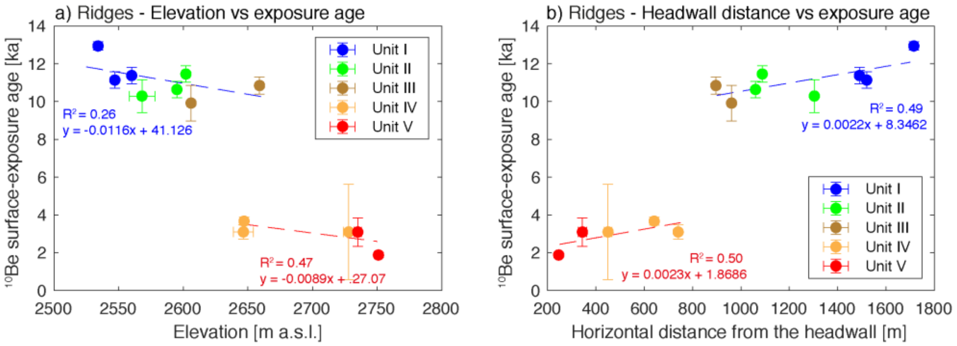

Figure A3: ^{10}Be surface-exposure ages of individual ~~landforms~~ridges (a,b), plotted against elevation (a) and horizontal distance to the headwall (b). The red and blue dashed lines represent the linear regressions for cluster 1 (Units I, II and ~~II~~III) and 2 (Units ~~II,~~ IV and V), respectively.

Formatted: Line spacing: single

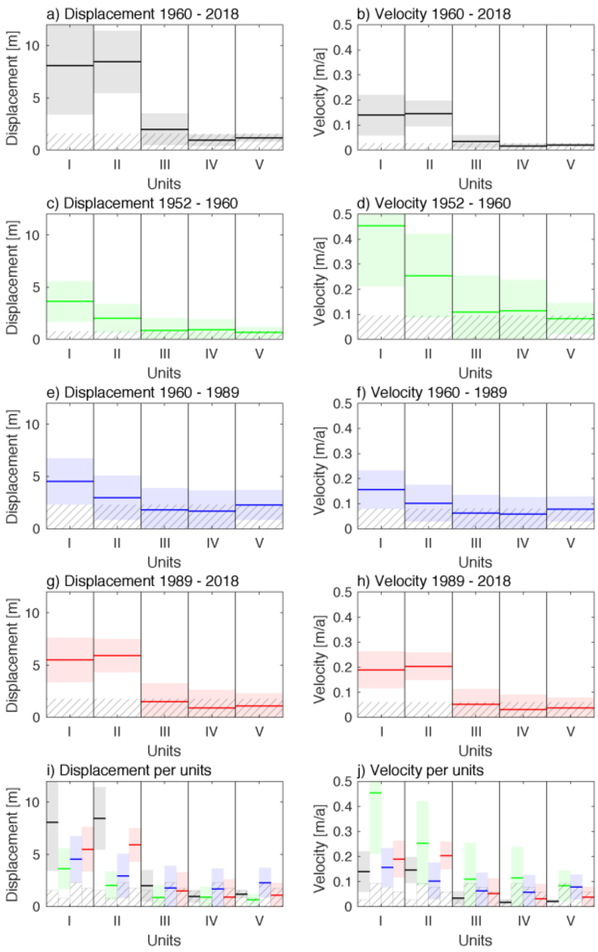

~~**Figure A2: Median surface displacement and velocity for each unit and for every pair of orthoimages tested in this study. Results are presented with the standard deviation ±1σ. The dashed patterns represent the detection limit defined by median value of the control area on Figure 3 used as a threshold value to detect movement.**~~

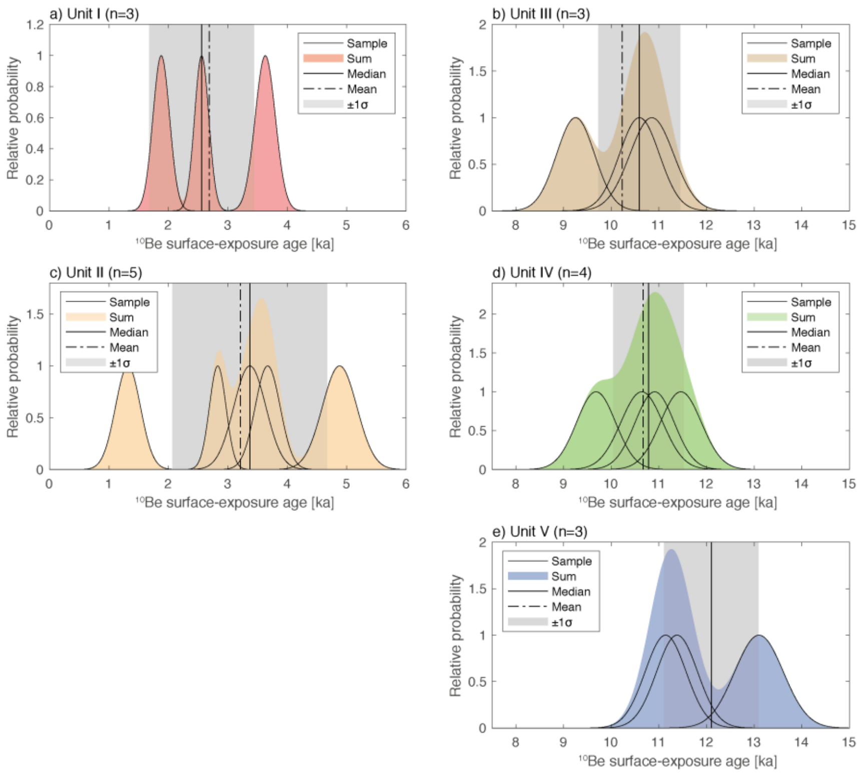

~~Figure A3: Probability plots~~

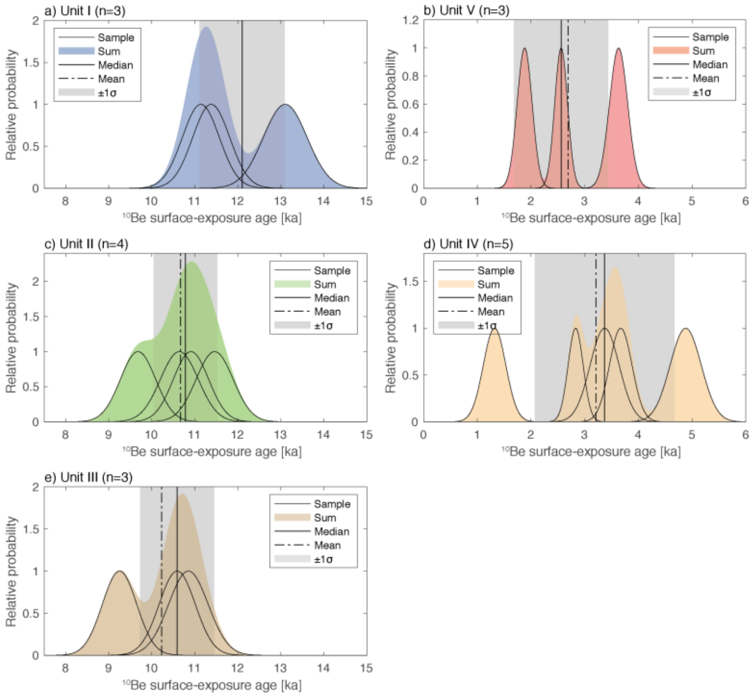

Figure A4: Probability distributions of the ^{10}Be surface-exposure ages for individual samples with sum, mean, median and standard deviation for each unit.

Table A1: Statistics of the ground control points (GCP) used for the co-registrations of the two orthomosaics. Coordinates are mentioned in the EPSG:2154 - RGF93 v1 / Lambert-93 system.

ID	X/Easting	Y/Northing	Z/Altitude [m a.s.l.]	Accuracy X/Y/Z [m]	Error [m]	X error [m]	Y error [m]	Z error [m]	X est	Y est	Z est
GCP1	967692.6055	6441333.13	2445.72998	0.5	0.44	0.33	0.17	0.25	967692.93	6441333.30	2445.98
GCP2	967241.2324	6439828.326	2510.1001	0.5	0.11	0.06	0.04	-0.09	967241.29	6439828.36	2510.01
GCP3	966734.1818	6440583.405	2476.37012	0.5	0.46	-0.30	0.34	0.04	966733.88	6440583.74	2476.41
GCP4	967396.0163	6442035.338	2268.51001	0.5	0.17	0.07	0.08	-0.13	967396.08	6442035.42	2268.38
GCP5	968002.852	6441731.952	2301.87988	0.5	1.03	-0.71	-0.53	-0.53	968002.14	6441731.42	2301.35
GCP6	968011.3061	6439787.281	2603.13989	0.5	0.97	-0.50	0.54	-0.64	968010.81	6439787.82	2602.50
GCP7	969309.2	6440344.9	2749.7099	0.5	0.68	0.50	-0.39	0.26	969309.70	6440344.51	2749.97
GCP8	969334.57	6439595.47	2677.85	0.5	0.45	0.09	0.43	-0.08	969334.66	6439595.90	2677.77
GCP9	967699.3	6439158	2550.9899	0.5	0.94	-0.90	0.23	-0.15	967698.40	6439158.23	2550.84
GCP10	967056.4	6438897	2231.2299	0.5	1.11	0.72	-0.84	-0.12	967057.12	6438896.16	2231.11
				Median ±1σ [m]	0.57 ±0.34						

Table A2: Results of the manual control points assessment between the orthomosaics of 1960 and 2018. Locations of the points are shown in Figures 3 and A1. Coordinates are mentioned in the EPSG:2154 - RGF93 v1 / Lambert-93 system.

ID	Ref. year	1960		2018		Y diff [m]	X diff [m]	Distance [m]
		Y Coord.	X Coord.	Y Coord.	X Coord.			
1	1960	6439755.99	967286.309	6439756.8	967287.176	-0.81	-0.87	1.19
2	2018	6439617.448	967304.239	6439617.101	967303.589	0.35	0.65	0.74
3	2018	6439724.814	967578.359	6439725.682	967579.053	-0.87	-0.69	1.11
4	1960	6439577.379	967444.676	6439577.9	967445.254	-0.52	-0.58	0.78
5	1960	6439482.492	967386.922	6439483.403	967387.356	-0.91	-0.43	1.01
6	2018	6439348.534	967357.207	6439350.009	967356.686	-1.47	0.52	1.56
7	2018	6439237.047	967410.044	6439238.869	967410.477	-1.82	-0.43	1.87
8	2018	6439087.211	967537.061	6439087.992	967537.755	-0.78	-0.69	1.04
9	2018	6439897.034	967721.948	6439895.646	967722.728	1.39	-0.78	1.59
10	2018	6439925.404	968064.174	6439924.667	968064.218	0.74	-0.04	0.74
11	1960	6439786.761	968010.643	6439786.862	968010.845	-0.10	-0.20	0.23
							Median ±1σ [m]	1.04 ±0.45

Table A3: Statistics of the rock glacier, units, and control areas from the IMCORR analysis. Total area of both orthomosaics is 3067391 m^2.

	n	% of the total orthomosaic area	Area [m^2]	Surface displacement between 1960-2018 [m]			
				Median ±1σ	Mean	Minimum	Maximum
Rock glacier	4181	15.54	476648	1.30 ±2.01	2.37	0.02	20.41
Unit I	1500	4.95	151798	1.19 ±0.40	1.22	0.07	5.38
Unit II	1155	4.09	125560	0.95 ±0.60	1.08	0.02	13.28
Unit III	971	3.57	109624	1.96 ±1.45	2.19	0.12	13.28
Unit IV	321	1.25	38363	8.49 ±2.93	8.59	2.86	17.28
Unit V	234	1.68	51595	8.30 ±4.90	8.39	0.29	20.41
Control 1	65	0.22	6654	1.17 ±0.32	1.09	0.07	1.54
Control 2	170	0.56	17132	0.67 ±0.36	0.75	0.20	1.77
Control 3	96	0.32	9964	0.31 ±0.23	0.36	0.02	1.56
Control 4	37	0.14	4228	0.88 ±0.25	0.89	0.23	1.51
Control 5	55	0.18	5547	1.01 ±0.34	0.98	0.11	1.78
Control 6	65	0.21	6536	1.28 ±0.33	1.26	0.59	1.83
Control all	488	1.63	50061	0.79 ±0.43	0.82	0.02	1.83

Formatted: Line spacing: single